Diploma Thesis

Design and Testing of a Membrane-Based Electrochemical Hydrogen Compressor

submitted in satisfaction of the requirements for the degree of
Diplom-Ingenieur
of the TU Wien, Faculty of Mechanical and Industrial Engineering

---

Diplomarbeit

Aufbau und Test eines membranbasierten elektrochemischen Wasserstoffkompressors

ausgeführt zum Zwecke der Erlangung des akademischen Grades eines
Diplom-Ingenieurs
eingereicht an der Technischen Universität Wien, Fakultät für Maschinenwesen und Betriebswissenschaften

von

Florian Fritsch, BSc

Matr.Nr.: 01525109

unter der Anleitung von

Ao.Univ.Prof. Dipl.-Ing. Dr.techn. **Michael Harasek**

Univ.Ass. Dipl.-Ing. Dr.techn. **Christian Jordan**

Institut für Verfahrenstechnik, Umwelttechnik und technische Biowissenschaften
Forschungsbereich Thermische Verfahrenstechnik und Simulation
Technische Universität Wien
Getreidemarkt 9, 1060 Wien, Österreich

Okinawa, im Oktober 2022

Affidavit

I declare in lieu of oath, that I wrote this thesis and performed the associated research myself, using only literature cited in this volume. If text passages from sources are used literally, they are marked as such. I confirm that this work is original and has not been submitted elsewhere for any examination, nor is it currently under consideration for a thesis elsewhere. I acknowledge that the submitted work will be checked electronically-technically using suitable and state-of-the-art means (plagiarism detection software). On the one hand, this ensures that the submitted work was prepared according to the high-quality standards within the applicable rules to ensure good scientific practice „Code of Conduct“ at the TU Wien. On the other hand, a comparison with other student theses avoids violations of my personal copyright.

October 2022 in Okinawa, Japan

List of Abbreviations

ADC analogue to digital converter

AEM anion exchange membrane

CCM catalyst coated membrane

DRI direct reduced iron steel production

EHC electrochemical hydrogen compressor (Elektrochemischer Wasserstoffkompressor)

emf electromotive force

GDL gas diffusion layer

HER hydrogen evolution reaction

LHV lower heating value

MEA membrane electrode assembly

MFC mass flow controller

OCV open circuit voltage

OER oxygen evolution reaction

PCB printed circuit board

PEM polymer electrolyte membrane

RTD resistance temperature detector

SMC surface mount component

stp standard temperature and pressure (0 °C and 101 325 Pa)

List of Symbols and Constants

α	Symmetry factor or stoichiometric coefficient ([-] or [-])
$\alpha_{i,j}$	Separation factor for the species i and j ([-])
β	Enrichment factor or stoichiometric coefficient ([-] or [-])
$\Delta\varphi$	Galvani potential difference ([V])
Δp	Pressure difference ([Pa] or [bar])
Δp_i	Partial pressure difference for the species i ([Pa])
η	Overpotential ([V])
κ	Isentropic coefficient ([-])
μ	Chemical potential or general efficiency ([J/mol] or [-])
μ_i	Current efficiency of an EHC ([-])
μ_v	Voltage efficiency of an EHC ([-])
μ_c	Efficiency of the Carnot cycle ([-])
μ_{ehc}	Efficiency of an EHC ([-])
μ_{th-fc}	Maximum theoretical fuel cell efficiency ([-])
ρ	Film thickness ([m])
σ	Ionic conductivity ([S/m $= 1/(\Omega\,\mathrm{m})$])
$\tilde{\mu}_i$	Electrochemical potential of the species i ([J/mol])
a_i	Activity coefficient of species i ([-])
C_B	Concentration in the bulk ([mol/m^3])
C_S	Concentration at the surface ([mol/m^3])
d	Membrane thickness ([m])
D_i	Diffusion coefficient for the species i ([m^2/s])
F	Faraday constant ([96485, 33C/mol])
I	Current ([A = C/s])
i	Current density ([A/cm^2])
i_0	Exchange current density ([A/cm^2])
i_{ext}	Current density calculated from externally measured current ([A/cm^2])
i_{tot}	Current density calculated from flux and the Faraday equation ([A/cm^2])
j	Transmembrane flux ([mol/(m^2 s)])
j_i	Partial flux of species i ([mol/(m^2 s)])
N	Amount in mole i ([mol])
P_i	Permeability for the species i in a certain matrix ([mol m/(m^2 s Pa)])
Q	Charge ([C])
q_{12}	Specific heat flux ([J/mol])
r	Specific cell resistance ([Ω cm^2])
R	Ideal gas constant ([8,314 J/(mol K)])
R_i	Retention coefficient for the species i ([-])
U	Voltage actually applied to the Stack ([V])
U_e	External electrolysis voltage ([V])

U_{th}	Theoretical cell voltage ([V])
U_{th}^{0}	Theoretical cell voltage at 25 °C, 1 bar, 1 mol/L ([V])
w_i	Mass fraction of species i ([-])
w_{t12}	Technical work ([J/mol] or [J/kg] or [J/m^3] or [kW h/m^3])
x_i	Mole fraction or dimensionless concentration of species i ([-])
z	Number of charges ([-])
%	All non further specified concentration values ([%(v/v)])

Kurzfassung

Wasserstoff (H_2), das leichteste aller Gase, sorgt oft für schwere Diskussionen und gespaltene Meinungen. Während uns die Auswirkungen des Klimawandels von Jahr zu Jahr drastischer vor Augen geführt werden, existiert immer noch kein klarer, weltweit einheitlicher und konsistent durchgeführter Plan, um unsere starke Abhängigkeit von fossilen Energieträgern in absehbarer Zukunft auf Null zu reduzieren. Ohne einen drastischen Ausbau der Produktionskapazitäten erneuerbarer Energien wird dieses Ziel nicht erreichbar sein. Mit diesem Ausbau kommen etliche technische, aber auch nicht technische Hürden einher. Die zeitlich teilweise stark schwankenden Produktionsraten einiger erneuerbarer Energieproduktionsmethoden ist eine dieser Hürden. Der öffentliche Diskurs ist, teilweise zurecht und teilweise aufgrund von unrealistischen Vorstellungen, sehr stark auf Elektrifizierung fokussiert. Direkte Nutzung elektrischer Energie ist, wo möglich und sinnvoll, aufgrund der unvermeidbaren Umwandlungsverluste natürlich zu präferieren. Es gibt allerdings eine Reihe treibhausgasintensiver Prozesse, welche sich auf absehbare Zeit nicht direkt elektrisch betreiben lassen werden können. Auch diese Prozesse müssen, um die zum Beispiel bei der Pariser Klimakonferenz 2015 gesetzten Klimaziele zu erreichen, „endkarbonisiert“ werden. Bevor bei Überproduktion erneuerbarer Energie diese gar nicht genutzt wird, ist es sinnvoll, diese elektrische Energie in chemische Energie umzuwandeln. Möglich ist dies zum Beispiel durch Wasserstoffproduktion mittels Elektrolyse. Der so produzierte H_2 wird allerdings nicht zwangsweise an dem Ort produziert, an welchem es auch benötigt wird. Eine Möglichkeit, H_2 ohne große Investitionen in neue Infrastruktur zu transportieren, ist das bestehende Erdgasnetz. H_2 wird hierbei gemeinsam mit dem bereits transportierten Erdgas im Erdgasnetz verteilt. Somit kann das bestehende Erdgasnetz einen sehr großen Speicher für erneuerbare Energie bereitstellen. Für Verbraucher, welche hochreinen H_2 benötigen, bleibt allerdings die Herausforderung bestehen, diesen ohne großen Aufwand wieder aus dem Erdgas abzutrennen. Eine mögliche Lösung dafür ist der elektrochemischer Wasserstoffkompressor (EHC). Elektrochemische Wasserstoffkompression ist ein elektrochemisches Verfahren, bei dem eine ionenleitende Membran verwendet wird, um H_2 durch Zerlegung in Protonen und Anlegen einer externen Spannung hochselektiv von einer Seite der Membran auf die andere zu transportieren. Dieses Verfahren funktioniert auch gegen einen Konzentrations- oder Druckgradienten. Es ist daher mittels EHC möglich, H_2 in einem Schritt aus einem Quellstrom mit geringer Wasserstoffkonzentration abzutrennen und ihn mit höherem Druck und höherer Reinheit wieder abzugeben. Aufgabe für diese Diplomarbeit war es, eine Versuchsanlage im Labormaßstab zu bauen, welche Tests jenes Verfahrens mit unterschiedlichen Betriebsparametern erlaubt. Es wurde eine Versuchsanlage entworfen, welche ein thermostatisiertes Bad, eine Gasbefeuchtungseinheit, eine Gastrocknungseinheit, Stromversorung und Messtechnik enthält, um verschiedene Betriebsbedingungen eines EHC experimentell untersuchen zu können. Zum Abschluss der Arbeit wurden alle Komponenten der Versuchsanlage durch eine Reihe von Experimenten auf Funktion überprüft. H_2 konnte mittels der Versuchsanlage erfolgreich in einem Schritt aus einem Gasgemisch (4 % H_2) entfernt, auf 5 bar Überdruck komprimiert und auf nahezu 100 % Reinheit angereichert werden. Die Machbarkeit elektrochemischer Wasserstoffkompression konnte somit erfolgreich demonstriert werden. Mit weitere Forschung könnte sich diese als wichtige Technologie beim Übergang in eine Zukunft erneuerbarer Energien erweisen. Die ersten Experimente zeigten jedoch auch, dass es noch viel Raum für Verbesserungen gibt und dass weitere Experimente notwendig sind, um diesen Laboraufbau vollständig zu charakterisieren.

Abstract

Hydrogen, the lightest of all gases, often inspires heavy debates and a slew of dissenting opinions. Whether or not it will be widely used as a low carbon energy storage material in the future can only be speculated about at the present time. As the impacts of climate change become increasingly evident every year, there is still no clear, globally unified, and consistently implemented plan to reduce our heavy reliance on fossil fuels in the foreseeable future. Without a drastic expansion of the production capacities of renewable energies, this goal will not be achievable. This expansion comes with a number of technical, but also non-technical hurdles. The strongly-fluctuating production rates of some renewable energy production methods is one of these hurdles. The public discourse is very much focused on electrification which is partly well-grounded, but, on the other hand, driven by unrealistic expectations. Direct use of electrical energy is, where possible and sensible, to be preferred due to the unavoidable conversion losses. However, there are a number of greenhouse gas-intensive processes that, in the foreseeable future, cannot be operated using electric energy. In order to achieve the climate targets set at the Paris Accords in 2015, for example, these processes must also be "decarbonised". Before the energy produced during times of overproduction of renewable energy is not used at all, it makes sense to convert it into chemical energy. This is possible, for example, by using electrolysis to produce hydrogen. However, the hydrogen produced in this way is not necessarily produced at the location where it is needed. One way of transporting this hydrogen without major investments is the existing natural gas network. Hydrogen is distributed in the natural gas network together with natural gas. The existing natural gas network can thus provide a very large storage facility for renewable energy. However, consumers who need high-purity hydrogen still face the challenge of re-separating this hydrogen, without major effort, from the natural gas mixture. A potential solution is the electrochemical hydrogen compressor. Electrochemical hydrogen compression is an electrochemical process in which an ion-conducting membrane is used to transport hydrogen highly selectively from one side of the membrane to the other, by decomposition into protons and application of an external voltage. This method also works against a concentration or pressure gradient. It is therefore possible, using electrochemical hydrogen compression, to separate hydrogen from a source stream with a low hydrogen concentration in one step, and release it again at higher pressure and higher purity. The task for this diploma thesis was to design, build and test a laboratory scale electrochemical hydrogen compression unit which allows tests of the process with different operating parameters. A unit was designed containing a thermostated bath, a gas humidification unit, a gas drying unit, power supplies and measurement equipment in order to experimentally investigate different operating conditions of an electrochemical hydrogen compressor. At the end of the work, all components of the unit were checked for function in a series of experiments. During these one-step experiments, hydrogen was successfully removed from a gas mixture containing only 4 % hydrogen and compressed to 5 bar over-pressure, reaching a purity in the final product of almost 100 %. These experiments successfully demonstrated the feasibility of electrochemical hydrogen compression. With more research, it might prove to be an important puzzle piece in the transition towards a future of exclusively using renewable energy. The first experiments, however, also revealed that there is plenty of room for improvement, and that more experiments have to be carried out to fully characterise this laboratory setup.

Contents

Chapter 1

Introduction

1.1 Motivation

While political leaders are discussing the necessary legal frameworks for the future use of renewable energy, scientists and engineers are working on the technological side to make sure these renewable forms of energy will be able to deliver the required energy exactly when needed. Both the ever-growing public pressure to act on climate change and geopolitical considerations to become less reliant on energy imports are major driving factors for this shift towards renewable forms of energy. As we are aware, the intermittent nature of most forms of renewable energy production (e.g. wind and solar) is one of the biggest hurdles to overcome before they can replace fossil fuels on a larger scale. The technological progress in this field of research is rapid. One of the numerous possible solutions to this energy storage dilemma is the production of H_2 via electrolysis. If used correctly, hydrogen can be an outstanding energy carrier and storage material. When produced via electrolysis, H_2 emits no direct carbon during production. Hydrogen production is a mature science and many commercial "of-the-shelf" electrolysers can easily be obtained. Hydrogen storage and transportation, however, remain a technological challenge, in part due to hydrogen's low volumetric energy density. Even though many possible solutions like high-pressure storage in composite material pressure vessels, cryogenic liquefaction, physical adsorption on highly porous materials, or storage in chemically bound forms like Ammonia are all possible, all of them come with their benefits and drawbacks [1, 2].

The method proposed in this work employs a unique approach for H_2 distribution and utilisation at the location where it is needed: The existing natural gas infrastructure in combination with an electrochemical hydrogen compressor (Elektrochemischer Wasserstoffkompressor, EHC) capable of purifying H_2 from low concentrations of only a few percent to the high purity required for the use in H_2 fuel cells and other applications. This means that existing pipelines don't need to be repurposed completely to transport only hydrogen. They can still be used to transport natural gas but, at the same time, can act as a versatile hydrogen delivery and storage system. This is based on the fact that the driving force to selectively transport H_2 through the EHC as protons is not a difference in pressure but a difference in electrical potential, and both purification and compression can be achieved in a single apparatus.

1.2 Aim of this Work

The task for this Master's thesis was to engineer a functional prototype of an EHC with a maximum working pressure of 10 bar above atmospheric pressure. Preliminary theoretical work had been performed in a previous Bachelor's thesis [3] and the process to be replicated with this proof of concept laboratory scale apparatus was detailed in the respective patent [4]. The literature cited in this Bachelor's thesis and the process described in this patent lead to many design requirements, like the necessity of temperature control for the compressor or gas humidification and dehumidification as discussed in more detail later in section 3.1.

1.3 Hydrogen and Methane

1.3.1 Hydrogen

Hydrogen (Chemical Symbol H) is the lightest element in the periodic table. It consists of a single proton and an electron. In this work, the phrase hydrogen will be used for molecular hydrogen (H_2). Molecular hydrogen is a very light and non-toxic gas at standard temperature and pressure (stp). Due to its low density and high diffusion coefficient, H_2 is rapidly diluted in air [5]. Some material properties of hydrogen and other typical combustible fuels are given in Tab. 1.1. When comparing these properties it becomes apparent that hydrogen has a high gravimetric energy density but a very low volumetric energy density at stp. This, in part, is the reason for many of the technological challenges that come with using hydrogen as an energy carrier or energy storage material. Many consider the lack of dedicated hydrogen infrastructure the biggest obstacle to widespread hydrogen adoption as an energy carrier. At the same time, there is no real incentive to build new and expensive hydrogen infrastructure without widespread adoption of fuel cells. This could be referred to as a "chicken-and-egg-problem" [6, p. 469]

Tab. 1.1: Properties of hydrogen and other typical combustible fuels

		Hydrogen	Diesel fuel	Petrol	Methane	Propane
Formula	-	H_2	C_xH_y	C_xH_y	CH_4	C_3H_8
Molar mass	g/mol	2,016[b]	-	-	16,04[b]	44,1[d]
Density	kg/Nm^3	0,0899[a]	-	-	0,72[b]	1,5503[d]
Lower heating value	kWh/Nm^3	3,00[a]	-	-	9,97[a]	28,89[a]
Lower heating value	kWh/kg	33,33[a]	11,9[a]	12,0[a]	13,9[a]	12,88[a]
Boiling point	°C	-252,77[a]	-	-	-161,48[b]	-42[d]
Flammability limit	% (v/v)	4,0-75,0[a]	0,6-7,5[e]	0,6–7,6[f]	4,4–17[b]	1,7–10,8[d]

Data from [a] Linde-Gas [5] [b] RÖMPP-Redaktion et al. [7] [c] Hartmann-Schreier [8] [d] RÖMPP-Redaktion [9] [e] Habermeyer and Geldsetzer [10] [f] Achten [11]

Hydrogen Uses - Past, Present and Future

Hydrogen's main use today is in Ammonia production (mainly for fertilisers) and petrochemical refineries. According to latest data from the IEA [12] in 2020, 42 % out of the 88,48 Mt[1] of global hydrogen demand were used in refining processes. The remaining 58 % were mainly used for chemical production (ammonia and methanol) or for producing steel using the "direct reduced iron steel production (DRI)" method. These numbers are slightly lower than the demand in previous years, possibly due to the coronavirus pandemic. Nevertheless global demand for H_2 has been growing for many years now, and the main uses have more or less remained unchanged (see historic data shown in Figure 1.1).

Hydrogen Production

The exact percentage values of hydrogen production vary from year to year and from source to source, since the assumptions vary that are the basis for the respective calculations performed. The essence is clear and similar throughout many sources though:

[1] This includes more than 70 Mt H_2 used as pure hydrogen and less than 20 Mt H_2 mixed with carbon-containing gases in methanol production and steel manufacturing. It excludes around 30 Mt H_2 present in residual gases from industrial processes used for heat and electricity generation: as this use is linked to the inherent presence of hydrogen in these residual streams – rather than to any hydrogen requirement – these gases are not considered here as a hydrogen demand.

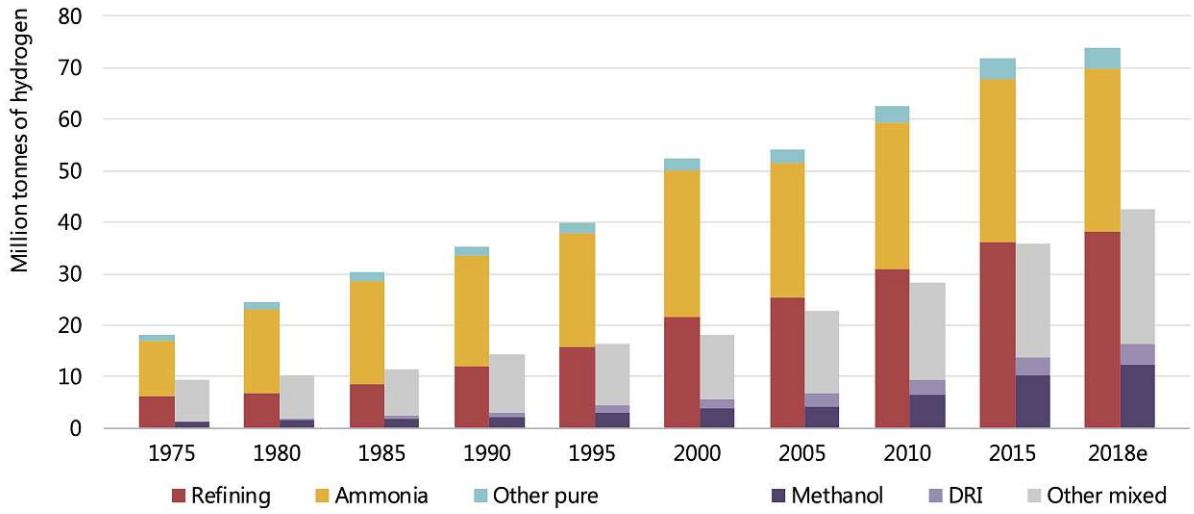

Fig. 1.1: Historic data for the global annual demand for hydrogen from 1975 until 2018. Taken from the IEA [13]. Bars on the left (green, yellow and red) are applications that require hydrogen with only small levels of additives or contaminants. Bars on the right (grey, violet and purple) represent demand for applications that use hydrogen as part of a mixture of gases, such as synthesis gas. The bar for the year 2018 was still an estimation when the report containing this Figure was published. Therefore the label "2018e"

Today, only about 0,02 %–0,1 % of all global H_2 is produced by dedicated water electrolysis [12, 13, 14]. Around 0,6 %–5 % of all H_2 is produced via electrolysis, if H_2 production as a side product of the chlorine and caustic soda production is included [12, 13, 15]. The remaining 95 %–99,4 % of the total hydrogen production is presently (2020) produced from fossil fuels (mostly natural gas and coal) [12, 13, 15, 16]. Even though the absolute demand for H_2 has increased (see Figure 1.1) these fractions have remained unchanged within the last 10 years [6, p. 474].

1.3.2 Methane

CH_4, the simplest possible alkane, is a colourless and odourless gas that consists of one carbon atom and four hydrogen atoms. It is the main constituent of natural gas and a very potent greenhouse gas when released into the atmosphere. Natural gas is a fossil fuel and we should therefore strive to reduce the use of this resource. Alternative sources for CH_4 (e.g. producing it from biomass) exist but are not very widespread. In some cases natural gas can be replaced by or mixed with other gaseous fuels, assuming properties like the dew point, the Wobbe index or the density stay within certain limits. Small amounts of H_2 are already commonly present in natural gas and different countries have different regulations regarding the limit of H_2 allowed in their natural gas grid. Austria allows up to 4 % (molar), Germany and Switzerland allow 5 % (by volume) and the Netherlands have a limit of 12 % (by volume) [17]. Kuczyński et al. [18] discusses the implications as well as the positive and negative consequences of transporting different fractions of H_2 together with CH_4 in pipelines. Some properties of CH_4 can be found in Table 1.1.

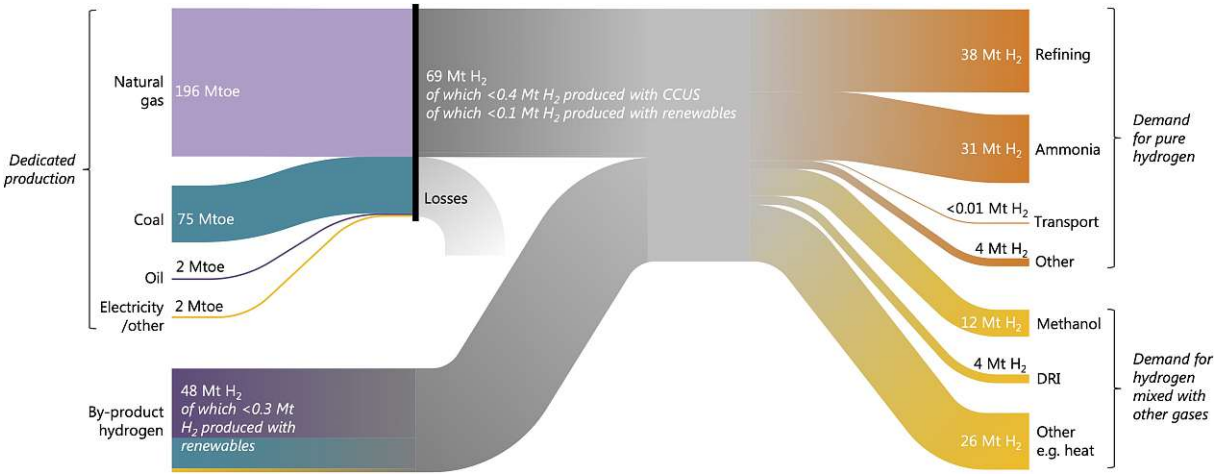

Fig. 1.2: Sankey diagram depicting the hydrogen value chain from the IEA [13]. The shares of hydrogen production based on renewables are calculated using the share of renewable electricity out of all global electricity generation for this year. The share of dedicated hydrogen produced with carbon capture, utilization and storage is estimated based on existing installations with permanent geological storage, assuming an 85% utilisation rate. Data shown is an estimate for 2018.

Chapter 2

Theory

2.1 Classification of the Field of Electrochemistry

Electrochemistry is a sub-discipline of physical chemistry that is characterised by the separation of the reactants in space. Consider a "normal" chemical reaction, like burning hydrogen gas (H_2) in air. The H_2 and the oxygen (O_2) molecules have to get close enough to each other to overcome the initial repulsion of their negatively charged electron clouds and eventually "shift their electrons around" on the molecular level to form new bonds and produce the product H_2O. Overcoming this repulsion in a "classical" reaction is possible by an increase in velocity (i.e. kinetic energy or temperature) of the molecules until a temperature above the ignition temperature is reached.

If the same reaction happens electrochemically, the two reactant molecules never actually meet in one place. Instead, two different partial reactions - one oxidation and one reduction reaction - proceed separated from each other in space. This necessarily leads to an electron and an ion flux on a larger than molecular scale between these two partial reactions. The end product of these separated oxidation and reduction reaction is again H_2O.

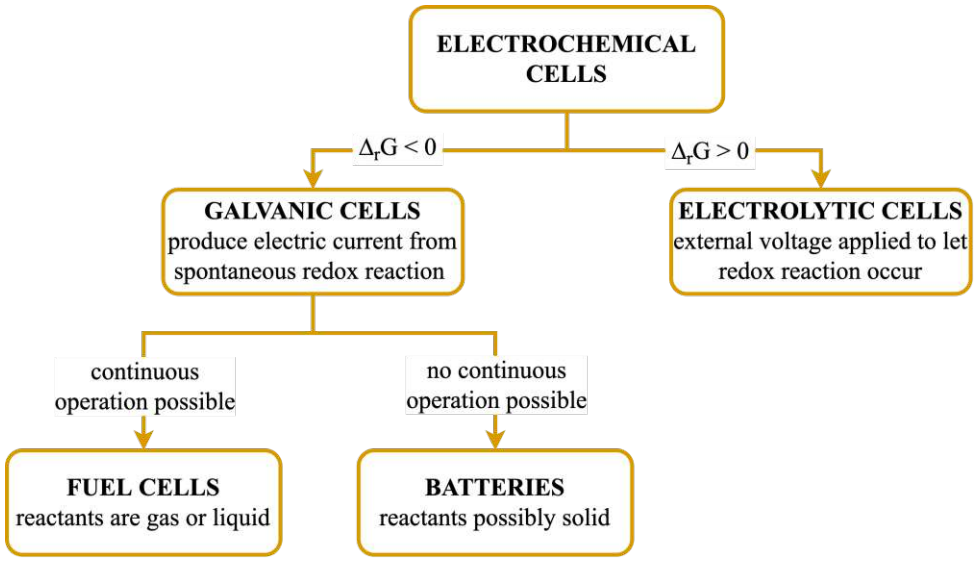

Fig. 2.1: Classification of the field of electrochemistry.

For any electrochemical reaction to occur, some sort of electrochemical cell is required. Electrochemical cells consist of two electrodes carrying charges (in the form of electrons or holes) and an electrolyte between the electrodes carrying ions (cations or anions). The construction and basic elements of an electrochemical cell will be further discussed in section 2.4. Electrochemical cells can be subdivided into categories as depicted in Figure 2.1. If the reaction in an electrochemical cell occurs spontaneously ($\Delta_r G < 0$) and produces an electric current when the two electrodes

are connected, the cell is called a GALVANIC CELL. If an external voltage has to be applied to let a non-spontaneous redox reaction occur ($\Delta_r G > 0$), it is called an ELECTROLYTIC CELL. Galvanic cells can be further subdivided into fuel cells that can be operated continuously, and batteries that can not be operated continuously. Batteries could be further divided into primary batteries that can only be discharged once, and secondary batteries that can be recharged and then discharged again. This division (and others) are omitted from Figure 2.1 because the present work will focus on fuel cells and electrolytic cells as a foundation for the EHC.

2.2 Electrochemical Energy Conversion

As described in section 2.1, electrolytic cells are used to let non-spontaneous redox reactions occur by applying a voltage to the cell through an external electrical power source. That means they convert electrical energy to chemical energy like shown at the top of Figure 2.2.

Fuel cells are used to continuously and directly convert chemical energy into electrical energy that can be used in an external circuit. In Figure 2.2, fuel cells are depicted by the bottom arrow. Electrochemistry is not the most common path currently taken to transform these two forms of energy (chemical to electrical) into each other. The most common path, by far, is combustion of chemical species for the production of heat, then turning that heat into mechanical energy using a turbine and then converting the mechanical energy into electrical energy using a generator. Each of these steps has potential energy losses attached to it. For example, converting chemical energy to thermal energy using combustion (left arrow in Figure 2.2), can only be 100 % efficient, if the fuel is entirely burned and no leftover fuel is allowed to escape with the combustion gases. Even though every energy transformation has an efficiency attached to it, none of the efficiencies in the depicted energy transformations are as limiting as the Carnot cycle efficiency for turning heat into mechanical energy and the theoretical fuel cell efficiency. These two are further discussed in equation (2.1)

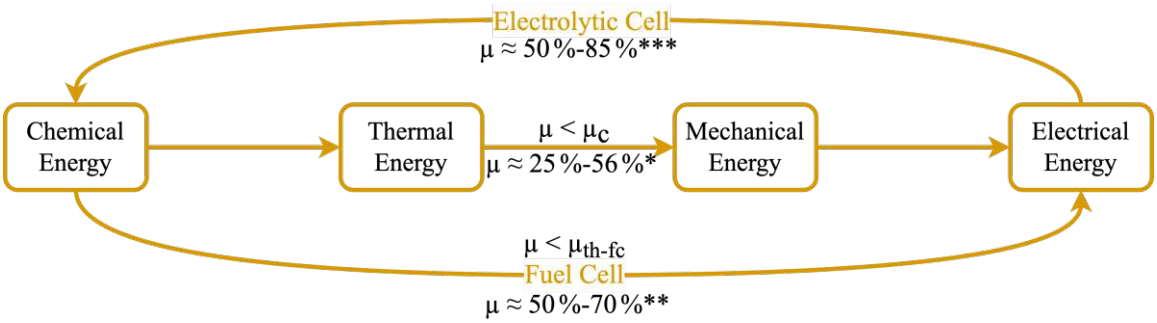

Fig. 2.2: The path taken for electrochemical energy conversion (outer circular path) against the path taken for classical electricity production by burning fuels (inner path). Here μ_c is the efficiency of the Carnot cycle and μ_{th-fc} is the maximum theoretical efficiency of a fuel cell [19, p. 159]. The percentages given in this Figure are typical values actually achieved in real world applications. (* from [20], ** from [21] and *** from [14])

$$\text{Fuel Cell: } \mu_{th-fc} = 1 - \frac{T_f \Delta_r S}{\Delta_r H} \qquad \text{Carnot Cycle: } \mu_c = 1 - \frac{T_c}{T_h} \tag{2.1}$$

Assuming *very* favourable conditions, both for the Carnot cycle efficiency and the maximum theoretical efficiency of a hydrogen fuel cell, some numerical values were chosen or taken from literature.

$$\mu_{th-fc} = 1 - \frac{283{,}15\,\mathrm{K}(-36\,\frac{\mathrm{J}}{\mathrm{mol\,K}})}{-241\ 650\,\frac{\mathrm{J}}{\mathrm{mol}}} \qquad \mu_c = 1 - \frac{298{,}15\,\mathrm{K}}{1873{,}15\,\mathrm{K}} \tag{2.2}$$

$$\mu_{th-fc} = 95{,}8\,\% \qquad \mu_c = 84{,}1\,\%$$

- $T_f = 10\,°\mathrm{C}$ was chosen as the fuel cell operating temperature
- $\Delta_r S = -36\,\mathrm{J/(mol\,K)}$ as the reaction entropy (assuming product H_2O is vapour) at T_f was calculated with data from the VDI [22] and the NIST [23]
- $\Delta_r H = -241{,}65\,\mathrm{kJ/mol}$ as the reaction enthalpy (assuming product H_2O is vapour) at T_f was calculated with data from VDI [22] and NIST [23]
- $T_c = 25\,°\mathrm{C}$ was chosen as the cold side temperature for the Carnot cycle
- $T_h = 1600\,°\mathrm{C}$ as the hot side temperature of a gas turbine was taken from Mitsubishi Heavy Industries, Ltd [24] (visited April 15, 2022)

The somewhat constructed results display why fuel cells/electrochemical energy conversion can be an attractive alternative to classical methods. Obviously there is a number of caveats to consider with the results of equations (2.2).

First, some considerations about the Carnot cycle efficiency: As depicted in Figure 2.2, the Carnot cycle efficiency is not the only efficiency on the path for classical electricity production. Generators and combustion also have an efficiency attached to them, albeit very high. The temperature of 1600 °C, chosen for the hot side of the Carnot cycle efficiency, is close to the limit of what many materials can endure. Electrical efficiencies ($E_{electric}/E_{fuel}$) that are actually achieved with classical power generation are always lower than μ_c from equation (2.2) (see typical percentages in Figure 2.2). The Siemens AG proclaimed a world record in 2016 [25] (visited April 15, 2022) when a combined cycle gas turbine power plant with one of their generators reached 61,5 % electrical efficiency. On the positive side, waste heat that is generated during classical combustion is generated at a very high temperature. Therefore, a part of this waste heat can still easily be utilised for applications like process steam production or district heating. Like this, reaching efficiencies in the 80 %–90 % range [26] is common. The waste heat produced by a polymer electrolyte membrane (PEM) fuel cell that is operated at under 100 °C does not have as many obvious applications, though it can still be utilised to some degree.

Next, the calculated maximum theoretical efficiency for the hydrogen fuel cell should also be scrutinised. The very low operating temperature of 10 °C, chosen for the calculation of μ_{th-fc} is beneficial for a high fuel cell efficiency and a high theoretical cell potential. Low temperatures, however, are not practical for actual applications of fuel cells. As pointed out by Barbir [6, p.24]: "[...] in general a higher cell temperature results in a higher cell potential. This is because the voltage losses in operating fuel cells decrease with temperature, and this more than compensates for the loss of theoretical cell potential." Another factor leading to this very high maximum efficiency was the assumption that the product water is steam and not liquid water. In other words, the use of the lower heating value (LHV) for $\Delta_r H$, that doesn't include the enthalpy of vaporisation. It is, however, common practice to use the LHV for calculating fuel cell efficiencies. Not only because it leads to higher numbers, but also because it is often used for calculating the efficiency of classical combustion devices and therefore gives a better comparison between the two. As long as it is somehow specified which value was used for $\Delta_r H$, both the lower and higher heating value can be used.

2.3 Membrane Separation Processes

A membrane is a very common concept in various different fields of science and engineering. In its most general form, a membrane is a a quasi two dimensional mechanical structure serving as a barrier that separates two compartments and selectively impedes or controls the transport between these two phases. There are many different membrane processes that are based on different separation principles or mechanisms. The composition of the species to be separated by a membrane, can range from small particles to individual molecules [27, 28, 29].

One very important branch of membrane science covers biological membranes, like the ones that protect the nucleus in eukaryotes and make up the biggest part of a cell's outer hull. These membranes control which molecules enter and leave a cell and maintain a certain osmotic pressure from inside the cell to its surroundings, therefore keeping the cell alive. There would be no life without membranes. This however, no matter how interesting, will not be the topic of this work. When membranes are mentioned in this work, synthetic membranes, technical membranes or industrial membranes for separation are meant. They essentially perform the same job as biological membranes - restrict the motion of certain species through a barrier - but are made of polymers, inorganic materials or metallic materials [29].

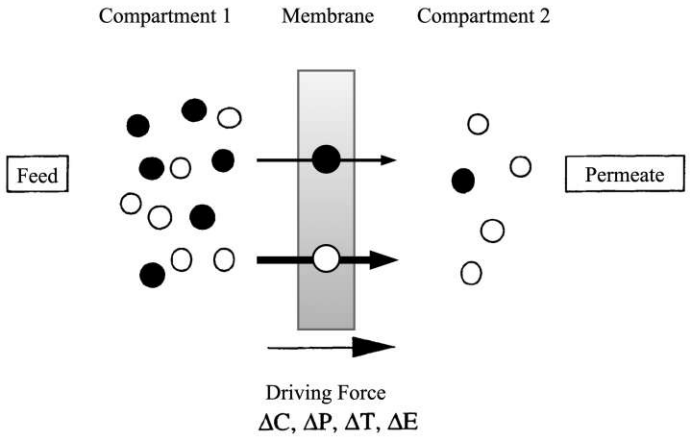

Fig. 2.3: Schematic representation of a membrane separation process. The feed, a mixture of two different particles shown as black and white, approaches the membrane and through some sort of externally applied driving force, the white particles are preferentially transported through the membrane to make up most of the permeate on the other side. Figure adapted from [28]

Other ways to classify membranes also exist and are shown in Figure 2.4a. Schematic drawings of a few basic membrane types that will briefly be explained in this section are shown in Figure 2.4b.

Microporous membranes

Microporous membranes are very similar to conventional filters, the differentiating factor being hole sizes that are far smaller. Typical pore sizes for ultrafiltration and microfiltration using microporous membranes range from about 10 nm to about 10 µm [27]. Microporous membranes can be made from organic and inorganic materials and work by not letting any particles larger than the largest hole size of the membrane pass through to the permeate side (sieve effect).

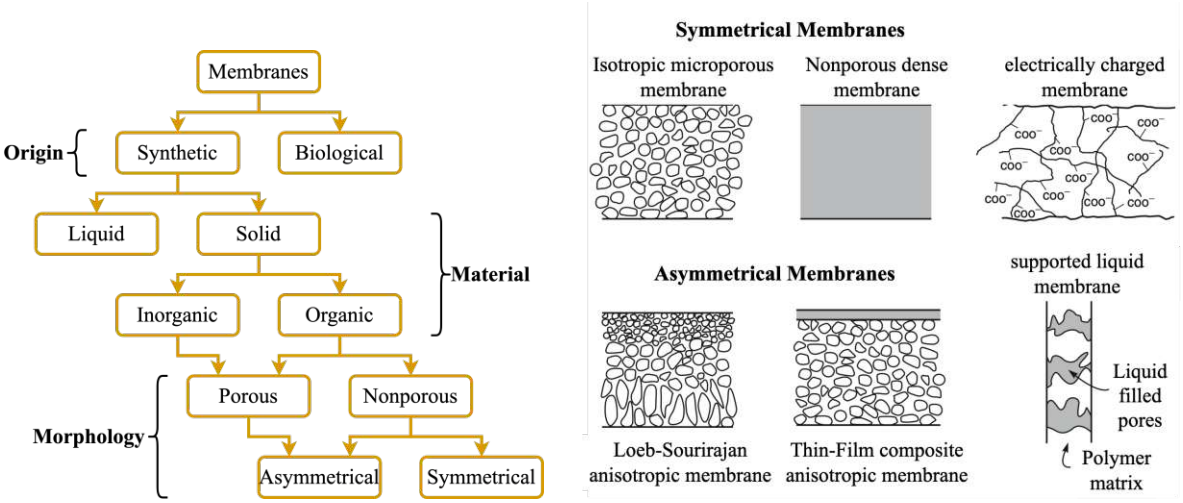

(a) Common ways to classify membranes include classification by material, origin and morphology. Figure adapted from [30]

(b) Schematic representations of different membrane types. Electrically charged membranes are commonly used for PEM fuel cells, electrolysis and electrochemical hydrogen compression (EHC). Figure adapted from [27]

Fig. 2.4: Possible ways to classify membranes and schematic drawings depicting some of these membrane types

Nonporous Dense Membranes

Nonporous dense membranes work by solution and diffusion. The preferentially transported species gets dissolved in the membrane material and, depending on the transport rate of this species in this membrane, moves through the material. The driving force for this movement can be a gradient in pressure, concentration or electrochemical potential. The transport rate of different species in the same membrane can be different therefore leading to separation [27]. These membranes can be used for reverse osmosis, nanofiltration, gas permeation or pervaporation processes [30].

Electrically Charged Membranes

"Electrically charged membranes can be dense or microporous, but are most commonly very finely microporous, with the pore walls carrying fixed positively or negatively charged ions." [27, p.5]. This membrane type can, depending on the charge of the ions on the pore walls, either be a cation exchange membrane or an anion exchange membrane. The main separation mechanism is the exclusion of ions of the same charge. This type of membrane is, for example, used for electrodialysis (both anion and cation exchange membranes), PEM fuel cells (see section 2.5.2), anion exchange membrane (AEM) electrolysis (see section 2.5.1) and EHCs. Probably the most widespread membrane used for PEM fuel cells, electrolysis and EHC is Nafion^{TM}. First introduced in 1967 by DuPont (Delaware, United States), it is a polymer based on polytetrafluoroethylene (Teflon^{TM}) [31, p. 69] with additional sulfonic acid groups. This combination gives Nafion^{TM} its specific properties. The structure based on Teflon ^{TM} is responsible for excellent chemical and thermal stability while the sulfonic acid groups give Nafion^{TM} the capability to selectively transport cations (mostly protons). Even though the polymer itself is thermally and chemically stable, operating temperatures for PEM are mostly limited to a maximum of 100 °C because liquid water is required to uphold Nafion^{TM}'s proton conducting properties.

2.3.1 Describing Membrane Processes - Selectivity, Flux and Permeability

To allow comparative studies on membrane processes or make decisions as to whether or not certain membrane processes are suitable for a certain separation task, we need some ways of describing the processes. Three important parameters for this discussion are selectivity, flux and permeability. [28]

Selectivity

The selectivity of a membrane is a way to describe how good a certain membrane is, under specific operating conditions, in separating one component out of a mixture of multiple components. Possible ways to quantify selectivity are:

$$\text{Enrichment factor:} \qquad \beta_i = \frac{w_{i,P}}{w_{i,F}} \text{ or } \frac{x_{i,P}}{x_{i,F}} \tag{2.3}$$

It describes how much higher the mass fraction w of the component i is in the permeate compared to the feed. For gas separation processes, the molar fraction x is sometimes used instead of w.

$$\text{Separation factor:} \qquad \alpha_{i,j} = \frac{w_{i,P} w_{j,F}}{w_{j,P} w_{i,F}} \text{ or } \frac{x_{i,P} x_{j,F}}{x_{j,P} x_{i,F}} \tag{2.4}$$

It describes how good a certain membrane is at separating a mixture of two components i and j. Very high and very low separation factors ($1 >> \alpha_{i,j}$ or $1 << \alpha_{i,j}$) show that the membrane is well suited for the separation task at hand while a separation factor of 1 means the membrane can not be used to separate the two components i and j at the current operating conditions.

$$\text{Retention coefficient:} \qquad R_i = 1 - \beta_i \tag{2.5}$$

As a close relative to the enrichment factor, the retention coefficient is used to describe which percentage of a component i is retained in the feed.

Flux

The flux is a flow rate that is not only normalised to time but also to membrane area. The flux can can either be given for all the components passing through a membrane together (transmembrane flux) or for every component individually (partial flux). In the literature [30, 27] the flux is often defined as a mass flux with SI units of $\mathrm{kg/(m^2\,s)}$ or $\mathrm{g/(m^2\,s)}$. In this work however, the flux j will be used as a molar flux with SI units of $\mathrm{mol/(m^2\,s)}$ because this is more convenient in combination with the many electrochemical processes that occur in an EHC. Mulder [28] mentions that all three versions of flux (volumetric, molar or mass) are common.

$$\text{Transmembrane flux:} \qquad j = \frac{1}{A_M}\frac{dn_P}{dt} \tag{2.6}$$

$$\text{Partial flux:} \qquad j_i = \frac{1}{A_M}\frac{dn_{i,P}}{dt} \tag{2.7}$$

$$\text{Partial flux:} \qquad j_i = L_i \frac{\Delta\mu}{d} \tag{2.8}$$

The partial flux j_i of a component i from equation (2.7) can generally be calculated as the product of the gradient of some driving force $\Delta\mu$ and a membrane dependant transport coefficient L_i for the component i. The driving force is divided by the membrane thickness d since the transmembrane flux is inversely proportional to membrane thickness. The resulting general equation is equation (2.8).

Permeability

Different models can be used to describe the mass transport in a membrane separation process. Two very common and successful models are the pore flow model, used for porous membranes, and the solution diffusion model. In the latter, the permeants dissolve in the membrane material and then diffuse through the membrane along a concentration gradient as previously explained on page 18 about nonporous membranes. Starting with the general form of the flux equation (2.8) and performing a few simple integration and substitution steps (see [30]) the equation describing the solution diffusion model can be attained. Different versions of the solution diffusion equation can be used for different driving forces $\Delta\mu$. Equation (2.10) shows the difference of partial pressure is shown, which is used in the modelling of gas permeation processes. The solution diffusion model however can also be used for other processes like reverse osmosis or pervaporation.

$$j_i = \frac{D_i S_i}{d} \Delta p_i \tag{2.9}$$

$$j_i = \frac{P_i}{d} \Delta p_i \tag{2.10}$$

In equation (2.10), D_i is the diffusion coefficient of component i in the membrane material, S_i is the sorption coefficient and the product of the two is the permeability P_i of component i in $\mathrm{mol\,m/(m^2\,s\,Pa)}$. The permeability P_i should not be confused with the permeance of a membrane. The permeance is the permeability divided by membrane thickness (P_i/d) [27, p. 37].

2.4 Electrochemical and Thermodynamic Theory

As previously mentioned in section 2.1, electrochemical cells are always made up of two electrodes, normally able to carry electrons, and an electrolyte between the two electrodes that can transport ions. The electrolyte can have different forms. It can be a liquid (organic liquid, water or molten salt) or a solid (ceramic or polymer). Figure 2.5 shows two typical electrochemical cells (both galvanic cells in this case) with different types of electrolytes and different types of electrodes. For further describing electrochemical cells, some electrochemical concepts need to be established.

2.4.1 Faraday's Law

Faraday's law is the equation that correlates the total charge Q (in C = coulomb) or current I (charge per time A = C/s) passed through a cell with the amount of product N (in mol) of an electrochemical reaction [32].

$$N = \frac{Q}{zF} \qquad \frac{dN}{dt} = \frac{1}{zF}\frac{dQ}{dt} \qquad \dot{N} = \frac{I}{zF} \tag{2.11}$$

Equation (2.11) shows three different versions of Faraday's law. Here, z is the number of electrons transferred per molecule of product and F is Faraday's constant (96 485,33 C/mol). Taking the reaction of Figure 2.5a as an example: If this galvanic cell produced a current of

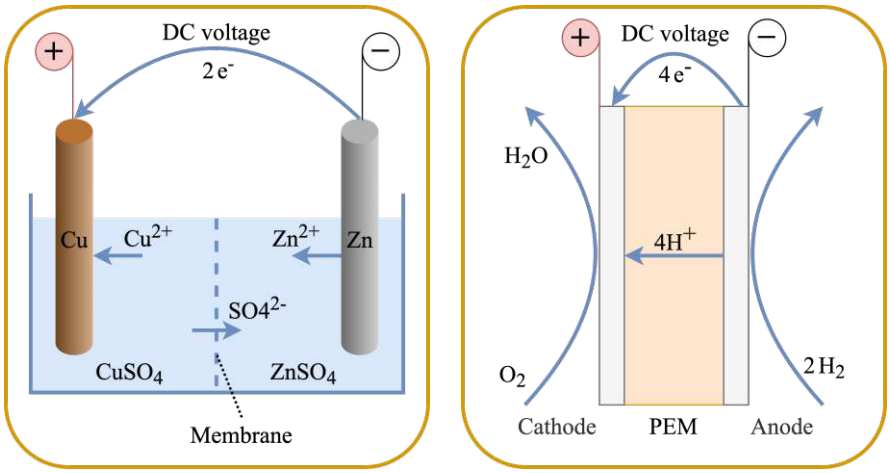

(a) Schematic representation of the Daniell cell, named after the inventor J. F. Daniell (1790–1845) who developed this battery type in 1836 [19]. Here, the electrolyte is an aqueous sulphate solution and the electrodes are Cu and Zn rods.

(b) Schematic representation of a PEM fuel cell. Here, the electrolyte is a proton conducting polymer and the electrodes are thin catalyst layers pressed to the membrane with electrically conductive substrates like carbon cloth.

Fig. 2.5: Schematic representations of a Daniell cell and a PEM fuel cell as examples for electrochemical cells.

1,8 A for 3 h, then after this time 0,1 mol of Copper were turned from Cu^{2+} to metallic Cu and collected on the Cu rod.

2.4.2 From Chemical Potential to Electrochemical Potential

In chemistry, chemical potential, denoted with the Greek letter μ (mu), is an important intensive property to describe the equilibrium of thermodynamic systems with phase changes or chemical reactions [33].

$$\mu_i = \left(\frac{\partial G}{\partial n_i}\right)_{T,p,n_j \neq n_i} \qquad \mu_i = \mu_i^0 + RT\ln(a_i) \tag{2.12}$$

As seen in the left equation of (2.12), the chemical potential is defined as the partial derivative of the Gibbs free energy with respect to one species n_i. Each species tends to minimise its μ_i. The right equation in (2.12) shows that the chemical potential can be split up into two parts. Here, the μ_i^0 term describes the "chemical surroundings" and the $RT\ln(a)$ term describes the activity (or concentration) dependence. For example, if one half of a glass was filled with a concentrated salt solution and the other half would be filled only with a mild salt solution, the $RT\ln(a)$ term for the concentrated solution would be higher than for the mild one due to the higher concentration. To minimise μ_i, some salt will move from the more concentrated to the less concentrated side. An example for the influence of the "chemical surroundings" term μ_i^0 would be, when water vapour from the air is drawn to a hydrophilic substance like $CuSO_4$ even though its concentration in the $CuSO_4$ will be higher than in the Air.

$$\boxed{\tilde{\mu}_i = \mu_i^0 + RT\ln(x_i) + zF\varphi} \tag{2.13}$$

In electrochemistry, the chemical potential is extended with another term ($zF\varphi$) to also include the effects of electrical fields on ions. The electrochemical potential is denoted with the letter $\tilde{\mu}_i$, as seen in equation (2.13). In this equation z is the number of charges of the ion, F is the Faraday constant and φ is the electrostatic potential. Note that when the charge z of a species is 0 (e.g. for molecules like H_2) the electrochemical potential equals the chemical potential. Since, just like with the chemical potential, any species in a thermodynamic system tending towards minimising the electrochemical potential, the gradient of the electrochemical potential $\nabla\tilde{\mu}_i$ is the driving force for the particle flux j_i (in mol/(m^2 s)).

$$j_i = -\,\text{const.}\nabla\tilde{\mu}_i \qquad\qquad j_i = -\,\frac{\sigma}{z^2F^2}\nabla\tilde{\mu}_i \tag{2.14}$$

Since the same driving force does not lead to the same particle flux in every material, another constant is needed that describes the material properties. This constant is σ, the ionic conductivity (in S/m). The negative sign in front of the constant stems from the fact that particles tend to travel in the direction where the electrochemical potential is getting smaller. This means that, in this direction, $\nabla\tilde{\mu}_i$ is negative but the particle flux j should be positive. Therefore a minus sign is needed. Equation (2.14) is widely applicable. With the right substitution, it describes both the conductance of electrons in a metal without diffusion (Ohm's law) but also diffusion without an electric field due to a gradient in concentration (Fick's first law). For a more in depth explanation, the lecture "Technical Electrochemistry" at TU Wien is highly recommended [34].

2.4.3 From Electrochemical Potential to Galvani Potential Difference

Like the chemical potential for normal chemical reactions, the electrochemical potential can be used to describe the equilibrium of an electrochemical reaction. The reaction will have reached equilibrium, when the electrochemical potential of the reactants and the products is equal. As an example, the reaction occurring on the anode of a hydrogen fuel cell (Figure 2.5b) will now be discussed.

$$H_2 \longleftrightarrow 2\,H^+ + 2\,e^- \qquad\qquad \tilde{\mu}_{H_2} = 2\tilde{\mu}_{H^+} + 2\tilde{\mu}_{e^-} \tag{2.15}$$

If the external circuit connecting the anode and the cathode electrically is disconnected, but the reactants (H_2 on the anode and O_2 on the cathode) are still supplied, then each of the half cell reactions (anode and cathode) will eventually reach equilibrium.

The potential difference that can then theoretically be measured between the two electrodes is called the open circuit voltage (OCV), electromotive force (emf), reversible voltage, or theoretical cell voltage U_{th} [31, 35]. Even though the value of the OCV depends on the full cell reaction (as shown later in 2.4.4), only the two respective half cell reactions are in equilibrium when the OCV is measured. The full electrochemical cell can not be in equilibrium because then ΔG would be zero [19] and therefore the OCV would be 0 V (explained later with equation (2.27)).

Lets now focus on the reaction occurring on the fuel cell anode (Figure 2.6). H_2 from the gas phase will continue to be split into H^+ and e^- on the catalyst coated electrode (left side of equation (2.15)) until equilibrium is reached, and the electrostatic forces prevent more H^+ from accumulating in the already slightly positively charged ionomer. This difference in electrostatic potential within one half cell is called the Galvani potential difference $\Delta\varphi$. In this case, it is the difference between the slightly positively charged ionomer and the slightly negatively charged electrode.

$\Delta\varphi$ can be calculated, assuming the half cell reaction has reached equilibrium (right side of equation (2.15)), by using the definitions of the electrochemical potential introduced before in

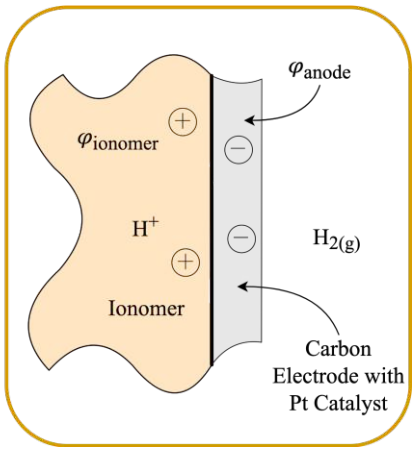

Fig. 2.6: Cutout of a hydrogen fuel cell anode for the calculation of $\Delta\varphi$ between the ionomer and the electrode

equation (2.13). $\tilde{\mu} = \mu + zF\varphi$ is used to go from equation (2.16) to (2.17) and $\mu = \mu^0 + RT\ln(x)$ is used to go from equation (2.19) to (2.20).

$$\tilde{\mu}_{H_2} = 2\tilde{\mu}_{H^+} + 2\tilde{\mu}_{e^-} \tag{2.16}$$

$$\mu_{H_2} = 2\mu_{H^+} + 2F\varphi_{\text{ionomer}} + 2\mu_{e^-} - 2F\varphi_{\text{anode}} \tag{2.17}$$

$$\mu_{H_2} = 2F\underbrace{(\varphi_{\text{ionomer}} - \varphi_{\text{anode}})}_{-\Delta\varphi_{\text{anode}}} + 2\mu_{H^+} + 2\mu_{e^-} \tag{2.18}$$

$$\Delta\varphi_{\text{anode}} = \frac{1}{2F}(2\mu_{H^+} + 2\mu_{e^-} - \mu_{H_2}) \tag{2.19}$$

$$\Delta\varphi_{\text{anode}} = \frac{1}{2F}(2\mu^0_{H^+} + 2RT\ln x_{H^+} + 2\mu_{e^-} - \mu^0_{H_2} - RT\ln x_{H_2}) \tag{2.20}$$

$$\Delta\varphi_{\text{anode}} = \frac{1}{2F}\left(\underbrace{2\mu^0_{H^+} + 2\mu_{e^-} - \mu^0_{H_2}}_{2F\Delta\varphi^0_{\text{anode}}} + RT\ln\left(\frac{(x_{H^+})^2}{x_{H_2}}\right)\right) \tag{2.21}$$

$$\Delta\varphi_{\text{anode}} = \Delta\varphi^0_{\text{anode}} + \frac{RT}{2F}\ln\left(\frac{(x_{H^+})^2}{x_{H_2}}\right) \tag{2.22}$$

The resulting equation (2.22) describes the Galvani potential difference's dependence on material properties ($\Delta\varphi^0$) and on activity/ concentration/ partial pressure of the reactants (x_{H^+} and x_{H_2}). This is the Nernst equation for an electrochemical half-cell.

$$\boxed{\Delta\varphi = \Delta\varphi^0 - \frac{RT}{zF}\ln\left(\frac{a_{\text{red}}^{\beta_{\text{red}}}}{a_{\text{ox}}^{\alpha_{\text{ox}}}}\right)} \tag{2.23}$$

The general form for this equation is given in equation (2.23). Extra care has to be taken to make sure the signs are correct for all three parts of this equation. The activity a can be replaced by a dimensionless concentration $x = c/c_o$ if the concentration is low.

2.4.4 From Galvani Potential Difference to Open Circuit Voltage (OCV)

Like mentioned before (section 2.4.3), the OCV is the voltage that can theoretically be measured between the two electrodes when each of the electrodes is supplied with reactants, both electrodes are in equilibrium, respectively, and the external current loop is disconnected so no current can flow. In actuality, however, "disconnected" usually means that there is a very high impedance (like a voltmeter to determine the OCV) in between the two electrodes. A very high impedance leads to very small currents. There are effects that lead to voltage losses even at these very small currents [6, p 40], as discussed later in the section about polarisation curves and overpotential (section 2.4.6). It is therefore unpractical and also not strictly necessary to measure the OCV because it can easily be calculated from thermodynamic data as shown in the following few equations for a PEM fuel cell.

$$\mathrm{H_2} \longleftrightarrow 2\,\mathrm{H^+} + 2\,\mathrm{e^-} \qquad \tilde{\mu}_{\mathrm{H_2}} = 2\tilde{\mu}^a_{\mathrm{H^+}} + 2\tilde{\mu}^a_{\mathrm{e^-}} \tag{2.24}$$

$$\frac{1}{2}\,\mathrm{O_2} + 2\,\mathrm{e^-} + 2\,\mathrm{H^+} \longleftrightarrow \mathrm{H_2O} \qquad \frac{1}{2}\tilde{\mu}_{\mathrm{O_2}} + 2\tilde{\mu}^c_{\mathrm{H^+}} + 2\tilde{\mu}^c_{\mathrm{e^-}} = \tilde{\mu}_{\mathrm{H_2O}} \tag{2.25}$$

$$\frac{1}{2}\,\mathrm{O_2} + 2\,\mathrm{H_2} \longleftrightarrow \mathrm{H_2O} \qquad \underbrace{\frac{1}{2}\mu_{\mathrm{O_2}} + \mu_{\mathrm{H_2}} - \mu_{\mathrm{H_2O}}}_{=\,-\Delta_r G} = \underbrace{2(\tilde{\mu}^a_{\mathrm{H^+}} - \tilde{\mu}^c_{\mathrm{H^+}})}_{=\,0\ \text{(if no current)}} - \underbrace{2(\tilde{\mu}^c_{\mathrm{e^-}} - \tilde{\mu}^a_{\mathrm{e^-}})}_{=\,2FU_{th}} \tag{2.26}$$

The electrochemical potential $\tilde{\mu}$ for uncharged molecules like $\mathrm{H_2}$ is equal to the chemical potential μ, as discussed before in section 2.4.2. Since there is no current flow through the external loop we can assume that there is no proton flux through the membrane. The general transport equation (2.14) tells us, that the flux is a constant multiplied by $\nabla\tilde{\mu}$. Therefore, if we assume the conductivity of the ionomer is not 0, $\tilde{\mu}_{\mathrm{H^+}}$ has to be constant throughout the ionomer and $(\tilde{\mu}^a_{\mathrm{H^+}} - \tilde{\mu}^c_{\mathrm{H^+}})$ has to be 0. The difference of the electrochemical potential between the two electrodes equals the OCV U_{th} [36, 35].

$$\boxed{U_{th} = \frac{-\Delta_r G}{zF}} \tag{2.27}$$

Equation (2.27) therefore allows to calculate U_{th} just using the Gibbs Free Energy of reaction $\Delta_r G$, the charge number z and the Faraday constant F. If the reaction we want to take place is non spontaneous $\Delta_r G > 0$, this theory still works but the theoretical voltage that needs to be applied is called the external electrolysis voltage $U_e = \frac{\Delta_r G}{zF}$. The minus sign is removed in this case.

The Galvani potential difference $\Delta\varphi$ for a single half cell can not be measured individually [19, p 47][35], but the OCV for a full electrochemical cell with two electrodes can be. We could now build and measure every possible combination of half cells imaginable and tabulate this data. Since this is unpractical and cell potentials are additive, if the same reference point is used, we instead measure and tabulate standard potentials U^0_{th}.

The standard potential for any half cell reaction is the OCV of this half cell with activity $a = 1$ against the standard hydrogen electrode at standard conditions (25 °C, 1 mol/L, 1 bar). The standard hydrogen electrode is a platinised platinum strip, submerged in acidified water where hydrogen gas is bubbled against the electrode. This electrode, by convention, has a potential of 0 V for any temperature [37]. Using these tabulated standard potentials, or thermodynamic data like the Gibbs Free Energy of reaction $\Delta_r G^0$, we can calculate the OCV for every imaginable combination of two half cells.

2.4.5 Concentration Dependence of the OCV - The Nernst Equation

Thermodynamic data is mostly only available for standard conditions ($\Delta_r G^0$) where the reactants have activity 1, but we want to be able to calculate the OCV for other concentrations of the reactants. The Nernst equation allows just that. It correlates the OCV of a cell U_{th} at non standard conditions with the tabulated OCV U_{th}^0 at standard conditions. We can easily obtain the Nernst equation for a full cell by plugging equation (2.12), which describes the concentration dependence of the chemical potential, into the just found formula for U_{th} (2.27).

$$U_{th} = \frac{-\Delta_r G}{zF} = \frac{-1}{zF}\left[\sum_{\text{products}} \alpha_i \mu_i - \sum_{\text{reactants}} \beta_j \mu_j\right] \tag{2.28}$$

$$U_{th} = \frac{-1}{zF}\left[\underbrace{\sum_{\text{products}} \alpha_i \mu_i^0 - \sum_{\text{reactants}} \beta_j \mu_j^0}_{=\Delta_r G^0 = -zFU_{th}^0} + \sum_{\text{products}} \alpha_i RT \ln x_i - \sum_{\text{reactants}} \beta_j RT \ln x_j\right] \tag{2.29}$$

$$U_{th} = U_{th}^0 - \frac{RT}{zF}\left[\sum_{\text{products}} \ln x_i^{\alpha_i} - \sum_{\text{reactants}} \ln x_j^{\beta_j}\right] \tag{2.30}$$

After this, in equation (2.29), we substitute the sums over the constant values for μ^0 with the voltage U_{th}^0 at standard conditions by using equation (2.27) again. As a last step to go from equation (2.30) to the Nernst equation for galvanic cells, (2.31) we use the logarithm rules to move the multiplicands (stoichiometric factors α und β) to the exponents and turn the sums into multiplications.

$$\boxed{U_{th} = U_{th}^0 - \frac{RT}{zF} \ln \frac{\prod_{\text{products}} a_i^{\alpha_i}}{\prod_{\text{reactants}} a_j^{\beta_j}}} \tag{2.31}$$

2.4.6 When Current Starts to Flow - Overpotential and Polarisation Curves

Up to this point the assumptions of an open circuit and equilibrium for each of the respective electrodes have been made to find equations describing the Galvani potential difference between one electrode and its electrolyte $\Delta\varphi$, the OCV U_{th}^0 at standard conditions and the OCV U_{th} at non standard conditions. Obviously, any real application is not going to be of any use if there is no current being produced by galvanic cells or no current being used to drive an electrolytic cell. This section will describe some effects that become relevant as current starts to flow. In other words: Up to this point, only the thermodynamic equilibrium of electrochemical reactions was discussed. In this section, the kinetics will be the main focus.

In practice, the voltage U that has to be applied to an electrolytic cell to let a reaction occur is always higher than the theoretical external electrolysis voltage U_e, and the voltage that is produced by a galvanic cell is always lower than the theoretical cell voltage U_{th} from thermodynamic calculations. [19, p 60]. This difference in voltage from the theoretical voltage to the actual voltage at a certain current is called the overpotential η. The overpotential can occur on any of the three main parts of an electrochemical cell (see equations (2.32) and (2.33)).

$$\text{Galvanic Cells: } U = U_{th} - \eta_{anode} - |\eta_{cathode}| - \eta_{\Omega} \tag{2.32}$$

$$\text{Electrolytic Cells: } U = U_{e} + \eta_{anode} + |\eta_{cathode}| + \eta_{\Omega} \tag{2.33}$$

In this equation, η_{Ω} is the overpotential occurring in the electrolyte. It is easy to understand that all of the components in equation (2.32) and equation (2.33) are necessarily occurring if there is any current flowing. When trying to find $\Delta\varphi$ under open circuit conditions in section 2.4.3, we assumed each of the half cell reactions in an electrochemical cell to be in dynamic equilibrium, meaning the rate of the forward reaction equals the rate of the backwards reaction. It therefore makes sense to call $\Delta\varphi$ under these equilibrium conditions $\Delta\varphi^{eq}$. Assuming that current is now flowing, one of the reaction rates necessarily has to be larger than the other, which means $\Delta\varphi$ between one electrode and it's electrolyte can not be $\Delta\varphi^{eq}$ anymore. Therefore, overpotential at the anode and the cathode side, respectively, is this difference in Galvani potential difference [35].

$$\Delta\varphi - \Delta\varphi^{eq} = \eta_{cathode} \text{ or } \eta_{cathode} \tag{2.34}$$

The overpotential in the electrolyte η_{Ω} is also necessarily non zero, because otherwise the electrolyte would have to conduct ions without any resistance.

It is also noteworthy, that the overpotentials on the anode η_{anode} and the cathode $\eta_{cathode}$ are completely unaffected by the respective other half cell. The total cell reaction is not relevant anymore for kinetic considerations. Only the individual half cell reactions have to be considered [35]. This means, for example, that the cathodic overpotential $\eta_{cathode}$ of a PEM hydrogen electrolyser is the same as the cathodic overpotential of an electrochemical hydrogen compressor, even though the second half cell for PEM elecrolysis is built differently and supplied with different reactants than the second half cell of an EHC (see section 2.5.1 or section 2.6). As they both use the same cathode, they will have the same cathodic overpotential (assuming the two cathodes are really identical).

2.4.6.1 Polarisation Curves

A graph depicting the relationship between cell voltage, current density and indirectly also overpotential, is called a polarisation curve. The use of the term polarisation in this regard is sometimes considered misleading [31, p. 45]. Nevertheless it is widely used in literature and will therefore be used in this work as well. Examples for polarisation curves can be found in Figure 2.7. When trying to find equations that describe the amount of overpotential at a certain current (or vice versa), it seems to be more common to classify the overpotentials by the phenomena that caused them instead of the location where they occur. Possible causes of overpotential are [6, p 40]:

- Kinetics of the electrochemical reactions - activation overpotentials
- Internal electrical and ionic resistance - ohmic losses
- Difficulties in getting the reactants to reaction sites - concentration polarisation
- Internal (stray) currents
- Crossover of reactants

All of these individual effects together, assuming other factors like concentration of the reactants or temperature are constant, lead to a certain total overpotential $\eta(i)$ like depicted in Figure 2.7 which depends on the current density i in $\mathrm{mA/cm^2}$.

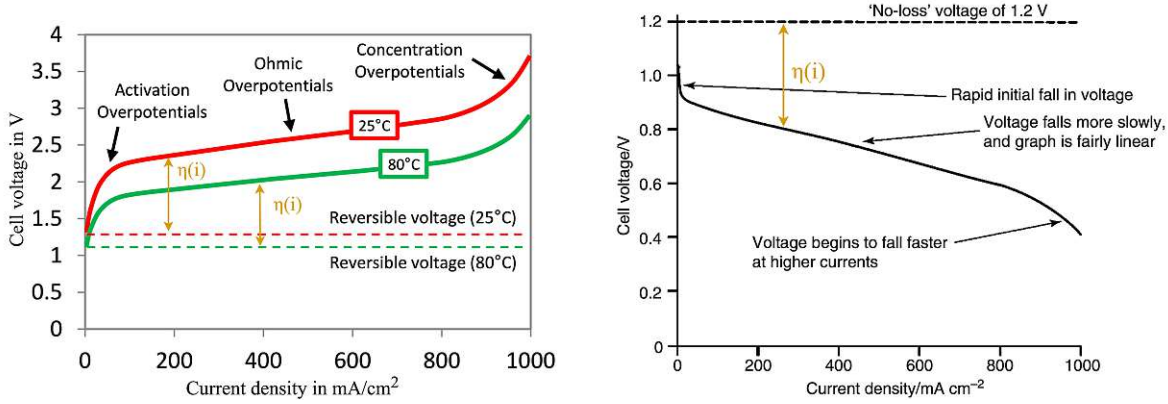

(a) Polarisation curves for alkaline water electrolysis at two different temperatures adapted from [38]. The difference between the two dashed lines is because of the effect of temperature on the OCV that has already been discussed in section 2.4.5

(b) Polarisation curve for a PEM hydrogen fuel cell adapted from [31]

Fig. 2.7: Both of the exemplary polarisation curves show a similar pattern for $\eta(i)$: Logarithmic growth at very low current densities followed by a mostly linear increase at medium current densities and exponential growth at high current densities.

The individual reasons for overpotential listed above will now briefly be discussed in the following. The focus will be placed on the mathematical description and the possible factors of influence to the respective causes of overpotential. A more in depth explanation can be found elsewhere [6, 31, 35, 39].

2.4.6.2 Activation Overpotential

The logarithmic growth of overpotential at low current densities seen in Figure 2.7 is caused by activation losses. Activation losses or activation overpotentials occur both at the anode and at the cathode [6, p. 48]. They are results of limiting reaction kinetics at the electrode surfaces. The total activation overpotential of a cell is the sum of the anode and the cathode activation overpotential.

The mathematical model used to describe activation overpotential at one electrode is the Butler-Volmer equation (2.35). The Butler-Volmer equation can describe activation overpotentials when ion transfer at the electrode surface is the rate limiting step for the reaction [35]. This is the case for both electrodes of PEM fuel cells. A derivation for this equation can be found in [6] or [35].

$$i = i_0 \left(e^{\frac{|z|F\alpha\eta}{RT}} - e^{-\frac{|z|F(1-\alpha)\eta}{RT}} \right) \tag{2.35}$$

In equation (2.35), z is the number of charges, F is the Faraday constant, R is the ideal gas constant, η is the anodic or cathodic overpotential, α is a symmetry factor and i_0 is the so called exchange current density. Exchange current density is one of the most important parameters for describing the kinetics of fuel cells [40] and electrolysis [39]. It is therefore also vital for describing the kinetics of EHCs. The exchange current density i_0 is an electrochemical pendant to the rate constant r_0 for chemical reactions [6]. When there is no net reaction occurring in a half cell ($\Delta\varphi{=}\Delta\varphi^{eq}$), the reaction actually still proceeds in both directions at the same rate.

The rate at which the reaction proceeds in this case is called the exchange current density i_0. In contrast to the rate constant r_0, the exchange current density i_0 is concentration dependant. An overview of other factors that influence the exchange current density can, for example, be found in [6, p. 38], [41, p. 55] or [31, p. 51]. Because ion transfer is the rate limiting step, the general Butler-Volmer equation (2.35) is valid both for the anode and the cathode of PEM fuel cells [6] and PEM electrolysis [41].

The two exponential terms in the Butler-Volmer equation (2.35) describe the forward and backwards reaction on the *same electrode / same half cell*. When $i = i_0$, the two exponential terms become equal two each other, i.E. the forward and backwards reaction at one electrode occur at the same rate.

One more detail that is worth mentioning (because it is regularly encountered in literature about this subject) is the so called Tafel equation and the Tafel slope that it describes. The Tafel equation was an empirically found relationship [6, p. 41], which also describes the relationship between activation overpotential and current. However, by comparing coefficients, we can determine, that the Tafel equation is equivalent to a simplified version of the Butler-Volmer equation: Assuming the overpotential η is not too close to 0 V, one of the two exponential terms in the Butler-Volmer equation (2.35) is much larger than the other, which can therefore be neglected. The sign of the overpotential η determines which of the two exponential terms can be neglected and wether or not the electrode in question is currently working as an anode or a cathode. After neglecting one of the exponential terms and taking the natural logarithm, we arrive at the Tafel equation (2.36).

$$\eta \text{ negative: } \ln i = \ln i_0 - \frac{|z|F(1-\alpha)\eta}{RT} \qquad \eta \text{ positive: } \ln i = \ln i_0 + \frac{|z|F\alpha\eta}{RT} \tag{2.36}$$

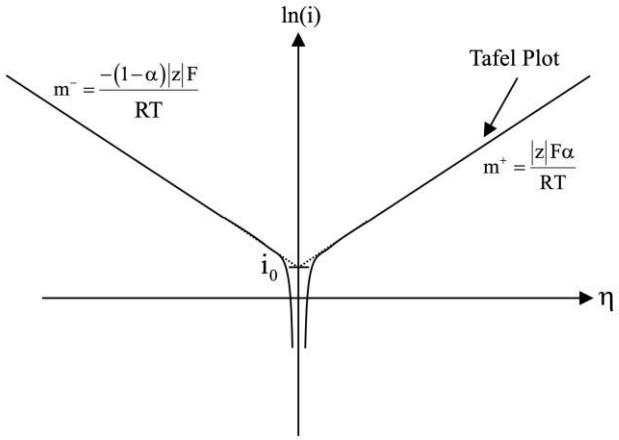

Fig. 2.8: The Tafel plot is a convenient way to determine the exchange current density i_0 (from the location of crossing the y axis) and, if it is not known beforehand, the charge number z (from the slopes m^+ and m^- of the positive and negative linear function). Note that the Tafel equation is a simplification of the Butler-Volmer equation and not valid for very low overpotentials. Also note that this is the Tafel plot for one electrode acting as an anode or cathode. It is not a plot of a full cell. Figure adapted from [35]

In PEM hydrogen fuel cells, the anode exchange current density is several orders of magnitude larger than the cathode exchange current density ($\sim 10^{-3}$ A/cm^{2}Pt on the H_2 side versus $\sim 10^{-9}$ A/cm^{2}Pt on the O_2 side at 25 °C and 1 bar with acid electrolyte) [6]. Therefore, the

anode's impact on activation overpotential is often ignored and the total activation overpotential for PEM hydrogen fuel cells is approximated by only including the cathode side activation overpotential [6, 40] [31, p. 50]. Usually, activation losses make up the largest part of the total losses at any current density by far for PEM fuel cells.[6, p. 48]. However, this does not seem to be the case for EHCs, because they possess the high exchange current density of the fuel cell anode on both the anode and the cathode side [42].

Possible ways to increase the exchange current density i_0 and decrease the activation overpotential are: [31]

+ Increase temperature
+ Increase electrode surface area or roughness
+ Increase the reactant concentration or pressure
+ Increase the amount of catalyst or use more effective catalysts

2.4.6.3 Ohmic Losses

Ohmic losses are responsible for the mostly linear increase of overpotential $\eta(i)$ with increasing current (Figure 2.7) at medium current densities. They occur because of the resistance to the flow of ions and electrons in the electrolyte and the electrically conductive parts of an electrochemical cell, respectively. They are conceptually the easiest losses to understand and also easy to describe mathematically.

$$i = \frac{\eta_\Omega}{r_\Omega} \tag{2.37}$$

Equation (2.37) is essentially Ohm's law using the total area specific cell resistance r_Ω in $\Omega\,\mathrm{cm}^2$ and the ohmic overpotential η_Ω in V. The total cell resistance can be further subdivided into the individual parts of the resistance. The ionic resistance of the electrolyte r_{Ω_i}, sometimes given by the inverse as ionic conductivity σ_{ion} in S/cm=$1/(\Omega\,\mathrm{cm})$, the contact resistance r_{Ω_c} and the electronic resistance r_{Ω_e}. [6, p. 45].

$$r_\Omega = r_{\Omega_i} + r_{\Omega_e} + r_{\Omega_c} \qquad r_\Omega = \frac{d}{\sigma_{ion}} + r_{\Omega_e} + r_{\Omega_c} \tag{2.38}$$

The distance between the two electrodes d can be used to find the expected resistance of the electrolyte from the more commonly given conductivity value. For PEM, this distance is the membrane thickness. In fuel cell systems, the electronic resistance r_{Ω_e} is usually almost negligible even if less conductive materials like graphite or graphite/polymer composites are used for the current collectors. Ionic and contact resistances are approximately of the same order of magnitude [6, p. 45]. For minimising the ohmic losses, each of the three shares of resistances should be minimised. The resistance of the electrolyte (i.e. the membrane) used for PEM fuel cells and electrolysis (e.g. Nafion$^{\mathrm{TM}}$) is strongly dependant on temperature and humidity. In contrast to the conductivity of metals for electrons, their conductivity rises with rising temperature.

Possible ways to decrease the resistance and therefore the ohmic losses are:

+ Attempt to get clamping pressure on membrane electrode assembly (MEA) uniform to reduce contact resistance r_{Ω_c} [43]
+ Increase temperature to increase σ_{ion} of the membrane [6, p. 82]

+ Increase membrane humidity for better proton conductivity and increasing σ_{ion} [6, p. 81]
+ Decrease membrane thickness. Usually thinner is better even though this is a double edged sword. Thinner membranes reduce r_{Ω_i} but tend to increase r_{Ω_c} and undesired back diffusion, especially at high pressures [43].
+ Increase hydrogen partial pressure [44]

2.4.6.4 Concentration Polarisation

Concentration polarisation is a common phenomenon encountered in many different fields. Baker [27] describes concentration polarisation in membrane separation technology as follows:

> *In membrane separation processes, a gas or liquid mixture contacts the feed side of the membrane, and a permeate enriched in one of the components of the mixture is withdrawn from the downstream side of the membrane. Because feed mixture components permeate at different rates, concentration gradients can form in the fluids on both sides of the membrane. In this case, the concentrations at the membrane surfaces are not the same as the bulk fluid concentrations. This changes permeation through the membrane. The phenomenon is called concentration polarization.*

A very similar effect can also occur with pure substances. If we assume that, very close to the surface, the reactants are only transported to the reaction sites by diffusion through a thin fluid layer, the maximum current density becomes limited by the speed of diffusion. Assuming steady state operation, the amount of reactant being used at the electrode has to be equal to the diffusive flux of reactants being transported to the electrode from the bulk fluid. Therefore these types of losses are sometimes also called mass transfer losses. The diffusive transport to the electrode can be described by the one dimensional equation of diffusion (Fick's first law) (2.39).

$$J = -D\frac{c_S - c_B}{\delta}A \tag{2.39}$$

In Fick's first law (2.39), D is the diffusion coefficient of the species that has to be transported to the membrane surface in the surrounding fluid, δ is the film thickness of the boundary layer and c_S and c_B are the surface and bulk concentration of the diffusing species respectively. The amount of this species being used by an electrochemical reaction, as described in section (2.4.1), is given by the Faraday equation (2.11). Setting J (in mol/s) from Fick's first law (2.39) equal to $\dot{N}$ (in mol/s) from the Faraday equation (2.11), we arrive at an equation describing the dependence of the electrode surface concentration to current and bulk concentration. [6, p. 46]

$$i = \frac{DzF(c_B - c_S)}{\delta} \tag{2.40}$$

When the current density i rises, the surface concentration c_S drops. At some current density the surface concentration will reach 0. This current density is called the limiting current density i_L [6]

$$i_L = \frac{DzFc_B}{\delta} \tag{2.41}$$

For finding an equation linking the overpotential caused by mass transfer limitations η_{conc} to current density, we can use the Nernst equation (2.31). Assuming the second electrode of the electrochemical cell has a constant surface concentration c_K we can apply the Nernst equation to this full electrochemical cell two times for two extreme cases:

- Surface concentration on the limiting electrode = bulk concentration c_B
  surface concentration on the other electrode = c_K
- Surface concentration on the limiting electrode = the lower surface concentration c_S
  surface concentration on the other electrode is still = c_K

This leads to equation (2.43)

$$\eta_{conc} = \left(\cancel{U^0_{th}} - \frac{RT}{zF}\ln\left(\frac{c_K}{c_B}\right)\right) - \left(\cancel{U^0_{th}} - \frac{RT}{zF}\ln\left(\frac{c_K}{c_S}\right)\right) \tag{2.42}$$

$$\eta_{conc} = \frac{RT}{zF}\ln\left(\frac{c_B}{c_S}\right) \tag{2.43}$$

Combining (2.43) with equations (2.41) and (2.40) to eliminate the concentrations, we arrive at a relationship between concentration overpotential η_{conc} and current density i.

$$\eta_{conc} = \frac{RT}{zF}\ln\left(\frac{i_L}{i_L - i}\right) \qquad i = i_L - i_L e^{-\left(\frac{zF\eta_{conc}}{RT}\right)} \tag{2.44}$$

This model, however, assumes that the whole electrode surface area is uniform and reaches the limiting current density i_L at exactly the same time leading to a very sharp increase in overpotential close to this limiting current density. Since, on a real electrode, the current density and other factors are not perfectly uniform over the whole surface, some parts of the electrode might already be at their limiting current density while others could still go higher. Real current to mass transfer overpotential curves therefore start rising earlier and are less steep towards a specific limiting current density. An empirical model is often used instead of equation (2.44) to better describe the exponential relationship between current density and concentration overpotential [31, 6]. This relationship is given by equation (2.45)

$$\eta_{conc} = me^{ni} \tag{2.45}$$

m and n in equation (2.45) have to be determined experimentally for a specific cell.
Possible ways to decrease the mass transfer losses/concentration polarisation are:

+ Increase (turbulent) mixing at the membrane surface to decrease the boundary layer film thickness δ by increasing the feed velocity or introducing membrane spacers to promote mixing with the bulk phase [27]
+ Increase diffusion coefficient by increasing temperature
+ Increase H_2 concentration on the feed side

2.4.6.5 Back Diffusion, Fuel Crossover and Internal Currents

Fuel crossover and back diffusion describe the undesired permeation of molecules through the membrane. Internal currents are stray currents where the electrons don't take the desired path

through the external current loop but somehow pass through the membrane directly from anode to cathode. All three of these adverse effects lead to the same outcome and can be described by the same equation. For example, with fuel crossover, some of the H_2 supplied to a PEM fuel cell anode will not react at the anode to form $2\,H^+$ and $2\,e^-$ but instead diffuse to the cathode and react there to form H_2O directly. Each H_2 molecule passing through the membrane like this, reduces the maximum current the fuel cell can produce by two electrons. Looking at it from the outside, two electrons directly taking the path through the membrane instead of the external loop, is an equivalent process. Back diffusion is an effect that leads to a similar outcome in an electrochemical hydrogen compressor. Hydrogen, that was already pumped from a lower pressure anode side to a higher pressure cathode side can diffuse back to the anode and therefore has to be pumped through the membrane a second time therefore reducing the current efficiency.

Even though the membranes usually used for PEM fuel cells and electrolysis are practically impermeable to reactant gases and electrically non conductive, some trace amounts will diffuse along the concentration/pressure gradient [6, p. 42]. Under normal operation, these losses may be considered insignificant because they are usually orders of magnitude smaller than the operating currents (a few mA/cm^2) [31]. However, at low current densities or under open circuit conditions, these losses can become a significant fraction of the total losses. These effects are one of the main reasons why the OCV in real fuel cells is significantly lower than U_{th} calculated from thermodynamic data like shown in section 2.4.4. Even very low loss currents i_{loss} already lead to significant overpotentials because of the exponential nature of activation overpotentials that dominate this region of the polarisation curve. Dicks and Rand [31, p. 53] give some numerical examples for these types of overpotentials.

$$\text{For PEM electrolysis/EHC:} \qquad i_{tot} = i_{ext} - i_{loss} \tag{2.46}$$

$$\text{For PEM fuel cells:} \qquad i_{tot} = i_{ext} + i_{loss} \tag{2.47}$$

Equations (2.46) and (2.47) introduce a correction term i_{loss} that is either added [6] to the current passing through the external circuit i_{ext} in the case of PEM fuel cells, or subtracted [45] from the current passing through the external loop i_{ext} for PEM hydrogen electrolysis or EHCs.

For high temperature H_2 fuel cells, fuel crossover is less of an issue because of their higher exchange current density [31]. Fuel cells operating at higher current densities have a lower hydrogen concentration on the electrode surface (as discussed in section 2.4.6.4 about concentration polarisation). Therefore the effects of fuel crossover can often be neglected at higher current densities. [6]

Hydrogen back diffusion in PEM electrolysis is primarily described by the solution diffusion model (see section 2.3). It occurs from cathode to anode [41, p. 128] and is therefore strongly dependent on the difference of hydrogen partial pressure over the membrane. Similar results were reported from experiments with EHCs [45, 46]

Possible ways to decrease the losses due to back diffusion in EHCs are:

+ Use membrane material with lower diffusion coefficient for hydrogen [47]
+ Increase membrane thickness [47] (see section 2.4.6.3 for problem)

2.4.7 Energy Requirement for the Compression of Gasses

No machine works at 100 % efficiency and every process has losses attached to it. Calculating the energy requirements for 100 % efficient processes is still very sensible because it gives a reference to compare the real processes too. This section should give an overview of the energy

requirements for ideal adiabatic and isothermal compression as well as the energy required for compression in real world processes. It should also display why electrochemical hydrogen compression is an attractive alternative compression technology to pursue.

Reversible Isothermal Compression of an Ideal Gas

The first law of thermodynamics for an open system (system boundary as shown in the top right of Figure 2.9), after neglecting kinetic and potential energy, is given in equation (2.48).

$$q_{12} + w_{t12} = h_2 - h_1 \tag{2.48}$$

Expanding the enthalpy h to $u + pv$ by using the definition of enthalpy it can easily be shown that, for an ideal gas, the difference in enthalpy for an isothermal process turns out to be 0: Applying the equation of state for an ideal gas shows that $p_1 v_1 = p_2 v_2$. Similarly, using the caloric equation of state we find that $u_1 = u_2$. Therefore, equation (2.48) can be simplified to (2.49).

$$-q_{12} = w_{t12} \tag{2.49}$$

Equation (2.49) tells us that all the work we put into the system for isothermal compression of an ideal gas leaves the system as heat energy. This equation also holds true for irreversible compression. In this case, w_{t12} would also include an irreversibility term. For now, let us not consider irreversibility and try to find an equation describing the work required for ideal compression w_{t12}. It can be calculated using the integral $\int_1^2 v\ dp$. This integral, again because $p_1 v_1 = p_2 v_2$, can be substituted with $\int_1^2 p\ dv$ (see Figure 2.9).

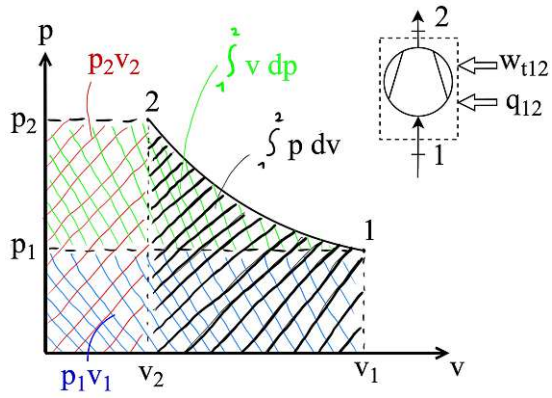

Fig. 2.9: A schematic representation of the relationship between the volume work done on a closed system $\int_1^2 p\ dv$ and the work done on an open system $\int_1^2 v\ dp$. As shown here, $\int_1^2 v\ dp = \int_1^2 p\ dv + p_2 v_2 - p_1 v_1$.

$$w_{t12} = -\int_1^2 p\ dv \tag{2.50}$$

$$w_{t12} = -\int_1^2 \frac{RT}{v}\ dv \tag{2.51}$$

$$w_{t12} = -RT \ln \frac{v_2}{v_1} \tag{2.52}$$

$$w_{t12} = -RT \ln \frac{RTp_1}{RTp_2} \tag{2.53}$$

$$w_{t12} = RT \ln \frac{p_2}{p_1} \tag{2.54}$$

Equation (2.54), describing the work for isothermal compression, looks very familiar because it resembles the Nernst equation (2.31) derived from the electrochemical potential in section 2.4.4. It will later (in section 2.6.1) be demonstrated that equation (2.54) does not just resemble the Nernst equation, but is actually identical to the equation describing electrochemical hydrogen compression which is derived from the Nernst equation.

Reversible Adiabatic Compression of an Ideal Gas

Using the first law of thermodynamics for open systems (system boundary again as shown in the top right of Figure 2.9) and knowing the process is adiabtic, equation (2.48) can this time be simplified to (2.55)

$$w_{t12} = h_2 - h_1 \tag{2.55}$$

For finding the equation describing the work to perform reversible adiabatic (=isentropic) compression on an ideal gas (= equation 2.56), we need a number of equations from thermodynamics:

- The caloric equation of state for an ideal gas ($du = c_v dT$)
- The definition of enthalpy ($h = u + pv$)
- The thermal equation of state for an ideal gas ($pV = nRT$)
- The relationships between the heat capacity at constant pressure c_p, the heat capacity at constant volume c_v, the isentropic exponent κ and the ideal gas constant R ($\kappa = c_p/c_v$ and $c_p - c_v = R$)

A full derivation can be found in [48, p. 101-105], a partial one in [49, p. 26]

$$w_t = RT_1 \frac{\kappa}{\kappa - 1} \left(\left(\frac{p_2}{p_1} \right)^{(\kappa-1)/\kappa} - 1 \right) \tag{2.56}$$

Mechanical compressors (without gas cooling) operate approximately adiabatically and therefore heat up the compressed gas significantly in the process. One solution to this problem is using staged compressors that cool the compressed gas in-between the stages (see Figure 2.10).

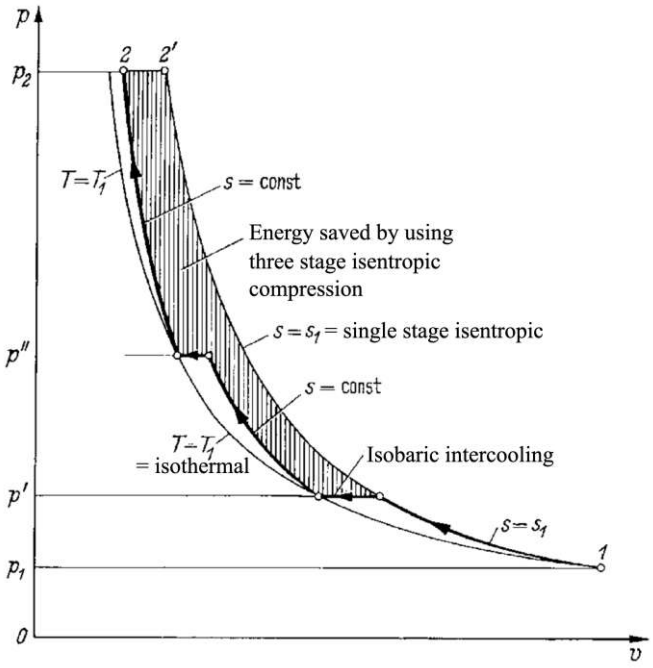

Fig. 2.10: p-v diagram to visualise the energy required for isentropic compression, isothermal compression and multi-stage isentropic compression. Multistage isentropic compression with isobaric intercooling requires less energy than single stage isentropic compression and approaches the energy required by isothermal compression for $n_{intercooler} \to \infty$. However, due to irreversibilities and imperfections, real mechanical multistage compressors use significantly more energy and, depending on compressor type and operating conditions, also still more than the ideal adiabatic work. Increasing the number of stages on a compressor obviously also increases the mechanical complexity and the price. Figure adapted from [50, p. 412]

Energy Requirements for Real Compression Systems

Figure 2.11 includes plots of the work required for reversible adiabatic and reversible isothermal compression of H_2 (equations (2.54) and (2.56)) over a range of compression ratios (p_2/p_1). The plot also includes the, substantially lower, work required for the reversible adiabatic compression of air. The drastic difference between air and H_2 can mostly be explained by the significantly lower density of hydrogen and the energy consumption being displayed as kW h/(kg K).

Treating H_2 as an ideal gas and assuming κ is constant for any pressure/temperature is obviously an oversimplification, but it is still a good display for the potential energy saving isothermal compression of hydrogen can offer since real gas effects also affect other methods of hydrogen compression. Graphs similar to Figure 2.11, comparing reversible isothermal compression with reversible adiabatic compression or adiabatic compression with a certain efficiency are often included in publications about EHCs. [55, 56, 57]. And while this is not wrong, it should still be presented with a little more nuance. The reversible adiabatic compression in Figure 2.11 assumes compression in a single stage. When adiabatically compressing H_2 from 1 bar to 200 bar in a single stage with an inlet temperature of 100 °C, the outlet temperature would already exceed 1000 °C [56]. Therefore any real mechanical compressor built for such high compression ratios, would use a multistage design with intercooling (see Figure 2.10).

Adding even more confusion to the topic of energy efficiency is that values for energy efficiency in % are often given without any information on whether this efficiency is calculated as an

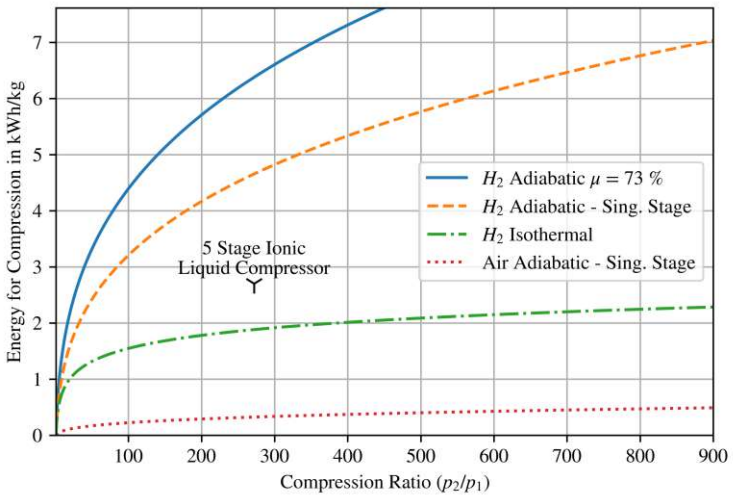

Fig. 2.11: Plots of energy requirements for the compression of gasses. The dashed line, representing reversible single stage adiabatic compression, uses equation (2.56) with properties of hydrogen ($\kappa = 1,4$ [51]; R =1,1456 $\times 10^{-3}$ kW h/(kg K)[52]; T_1 =293,15 K). The dash-dotted line, representing isothermal compression, uses equation (2.54) and the same constants for H_2 where needed. The dotted line, representing reversible adiabatic compression of air uses properties of air ($\kappa = 1,4$ [53]; R =7,974 $\times 10^{-5}$ kW h/(kg K)[52]. Data for the marker showing the energy consumption of an ionic liquid compressor is taken from [51]. The solid line represents adiabatic compression of H_2 with an efficiency of 73 %, a typical efficiency for linear compressors (a common type of mechanical compressors)[54]

isothermal efficiency ($w_{t,isothermal}/w_{t,real}$) or an isentropic efficiency ($w_{t,isentropic}/w_{t,real}$). E.g. Sdanghi et al. [54] tells us that "hydrogen reciprocating compressors, like diaphragm compressors, have an average efficiency of around 45%". Since we are talking about mechanical compressors, one could assume this efficiency is an adiabatic efficiency. This would mean the energy requirement for the average mechanical compressor is significantly higher than even the blue line in Figure 2.11. A terrible efficiency. However, the source literature [58] clarifies that the 45% are actually an isothermal efficiency.

Mechanical compressors are currently the most widespread technology used for hydrogen compression. It is a mature technology and several improvements have been made to overcome some of their weaknesses in regards to hydrogen.[54]. However, many drawbacks like mechanical complexity, vibration, noise and the comparatively low energy efficiency remain. Alternative concepts like the EHC or ionic liquid compressors (e.g. by Linde plc - see datapoint in Figure 2.11) try to solve some of these drawbacks. One benefit however, that only EHCs possess, is the ability to perform compression and purification of hydrogen even from very low concentration sources in a single unit and without any moving parts. The potential of not needing a separate purification device like pressure swing adsorption or cryogenic purification before the compression step can greatly simplify processes or even make hydrogen sources viable that were previously not worth recovering and just burned for their energy content. Not to mention that these purification methods (pressure swing adsorption and cryogenic purification) possibly need another compression step before the actual purification. The EHC could therefore reduce a three-step process into into a single step one.

2.5 Electrochemistry Applications with a Focus on Hydrogen

Electrochemistry has a vast number of applications like batteries, galvanic surface treatments, production of base chemicals or electrochemical sensors, and is therefore used in almost every major industry. The applications discussed here, however, will only revolve around hydrogen. Even more specific, it will concentrate on the production of hydrogen via water electrolysis and the conversion of the chemical energy stored in the H_2 molecule into electrical energy with the use of hydrogen fuel cells.

2.5.1 Water Electrolysis

Water electrolysis is the process of splitting H_2O into H_2 and O_2 in an electrochemical cell using an externally applied voltage. Every electrolyser consists of the same basic elements: two electrodes, where the half-cell reactions occur, and an electrolyte separating the two electrodes, that is capable of transporting anions and/or cations. The half cell reactions that occur at the electrodes depend on the process used. The four most common processes for dedicated H_2O-electrolysis are:

- Alkaline electrolysis (Figure 2.12a)
- Anion exchange membrane (AEM) electrolysis (also Figure 2.12a)
- Solid oxide electrolysis (Figure 2.12b)
- Polymer electrolyte membrane (PEM) electrolysis (Figure 2.12c)

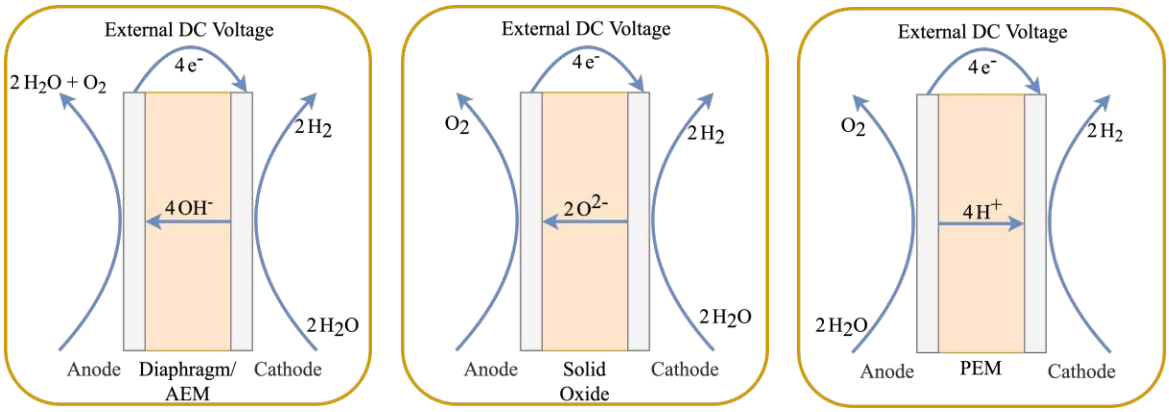

(a) Both in alkaline electrolysis and AEM electrolysis, the electrolyte conducts OH^- ions

(b) In solid oxide electrolysis, the electrolyte conducts O^{2-} ions at high temperatures

(c) In PEM electrolysis, the electrolyte selectively conducts H^+ ions

Fig. 2.12: Schematic representations of the four main electrolyser types that are being used or researched

These four types will now be discussed in more detail.

Alkaline and AEM H_2O Electrolysis

Water electrolysis under alkaline (20 %–40 % KOH) conditions is a very mature technology that has been used for around 100 years [59]. About 62 % of all the hydrogen produced via water electrolysis today (2020) is produced by alkaline electrolysis. The remaining production is almost

exclusively produced with PEM electrolysis. This fraction, however, has been changing a lot in recent years. In 2015, alkaline electrolysis still made up about 84 % of all dedicated water electrolysis. From 2015 to 2020, the global installed alkaline hydrogen electrolysis capacity has grown by about 31 %. In the same timespan, PEM electrolysis has grown by about 370 % [12]. This slower growth of alkaline compared to PEM electrolysis could be caused by the following downsides of classical alkaline electrolysis:

The porous diaphragm used to separate the anode and cathode, while allowing OH^- transport, is permeable to the KOH solution [14]. This porosity also allows H_2 from the cathode side to permeate to the O_2 (anode) side [19, p. 206]. At lower production rates, this can even lead to H_2 concentrations on the O_2 side reaching the lower flammability limit of 4 % [59]. Alkaline water electrolysis is also limited to the comparatively low pressure of about 30 bar on the H_2 side [19, p. 207],[14] and certain minimum and maximum voltage limits have to be observed due to corrosion concerns. Altogether, these restrictions to the operational range make alkaline electrolysis less ideal for the use with intermittent renewable energy.

Anion exchange membrane electrolysis offers a potential solution to many of the problems that come with alkaline electrolysis, without inheriting the catalyst drawback of PEM electrolysis (see 2.5.1 - PEM H_2O electrolysis). It does this, by replacing the diaphragm with a thin, dense, non-porous polymer membrane that is anion conductive [59]. However, the real world feasibility of AEM electrolysis still has to be proven while both PEM and alkaline electrolysis are already well established and widely used technologies.

H_2 reduction (cathode)	$4\,H_2O + 4\,e^- \longrightarrow 2\,H_2 + 4\,OH^-$	$U^0_{red} = -0{,}828\,V$	(2.57)
O_2 oxidation (anode)	$4\,OH^- \longrightarrow O_2 + 4\,e^- + H_2O$	$U^0_{ox} = -0{,}401\,V$	(2.58)
Full cell reaction	$2\,H_2O \longrightarrow 2\,H_2 + O_2$	$U^0_e = -1{,}230\,V$	(2.59)

Equations (2.57) and (2.58) show the reactions occurring on the cathode side and anode side in both alkaline and AEM electrolysis together with their respective standard electrode potential for the half cell reaction. Equation (2.59) shows the reaction for the full cell together with its external electrolysis voltage at standard conditions U^0_e . A schematic representation of an alkaline/AEM electrolysis cell is shown in 2.12a.

Solid Oxide H_2O electrolysis

Solid oxide electrolysis is, like represented in Figure 2.12b, characterised by the use of a solid ceramic electrolyte that conducts O^{2-} ions. This type of fuel cell is usually operated at temperatures of around 800 °C. The elevated temperature brings one major advantage and a host of disadvantages for water electrolysis. Like mentioned under 2.4.4, the voltage required for water splitting is determined by the difference in Gibbs free energy ΔG. This leads to the advantage of solid oxide electrolysis at elevated temperature. When temperature rises, the factor $T\Delta S$ grows a lot faster than ΔH. So the voltage required for water splitting at elevated temperature is significantly lower. [19, p. 204]. This lower voltage leads to a lower consumption of electrical energy for water splitting compared to alkaline or PEM elecrolysis. (about 3 kW h/m^3 compared to about 5 kW h/m^3 on average for PEM or AEM electrolysis [19, 14]). Some of the drawbacks of solid oxide electrolysers are the limitation to a low cell pressure of about 1 bar, the long ramp up time for heating up to working temperature, the low flexibility in load range, the low expected life span and the requirement for an additional source of energy in the form of heat energy. In conclusion, solid oxide electrolysis is currently not a well-suited method for many hydrogen production needs and especially unsuited for the production of H_2 with intermittent energy sources from renewable energy sources. Many of these things might change with further research and development in the future.

PEM H_2O electrolysis

Polymer electrolyte membrane electrolysis, like mentioned above, has seen rapid growth in its adoption in recent years. Compared to the previously mentioned technologies this electrolyser type, that was first introduced by General Electric in 1966, has numerous advantages [19, p. 207]. Among these advantages are:

- The ability to operate with a wide range of current densities
- Fast response to dynamic conditions
- A compact and modular form-factor
- The possibility for a high H_2 discharge pressure of up to 350 bar
- The absence of corrosive liquids [41, p. 37]

However, compared to alkaline electrolysers with reported lifetimes of 20 to 30 years [41, p. 37], [14], the mere five years that are currently being reported as lifetimes for PEM electrolysers are very short. PEM electrolysers are currently (2020) about 50 %–60 % more expensive than alkaline electrolysers [14]. Lastly, there is the problem of PEM electrolysers requiring platinum group metals as catalysts. Like indicated in equation (2.60) and equation (2.61), the hydrogen evolution reaction (HER) requires platinum as a catalyst, and the oxygen evolution reaction (OER) requires iridium as a catalyst. For the discussion of the working principles of an electrochemical hydrogen compressor (see section 2.4.6.2 about activation overpotentials or section 2.6.1 about OCV of EHCs) it is already important to note at this time, that during electrolysis the limiting reaction is the OER. The kinetics of the HER are several orders of magnitude faster than the OER.

$$\text{H}_2 \text{ reduction (cathode)} \quad 4\,\text{H}^+ + 4\,\text{e}^- \xrightarrow[\text{Pt}]{\text{HER}} 2\,\text{H}_2 \qquad U^0_{red} = \ 0{,}00\,\text{V} \tag{2.60}$$

$$\text{O}_2 \text{ oxidation (anode)} \quad 2\,\text{H}_2\text{O} \xrightarrow[\text{Ir}]{\text{OER}} 4\,\text{H}^+ + 4\,\text{e}^- + \text{O}_2 \qquad U^0_{ox} = \ 1{,}23\,\text{V} \tag{2.61}$$

$$\text{Full cell reaction} \quad 2\,\text{H}_2\text{O} \longrightarrow 2\,\text{H}_2 + \text{O}_2 \qquad U^0_e = -1{,}23\,\text{V} \tag{2.62}$$

The International Renewable Energy Agency (IRENA) noted in their 2020 report [14] that, for the individual stack, catalyst coated membranes (CCMs) represent an important part of the cost. They also note, however, that put into context of a full PEM electrolysis system, the platinum group metals make up less than 10 % of the total costs.

There are potential future lower cost alternatives to Pt for the HER [41, p. 85], and the required amount of catalyst per unit area has dropped significantly since the early days of PEM research (e. g. from up to 28 mg/cm^2 to 0,2 mg/cm^2 for Pt) [6, p. 93].

The OER, requiring iridium, is more problematic in that sense: “Efforts have also been made in the scientific community to find OER alternatives to IrO_2 but, of course, the task is more challenging and, to date, no viable solution to this problem has been proposed” [41, p. 89]. With the prices for iridium currently at around 169 000 €/kg compared to about 47 000 €/kg in January 2020 (data from Umicore [60] on May 06, 2022) the cost analysis might look drastically different today compared to 2020 when the IRENA report [14] was released. But that is to be discussed elsewhere.

2.5.2 Hydrogen Fuel Cells

Hydrogen fuel cells are devices that directly oxidise H_2 with O_2 to form H_2O and produce electricity. Like mentioned in section 2.2, fuel cells are not limited by the efficiency of the carnot

cycle, since they don't have to transform the chemical energy into heat energy and then use that heat energy to power a generator to produce electrical energy. They can skip the steps in between and directly produce electrical energy from chemical energy. Fuel cells, in general, are not limited to oxidising H_2. There are a number of fuel cells that can use other fuels like Methanol or Methane or even multiple different fuels as an energy source. An overview about different fuel cell technologies can, for example, be found in [19]. For this work, the focus will be put on PEM fuel cells since their understanding is crucial to the understanding of the EHC.

PEM Hydrogen Fuel Cell

Polymer electrolyte membrane fuel cells are basically PEM electrolysers running in reverse. There are, however, some key differences that distinguish the two technologies. First, PEM fuel cells usually use Pt on both the anode and the cathode [6, p. 93] (see equations (2.63) and (2.64) or Figure 2.13b). IrO_2 is therefore usually not needed.

Next, water management becomes a bigger concern in PEM fuel cells compared to PEM electrolysers. The ion conductivity of ionomeric H^+ conducting membranes like Nafion^{TM} is highly dependant on the water content of the membrane [6, p. 81]. For PEM water electrolysis, the humidification of the membrane is usually sufficiently performed through the water that is supplied on the anode side [61]. For PEM fuel cells, the water that is produced on the cathode side is usually not sufficient to protect the membrane from drying out (for an overview of the water transport in PEM see Figure 2.14 in section 2.6). This means that usually both the anode and the cathode gas supply streams are humidified before entering the fuel cell [6, p. 130].

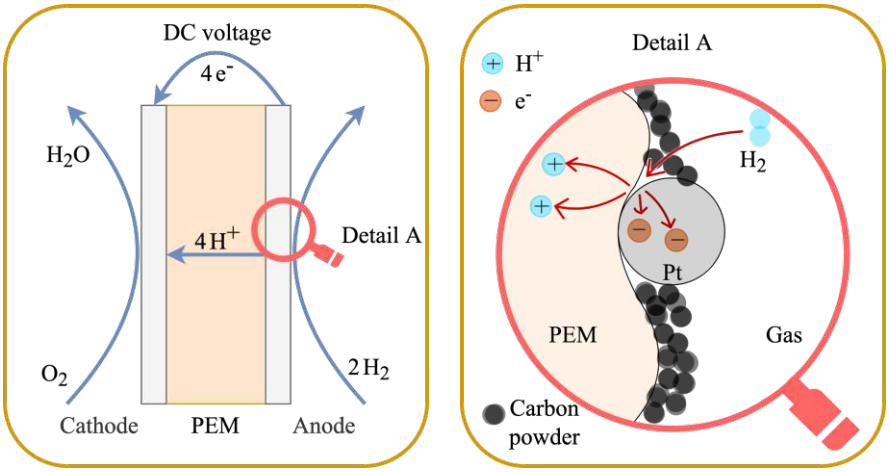

(a) In a PEM fuel cell, the electrolyte conducts H^+ ions. In contrast to PEM electrolysis no external voltage is applied. It is instead produced by the cell

(b) The processes occurring on the PEM fuel cell anode. A three phase boundary (electrolyte, gas, electrode) is necessary for the reaction

Fig. 2.13: Schematic representation of a PEM fuel cell and a detailed view at reaction (2.63) taking place on the anode surface.

As depicted in Figure 2.13b, the reaction in equation (2.63) needs a three phase boundary to take place. The three phases are gas, electrolyte (PEM ionomer) and solid (electrode made from Pt in carbon powder). The gas phase is required to provide H_2 to the reaction. Therefore, flooding of the electrode has to be inhibited because liquid water will prevent the catalyst from accessing the H_2 gas. The solid phase (Pt catalyst in carbon powder support) is required to adsorb the H_2 molecule and subsequently facilitate the splitting into two protons and two

electrons. The electrons travel to the metal current collector back-plate in this solid phase before they continue through the external circuit to the cathode. The ionomer (PEM) is needed at this three phase boundary to transport the produced protons to the cathode. A similar process also occurs on the cathode side (2.64) that won't be discussed in more detail here since it's hardly important for the EHC. One thing to note about the equations (2.63) and (2.64) is that, like in PEM elecrolysis, the reaction involving oxygen (2.64) is slower than reaction (2.63) by multiple orders of magnitude [19, p. 171].

H_2 oxidation (anode)	$2\,H_2 \xrightarrow[Pt]{} 4\,H^+ + 4\,e^-$	$U^0_{ox} = 0{,}00\,V$	(2.63)
O_2 reduction (cathode)	$4\,H^+ + 4\,e^- + O_2 \xrightarrow[Pt]{} 2\,H_2O$	$U^0_{red} = 1{,}23\,V$	(2.64)
Full cell reaction	$2\,H_2 + O_2 \longrightarrow 2\,H_2O$	$U^0_{th} = 1{,}23\,V$	(2.65)

2.6 Hydrogen Pump - Electrochemical Hydrogen Compressor (EHC)

In many ways the electrochemical hydrogen compressor (EHC) is very similar to PEM fuel cells and PEM electrolysers. Both of these were already discussed in the previous sections. Figure 2.14 shows schematics for all three of these technologies to visualise the differences and similarities.

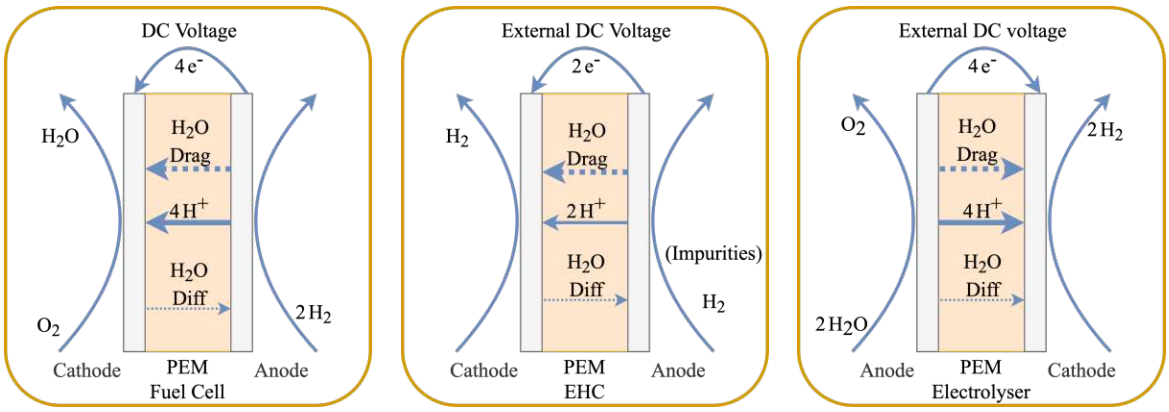

(a) A PEM fuel cell with information on water movement direction and mechanisms from [6, p. 83]

(b) An EHC cell with information on water movement direction and mechanisms from [45].

(c) A PEM electrolysis cell with information on water movement direction and mechanisms from [41, p. 124] and [2].

Fig. 2.14: Overview of a PEM fuel cell, PEM electrolyser and an EHC with arrows depicting the different water transport phenomena in the membrane. H_2O Diffusion (H_2O Diff) is a H_2O concentration driven mechanism, electroosmotic drag (H_2O Drag) is a transport mechanism where the water molecules are transported through the membrane by being attracted to the protons that are transported through the membrane. Electroosmotic drag therefore follows the direction of H_2 movement. Notice that the EHC anode is identical to the PEM fuel cell anode from 2.14a (except for the potential presence of impurities) and that the EHC cathode is identical to the PEM electrolysis cathode from 2.14c

These similarities and the fact that the same reaction is occurring on the anode and the cathode side in two opposite directions lead to some interesting conclusions.

2.6.1 Open Circuit Voltage and Polarisation Curves for EHCs

Trying to find the theoretical open circuit voltage for an EHC we will revisit the HER from PEM electrolysis (2.60) and the H_2 oxidation reaction from PEM fuel cells (2.63).

H_2 reduction (cathode)	$4\,H^+ + 4\,e^- \xrightarrow[Pt]{HER} 2\,H_2$	$U^0_{red} = 0{,}00\,V$
H_2 oxidation (anode)	$2\,H_2 \xrightarrow[Pt]{} 4\,H^+ + 4\,e^-$	$U^0_{ox} = 0{,}00\,V$
Full cell reaction	$H_2 \longrightarrow H_2$	$U^0_e = 0{,}00\,V$

(2.66)

As seen in reaction (2.66) the OCV U^0_e for the EHC is 0 V. Not just because the individual reactions are defined to be 0 V, as they are the reactions occurring in a standard hydrogen electrode, but also because it is the same reaction in different directions and any voltage would cancel out either way. Using this information to simplify the Nernst equation for a full electrochemical cell (2.31), we can get the Nernst equation for an EHC. The minus sign from equation (2.31) is omitted because we are describing the EHC operating as an electrolytic cell and not as a galvanic cell (see section 2.4.4).

$$U_e = \frac{RT}{2F} \ln \frac{p_{H_2 cat}}{p_{H_2 an}} \tag{2.67}$$

The similarity with isothermal compression (equation (2.54)) now becomes even more apparent with these simplifications applied to the Nernst equation. The theoretical cell voltage required for EHC operation turns out to be 0 V when $p_{H_2 cat} = p_{H_2 an}$ and rises with the difference in H_2 partial pressure between anode and cathode side as well as with temperature.

However, as comprehensively discussed in section 2.4.6, raising the cell temperature also has the effect of lowering activation overpotentials, increasing the ionic conductivity of the PEM membrane and therefore lowering ohmic losses and increasing the diffusion coefficient to lower concentration polarisation losses. A higher temperature is therefore generally favourable.

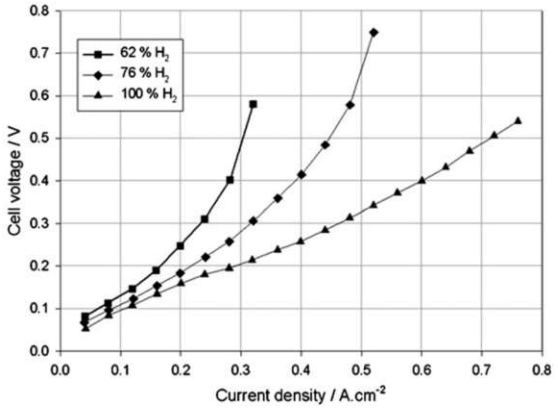

(a) A set of polarisation curves from Grigoriev et al. [45] for different hydrogen concentrations in the feed gas supplied to the EHC anode.

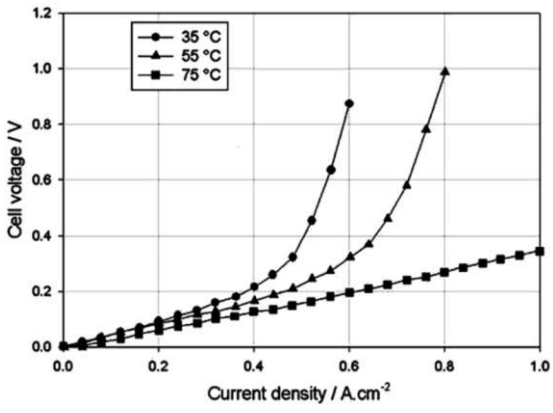

(b) A set of polarisation curves from Grigoriev et al. [45] for different humidifier temperatures

Fig. 2.15: The factors humidity and feed concentration, shown in these exemplary polarisation curves, are among a list of many factors that can influence the EHC polarisation curve. Other factors include back-pressure, temperature, membrane thickness, membrane material, catalyst loading, catalyst type and shape, ... (see section 2.4.6).

As mentioned in 2.4.6.2, the activation overpotental in EHC tends to be a lot lower than the activation overpotential in PEM electrolysis and fuel cells, due to the fast kinetics on both the anode and the cathode side. Figure 2.15 shows some polarisation curves for an EHC. Comparing these polarisation curves to the polarisation curves from Figure 2.7, the less pronounced activation overpotential at low current densities is immediately apparent.

2.6.2 Current and Voltage Efficiency of EHCs

The efficiency of an EHC has two parts to it. The power required for compression is calculated as the product of voltage and current. As discussed in 2.4.6, imperfections increase the voltage required to operate an electrolytic cell (through overpotentials η) and the current passing through the external circuit (i_{ext}) might have to be slightly higher than the current one would assume has to pass through the cell for a certain amount of product i_0 just calculated by using the Faraday equation (2.11). This leads to the two efficiencies commonly used to describe EHCs. The current efficiecy μ_i and the voltage efficieny μ_v.

$$\mu_i = \frac{i_{tot}}{i_{ext}} \qquad \mu_v = \frac{U_e}{U} \qquad \mu_{ehc} = \mu_i \mu_v \tag{2.68}$$

The current i_{tot} can be calculated using the Faraday equation (2.11) with the flux of hydrogen transported by the EHC and the current supplied by the external circuit i_{ext} can be measured directly during an experiment. The voltage ideally required for the operation of the EHC U_e can be calculated using the simplified Nernst equation (2.67) with the inlet temperature and the partial pressures of hydrogen on the anode and cathode side. The actual voltage applied to the EHC U can, again, be determined experimentally. The difference between these two voltages $U - U_e$ contains all the overpotentials η described in section 2.4.6.

2.6.3 Water Management in EHCs

Another differentiating factor between PEM electrolysis, PEM fuel cells and EHCs is water management. Figure 2.14 shows the main directions of water movement in these three processes. In section 2.5.2 the humidification requirements for PEM fuel cells and electrolysis were already discussed. However, the scientific community has not yet entirely made up its mind what the best way to humidify the membrane of an EHC is. The only thing that becomes very apparent when reading literature about the subject is just how critical the issue of water management in EHCs is. Almost no publication fails to mention some sort of issue they ran into regarding water management. Onda et al. [55] humidified the gas entering the anode side and removed condensate on the cathode side if any occurred. Casati et al. [42] decided, after not getting repeatable results using their EHC, to flood or at least partially flood the cathode side compartment. They report this did not lead to the desired improvement but rather to “schizophrenic behaviour” of the EHC. They also report, however, that they continued to operate this way to make sure the membrane was always sufficiently humidified. Ströbel et al. [46] and Sdanghi et al. [43] again just humidified the gas entering the compressor on the anode side. Grigoriev et al. [45] humidified the gas entering the anode chamber and had the entire cathode side of the membrane submerged in water for humidification and temperature control. The Analytic Power Corp [62] used a similar approach with their prototype EHC. They used liquid water on the cathode side for membrane cooling and humidification. Another team working together with the company Hyet Hydrogen [63] again just took the path of humidifying the inlet gas stream using a heated humidifier.

2.6.4 Main Components of an EHC

The Structure of an EHC is practically identical to the structure of a PEM fuel cell except for possibly being designed for a higher operating pressure.

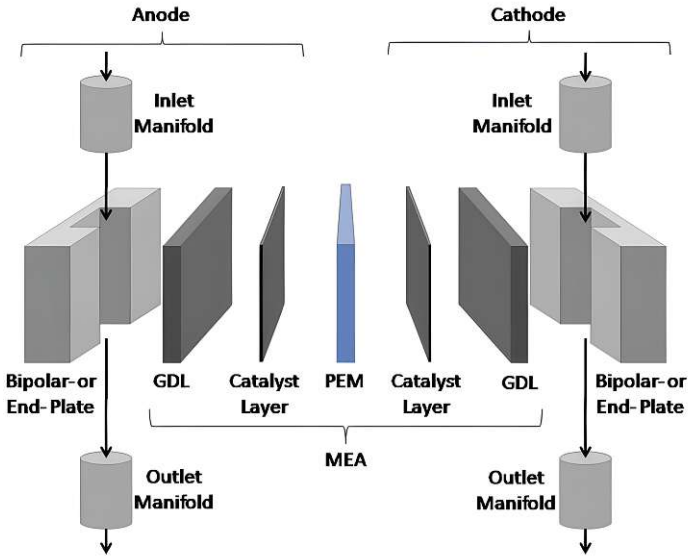

Fig. 2.16: Representation of the cell components of a PEM fuel cell. Image from [3] because the original source is no longer available.

Membrane Electrode Assembly (MEA)

The MEA is an - often prefabricated - assembly of the membrane, the conductive electrodes containing the Pt catalyst and the gas diffusion layers (GDLs). Sometimes the GDLs are not part of the MEA but are combined with the membrane during the stack assembly [6, p. 96]. If the MEA only consists of the membrane and the two catalyst layers, it is sometimes called a three layer MEA or a catalyst coated membrane (CCM). Following the same logic, a MEA that also includes the GDLs is sometimes called a five layer MEA.

Gas Diffusion Layer (GDL)

The GDL is made from a thermally and electrically conductive highly porous material that also has to be corrosion resistant. It is necessary to ensure steady transport of water and reactant gases to and from the membrane, provide a path for heat removal and for electrical current to flow. "These somewhat conflicting requirements are best met by carbon fiber based materials such as carbon fiber papers and woven carbon fabrics or cloths." [6, p. 98]. Sometimes hydrophobic coatings (PTFE) get applied to the GDL to prevent flooding of one side of the membrane that would block reactant gases from accessing the reaction sites.

Anode and Cathode Current Collector Plates or Bipolar Plates

Anode and cathode current collector plates, or bipolar plates for multi cell assemblies, are used as a mechanical support for the MEA but also serve a number of other purposes that again include some conflicting requirements. They connect the cell(s) electrically and therefore need to be conductive, they separate gases in adjacent cells in multi cell setups and distribute the gases over the membrane area by utilising a flow field pattern with possibly complex geometry. They therefore should be impermeable to gases and relatively easy to manufacture. They must be rigid enough to mechanically withstand the design pressure and chemically resist the acidic (pH

2 to 3 and 60 °C–80 °C) [6, p. 106] environment. Especially for EHC applications - due to the very high pressure differences over the membrane - membrane extrusion through small orifices in the collector plate has to be prevented [64].

Graphite fulfils the corrosion resistance requirement but is porous and therefore not completely gas tight as well as hard to machine. Metallic plates fulfil most other requirements but are not corrosion resistant enough. Metals such as aluminium might corrode and metal ions could diffuse into the ionomer lowering its conductivity. Corrosion layers on the metallic surface can also increase the cell resistance. Therefore metallic plates should be covered with a corrosion resistant and electrically conductive protection layer (e.g. graphite, diamond-like carbon, conductive polymer, organic selfassembled polymers, noble metals, metal nitrides, metal carbides, indium doped tin oxide, and so on) [6]. A lot of information and research about the corrosion issue with bipolar plates in EHCs can be found in this Analytic Power Corp Report [62].

2.6.5 Operational Modes for EHCs

EHCs can generally be operated in three different ways.

- Separation: A mixture of hydrogen and other gasses is supplied to the anode side. The EHC selectively transports protons from the anode through the membrane to the cathode which is kept at more or less the same pressure as the anode. The EHC process in literature about this is sometimes called electrochemical hydrogen separation (EHS) [65] or electrochemical hydrogen purification (EHP) [66]. This operational mode was investigated in [42, 45, 55, 66, 67].

- Compression: Pure H_2 is supplied to the anode side and transported through the membrane against a pressure gradient to the cathode side. The cathode side is confined and therefore increases in pressure as more and more H_2 gets pumped through the membrane. The EHC process in literature about this is sometimes called electrochemical compression (ECC) [47] This operational mode was investigated in [43, 45, 46, 47, 55, 68, 69]

- Simultaneous Separation and Compression: Both of the previously mentioned operational modes have a difference in H_2 partial pressure between anode and cathode in common which then leads to an increase in the necessary U_e for EHC operation. It would seem only natural to perform both actions at the same time. However, this has so far not been studied in detail. Combined compression and purification was performed in [63, 66, 70]

Chapter 3

Realisation of the EHC

3.1 Design Considerations

Fig. 3.1: Picture of the laboratory setup showing the thermostatic bath with the humidifier behind the compressor on the table (middle), the gas drying unit (bottom right), the temperature control & sensor electronics (middle right), the compressor power supply (middle right) and the power supply for the gas drying unit (top right)

After performing a thorough literature review and starting to create first stack designs, it became apparent that some design parameters had to be determined before continuing with further detailed planning. Since membrane electrode assemblys (MEAs) in "small household quantities" are only available in specific dimensions (usually $1'' \approx 2{,}5\,\text{cm} \times 2{,}5\,\text{cm}$, $2'' \approx 5\,\text{cm} \times 5\,\text{cm}$ or $3'' \approx 7\,\text{cm} \times 7\,\text{cm}$), the first design parameter that was decided on, was the membrane area of $50\,\text{cm}^2$. The other parameters that were set before going into further detailed planning were the maximum design pressure of 10 bar and the operating temperature range of 20 °C–95 °C for the cell stack. The maximum pressure was chosen at 10 bar, because fittings, tubing and other connectors for this pressure are readily available and comparatively inexpensive. The temperature limitation stems from the fact that a PEM needs liquid water to transport protons through the membrane and is thus limited to temperatures below 100 °C under normal operating conditions. These parameters lead to further restrictions and design choices. Original plans of incorporating water circulated heat exchanger loops into the compressor and humidifier unit where changed to a simpler design of submerging the entire compressor and humidifier in a thermostatic bath (similar to [46]) because of concerns for water condensing in the stainless steal pipes between the two heated units or possible uneven heating/cooling. Figure 3.1 and the flowchart in Figure 3.2 on the following page give an overview of the entire system. The structural frame was built using extruded aluminium profiles with dimensions $3\,\text{cm} \times 3\,\text{cm}$. All working surfaces close to the thermostatic bath are made from clear polycarbonate due to its mechanical stability and temperature resistance. The bottom storage shelf is made from grey polyvinyl chloride. The following sections will give a more detailed description of the individual main components that had to be designed and built for this setup.

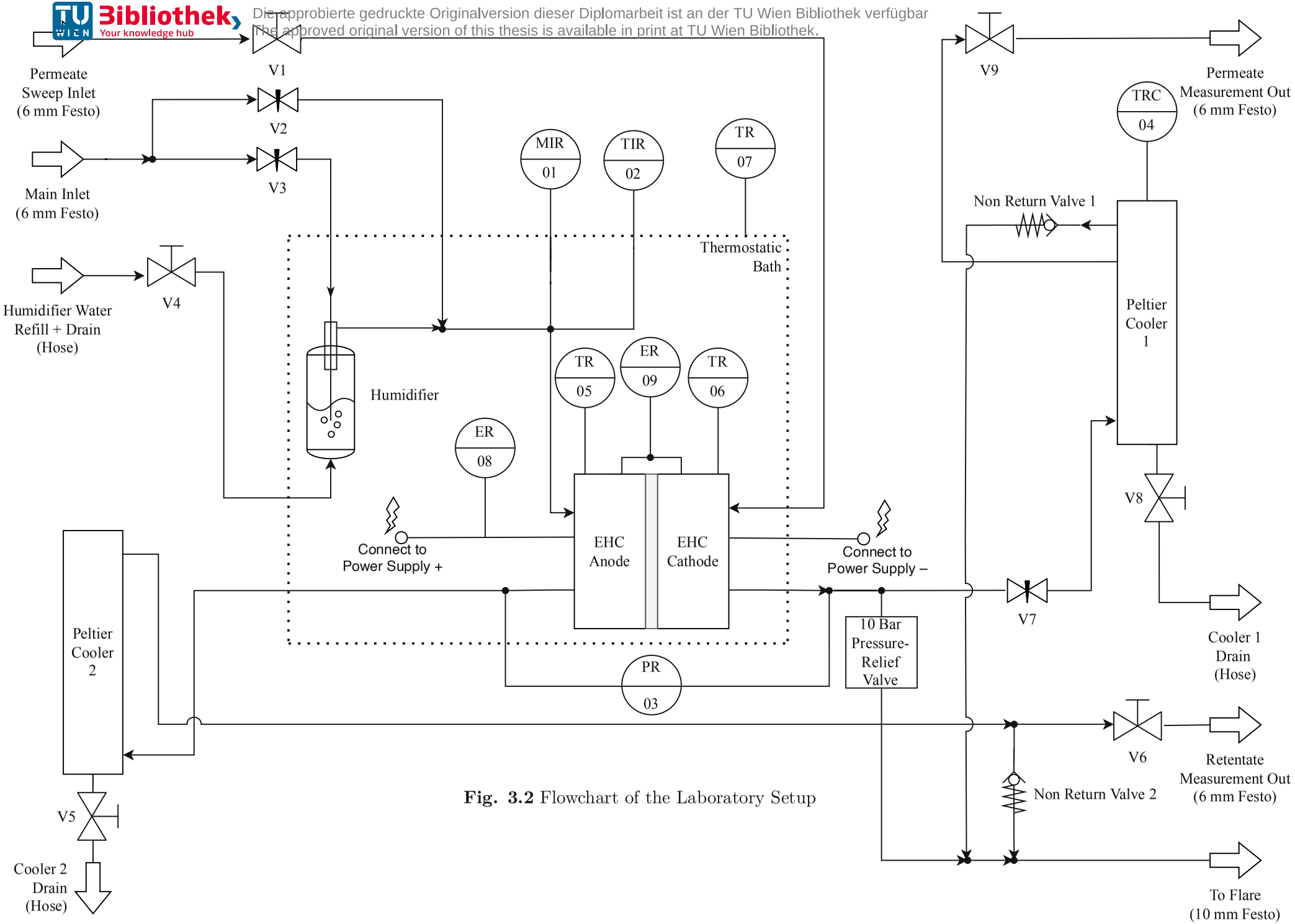

Fig. 3.2 Flowchart of the Laboratory Setup

3.2 The Compressor

The compressor is the core part of the entire system. The individual components that make up the compressor were already listed under (2.6.4) with a brief description of their respective functions. When designing the compressor, a number of factors were taken into consideration as listed below. Figure 3.3 shows the CAD model of the stack compared to the real assembled stack with all the Sensors and electrical connections attached. Figure 3.4 gives a schematic overview of all the components that the actual stack is comprised of.

(a) CAD Model of the final stack Design

(b) The fully assembled stack with all of the sensors and power cables connected

Fig. 3.3: Comparison of the Final CAD models with the real stack after assembly

- Mechanical requirements
  - Firmly and evenly press the MEA against the anodic and cathodic current collector plates to reduce contact resistance (see 2.4.6.3)
  - Withstand the design pressure
  - Facilitate H_2 transport to the membrane through the GDLs with the help of gas distribution channels
- Thermal requirements
  - Remove excess heat generated during operation (see 2.4.7)
  - Enable experiments with the compressor at any desired temperature
- Corrosion resistance
- Sealing design to prevent or at least easily detect hydrogen leaks
- Electrical requirements
  - Prevent short circuit between cathode and anode side
  - Connect high current power cables for up to 60 A to the cathode and anode sides respectively
- Include sensors for compressor performance surveillance

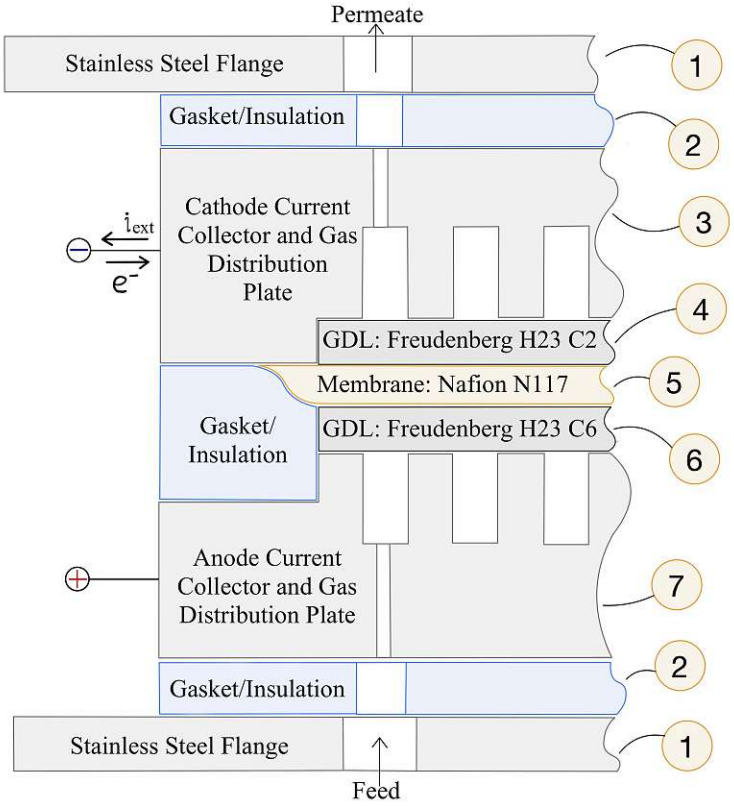

Fig. 3.4: Schematic cross-sectional view of the compressor stack. Explanations to each component (number) can be found below.

① Stainless Steel (V2A) Flange (DN 100 - PN 10-16 - DIN EN 1092-1-Typ 05) from Edelstahl24 (Frankfurt, Germany) with two G 1/4″ holes drilled in each of them for the inlet and outlet connections on anode and cathode side respectively.

② "Ice Cube Sealing" made from a Polyolefin Elastometer and sold by Quintech (Göppingen, Germany) for use with PEM fuel cells. Uncompressed thickness is 800 µm, compressed thickness (10 bar) is 600 µm. The material was cut to shape using stamps and knives. It is used to create a seal against hydrogen leaks and prevent electrical contact between the two current collector plates or the current collector plate and the respective stainless steel flange.

③ Cathode current collector plate made from aluminium (AlMg4,5Mn from Fixmetall GmbH) with a single CNC machined serpentine flow channel of width 1 mm and a CNC machined pocket with a depth of 200 µm designed for the GDL to fit into.

④ H23 C2 GDL for the cathode side made by Freudenberg (Weinheim, Germany) and sold by Quintech. Uncompressed thickness is 255 µm, compressed thickness (10 bar) is 215 µm. This GDL is not isotropic since it has a microporous layer on one side (can easily be visually identified by smoother texture). This layer should face the membrane. Since flooding is not an issue on the cathode side, H23 C2 is not treated with a hydrophobic coating.

⑤ Nafion N117 CCM with a Pt loading of 0,3 mg/cm^2 on the anode and cathode side of the CCM, respectively. Active area is 7 cm × 7 cm and membrane thickness is 183 µm.

⑥ H23 C6 GDL for the anode side made by Freudenberg and sold by Quintech. Uncompressed thickness is 250 µm, compressed thickness (10 bar) is 210 µm. This GDL is not isotropic since it has a microporous layer on one side. This layer should face the membrane. Since flooding can be an issue on the anode side, H23 C6 is treated with a hydrophobic coating.

⑦ Anode current collector plate made from aluminium (AlMg4,5Mn) with a single CNC machined serpentine flow channel of width 1 mm. The middle section of the collector plate is raised by 200 µm so that the total spacing between the two collector plates is equal to the sum of the thicknesses of the individual components that are supposed to fit in between them. This design comes with its weaknesses as discussed later.

Since all of the components in Figure 3.4 have to be vertically aligned with high precision during assembly, some alignment aids were also incorporated that are not shown in Figures 3.4 and 3.3. The two current collector plates were outfitted with Teflon alignment pins in their corners to assure alignment between ⑦ and ③. Additionally, to allow for proper alignment of the 1/4″ holes in ① and the smaller holes in the respective current collector plate, a poly-carbonate template was fabricated. This template is attached to the stainless steel flange ① using the M16 bolts as references before adding the first current collector plate into the poly-carbonate cutout during assembly. The M16 bolts (shown in Figure 3.3b) used to connect the two stainless steel flanges to each other are electrically insulated from the flanges by using a thin film of polyethylene terephthalate rolled into a cylinder and held together by Kapton tape. This was done to add a second layer of protection against a short circuit between the two current collector plates (⑦ and ③) in addition to the Gaskets (②). The M16 bolt heads and the M16 nuts are insulated from the flanges by using M16 Polyamid washers. These slightly deformable polymer washers also help providing a more even clamping pressure. Every material used in the compressor had to be able to withstand temperatures of up to the design temperature of 95 °C. Before assembling the stack, the membrane was soaked in deionised water overnight to fully saturate it with water at the start of the first experiments.

Other combinations of gas diffusion layers and membranes than the ones shown in Figure 3.4 are also possible (e.g. anode: titanium mesh and Sigracet 28 BC; membrane: Nafion 117; cathode: Sigracet 29 AA or anode: Titanium Mesh and Sigracet 28 BC; membrane: Nafion 212; Cathode: Sigracet 29 AA). One limitation to possible combinations is the total thickness of the MEA, that has to be around 600 µm for this stack design to seal and still put the MEA under adequate compression to make good electrical contact. The uncompressed thickness of the MEA as shown (④, ⑤ and ⑥) is 688 µm. The other two options proposed above would turn out to around 778 µm and 646 µm, respectively. Materials for some alternative MEAs were procured but not used for experiments due to time constraints. All the results shown in this work were obtained with the setup as shown in Figure 3.4. The CCMs procured from Ionpower GmbH (using N117 and NR212) both have a Pt loading of 0,3 mg/cm^2 on both the anode and the cathode side. The CCM using this N117 was used for the first test setup. One of the alternative CCMs (using N212), procured from Quintech, has an asymmetrical Pt loading of 0,3 mg/cm^2 on the anode side and 0,6 mg/cm^2 on the cathode side. This seems to be common practice for CCMs manufactured for fuel cell use [71] and is possibly to combat the slower Kinetics of the reaction occurring on the cathode side of a fuel cell (oxygen side). Because of the thick stainless steel plates and rigid power cables, the assembled stack is not easily manageable. Therefore a electrical winch was incorporated in the laboratory setup to make lifting the compressor in and out of the thermostatic bath more convenient. The winch can be seen in Figure 3.1 (blue object in the top).

3.3 Temperature Control for Humidifier and Compressor

As shown in the flowchart (Figure 3.2), the compressor and gas humidifier unit are both submerged in a thermostatic bath. The pipes connecting the two are also submerged in the bath and the combined humidity and temperature measurement before entering the compressor is performed in the submerged and therefore heated pipe to impede condensation and assure an accurate humidity reading. The humidifier itself was made using a stainless steel pneumatic tank (Festo "CRVZS-0.75") in which a 6 mm OD stainless steel pipe is partially submerged in water. The water inside the humidifier can be refilled or drained using the valve V5 (flowchart in Figure 3.2). After bubbling through the water, the humidified gas exits the humidifier through the same stainless steel T-piece it entered by. This time, however, it passes the outside of the before-mentioned stainless steel pipe and therefore exits through the other opening of the T-piece. The Polycarbonate bath was custom made by Acrylstudio (Wiener Neudorf, Austria) with outer dimensions of $(L \times W \times H)$ 66 cm × 25 cm × 35 cm and a wall thickness of 1 cm. The roughly 50 L volume of this bath is filled with deionised water and mixed with about 5 g of sodium carbonate (Na_2CO_3) to adjust the pH and prevent corrosion of the stainless steel parts submerged in it. The amount of Na_2CO_3 is adapted from the concentration recommended by IKA (Staufen, Germany) for the operation of their heating immersion circulators [72]. Overdosing of Na_2CO_3 should be avoided because more ions lead to an increased conductivity of the thermostatic bath. The concentration stated here did not lead to significant stray currents through the thermostatic bath during experiments, and current efficiencies of close to 100 % were regularly achieved (as shown in results section 4.2.6). The heating immersion circulator used to control the bath temperature is the "Corio CD" manufactured by Julabo (Seelbach, Germany). Its heating capacity is 2 kW and the advertised temperature stability is ±0,03 °C.

3.4 Gas Cooling and Drying Unit

Using the membrane area chosen at the beginning of the design process (section 3.1), some typical current densities from various literature sources about EHCs and the Faraday equation (2.11), a range of possible hydrogen fluxes were calculated. A maximum flux of 3,5 $cm^3/(min\,cm^2)$ with a membrane area of 50 cm^2 lead to a maximum flow of 175 cm^3/min through the membrane. Assuming this hydrogen flux will have a relative humidity of 90 % at 85 °C, it is possible to estimate the required power of the gas cooling unit. Both the latent heat of the water phase change and the sensible heat of cooling the liquid water and the hydrogen gas to a chosen temperature of 5 °C were calculated. Like this, a minimal continuous power of 6,5 W was found to be necessary for the cooler. Since this power is well within the range of what is achievable with thermoelectric cooling, it was decided to design the gas cooler using Peltier elements. Peltier coolers operate silently (unlike compressor coolers) and, except for electrical power, don't require any further connections to external support systems (unlike external water cooling systems). Two design principles were followed when designing the thermoelectric cooler:

1. Operate Peltier elements as far below their rated maximum power as technically and economically feasible
2. Minimise ΔT over the Peltier elements as far as technically possible by keeping the hot side temperature of the peltier element as close to room temperature as possible.

Both of these principles can easily be explained by examining the characteristic curves of Peltier elements like the one used for this gas cooler (Tru Components TES1-127040; 15,4 V DC; 3,9 A; sold by Conrad (Wels, Austria) under the item number 1565767). In this Peltier elements

data sheet we can see that an increase in current from 0,8 A to 1,6 A with $\Delta T = 20\,°C$ will increase the heat "pumped" by the Peltier element by about 10 W. However, increasing the current from 3,2 A to 4,0 A with the same ΔT only increases the amount of heat pumped by about 2,5 W. The efficiency decreases with increasing current. Similarly, the heat pumped by a Peltier element at a given current can be maximised, when ΔT is minimised. Looking at the data sheet again, we can see that, when operating at 1,8 A with $\Delta T = 20\,°C$, the Peltier element will pump about 12 W. Increasing ΔT to 40 °C at the same current, the heat pumped drops to 3 W. Since the goal is to get the cold side of the Peltier element as cold as possible while still maintaining sufficient cooling power, we need to keep the hot side as close to room temperature as possible to minimise ΔT and therefore maximise the heat pumped by each element. Originally it was planned to only cool and dry the permeate using this cooler. During first experiments it became obvious that drying the retentate would also be necessary. Luckily the gas cooling unit was designed with sufficient safety margins (60 W heat pumping capacity at $\Delta T = 30\,°C$ with an efficiency of 54 %) so it was possible to retrofit a second cooling chamber to the gas cooler that could dry the retentate gas stream. All the components and the mechanical construction of the cooler will be discussed in the following section.

3.4.1 Mechanical construction

The core of the gas cooling/drying unit consists of two pneumatic manifolds made from aluminium through which, during operation, the humid gas will flow. To condense the water out of this gas stream, the aluminium manifold is cooled to a specific temperature by 6 Peltier elements operated by a closed loop controller (see section 3.4.2).

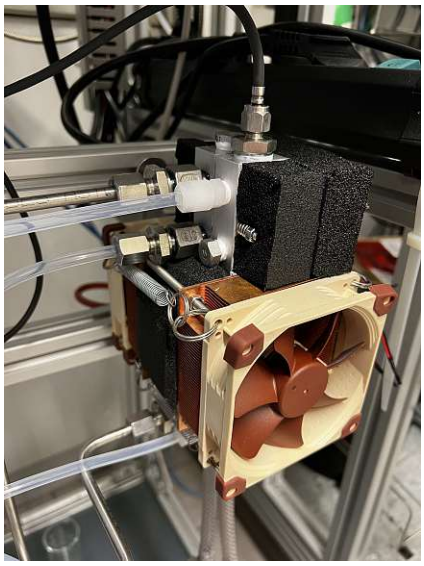

(a) Peltier gas cooler as installed with insulation, temperature sensor for the PID controller and all the necessary gas inlets and outlets connected

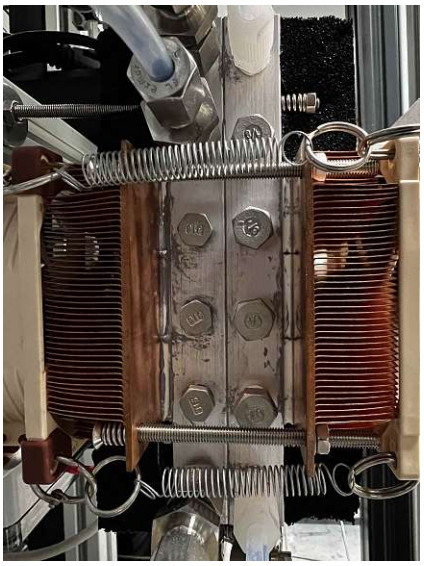

(b) Peltier gas cooler with insulation partially removed to show individual components in the stack.

Fig. 3.5: The main components of the gas cooling/drying unit from outside to inside are: 2x Noctua NF-A9 FLX 92 mm CPU fan; 2x modified 125 W Dynatron - K129 1U CPU Cooler (cooler and fan from Haym.Infotec (Salzburg, Austria)); 6x Tru Components TES1-127040 3,9 A Peltier element, 2x Legris 3311 10 13 06 pneumatic manifold (6x 1/8″ outlet, 2x 1/4″ inlet each)

The hot side of these 6 Peltier elements is in thermal contact with two modified copper server CPU coolers. The copper coolers had to be modified using a CNC mill and sandpaper on a smooth reference surface to accommodate 3 Peltier elements each. The thermal contact between the aluminium manifolds, the Peltier elements and the copper heat sinks was enhanced by use of thermal paste. This portion of the cooling stack (heat sinks, Peltier elements and aluminium manifolds) is pressed together by 4 spring-loaded M5 screws.

The 6 Peltier elements will produce a heat flux of about 112 W when operated at the maximum power allowed by the controller. Since the hot side temperature of the Peltiers should stay as close to room temperature as possible (see section 3.4), two CPU fans were attached to the outside of the cooling stack with 4 springs that pull them towards each other. With these fans in operation, the copper heat sinks do not get significantly warmer than the surrounding air even under maximum load.

3.4.2 PID controller

This unit will cool the incoming humid gas streams to a specific dew point that can be set in software by issuing a command to the controller running on an Arduino due single-board microcontroller via USB (for syntax see section 3.5.6). A fast responding Pt100 resistance temperature detector (RTD) probe constantly measures the temperature of a gas stream exiting the retentate cooling chamber. The Arduino uses this temperature, the target temperature and the experimentally determined constants $kp = 1000$ and $ti = 400$ (found in results section 4.1.1) to calculate P and I values (see Arduino Code in Attachment 6.2). The code for the differential (D) part of the PID controller was implemented but first experiments showed that a pure PI controller was sufficient to reach temperature stability of around ±0,2 °C. The constant kd to calculate D is therefore set to 0.

After summing up the just found P and I values, they are used to send an analogue signal from the Arduino's digital to analogue converter (0,55 V–2,75 V) to a remote controlled lab bench power supply by Voltcraft (PPS 11603 , 1 V–60 V, 0 A–2,5 A). This power supply accepts analogue inputs in the range from 0 V to 5 V for both the current limit and the set output voltage. The input controlling the power supply's current limit is constantly connected to the 5 V pin on the Arduino to keep the current limit at 2,5 A. The power supply's control input controlling the output voltage is connected to the Arduino's digital to analogue converter. The voltage produced by the Power supply can therefore be set to any value between 6,6 V and 33 V. This voltage is then directly applied to the 6 Peltier elements wired in series. The circuit diagram 3.8 provides this information in a graphical way.

3.5 Sensors and Electronics

A variety of sensors is installed in this setup. All of the sensor locations and what they are measuring is shown in the flowchart in Figure 3.2. The exact wiring for each sensor can be looked up in the circuit diagram 3.8.

3.5.1 Pressure and Product Purity

The obvious parameters of interest for a device used for purification and compression of hydrogen are the (differential) pressure over the compressor unit and some kind of purity measurement for the output gas stream. As shown in the flowchart in Figure 3.2, the pressure measurement is implemented directly in parallel to the compressor. The sensor used for this measurement is manufactured and sold by Analog Microelectronics (Mainz, Germany) under the product

ID "AMS 3012-10000-D", has a differential pressure range of 0 mbar to 10 000 mbar and outputs a standard 4 mA–20 mA signal. This current signal is then read by using precision surface mount component (SMC) shunt resistors on a custom-made printed circuit board (PCB) attached to the Arduino Due. The Arduino Due has a 12 bit analogue to digital converter (ADC) to digitalise the signal. The purity measurement for the product gas was not directly implemented inside this setup but it was assumed to be available in the gas supply unit. By opening or closing valves V6 or V9, a sample gas stream from both the post gas cooler permeate or the retentate after its gas cooler can be gathered. The non return valves 1 and 2 ensure that, if valves V6 or V9 are closed, the gas will be safely discharged to the combined outlet connected to a flare for normal operation. They also ensure that no contamination from the other side of the compressor (permeate/retentate) can occur while using one of the measurement outlets. The flare connected to the combined outlet, using a CH_4 burning pilot light, will ensure that no explosive gas mixtures can build up in the experimental area.

3.5.2 Temperature

In addition to pressure and purity measurements temperature is an important process parameter. The compressor produces heat during operation that has to be removed in the thermostatic bath and the gas cooler has to cool down the incoming humid gas stream. All of these processes need to be monitored. The temperature sensors (2, 5, 6 and 7 in the flowchart in Figure 3.2) are all of the type Pt100 and were bought together with their respective signal transducers from Otom Group (Bräunlingen, Germany) at sensorshop24.de. These transducers produce a standard 4 mA–20 mA current signal that can again be read using the Arduino's ADC and some precision SMC resistors.

3.5.3 Operational Current

To determine the current efficiency μ_i of the EHC as introduced in equation (2.68), the current through the external circuitry i_{ext} has to be measured. The membrane area of 50 cm^2 (as chosen in section 3.1) and typical current densities from literature tell us that very high currents of 100 A or potentially even more could be reached. The power supply used in this setup limits the current range to 0 A–60 A but this may still be a very significant amount of current. Measuring this current using a shunt resistor attached to the Arduino's ADC to create a voltage drop of 0 V–3,3 V, would result in as much as 198 W of power lost to heat. This is obviously not feasible and therefore a different principle of current measurement had to be deployed. A current transformer using a primary and a secondary winding to create a small output current proportional to the current flowing through the main circuit would provide a great low impedance measurement principle. However, this principle only works for AC currents since it depends on changing magnetic fields. The EHC works with DC. Therefore the sensor chosen to measure i_{ext} in this setup is the LEM "LA-150P" current transducer. It uses the Hall effect in a closed loop configuration and is therefore able to pick up DC currents with high accuracy and minimise the influence of non ideal effects such as linearity and gain errors [73]. This sensor has a current output equal to $i_s = i_{ext}/2000$. The required supply voltage of ±12 V is supplied by a DC to DC converter (see circuit diagram in Figure 3.8). With this supply voltage, the maximum allowed value for the shunt resistor to measure i_s is 40 Ω. As shown in the circuit diagram, a 22 Ω precision SMC resistor is used for this purpose. The voltage drop this shunt resistor will produce in the expected range of i_{ext} is very small, this voltage is not directly determined using the Arduino's on board ADC. Instead, an external 16 bit ADC with a programmable gain

amplifier (ADS1115) is used for this purpose. This ADC then digitally transmits the measured voltage to the ARDUINO by using the I2C protocol.

3.5.4 Applied Stack Voltage

To determine the voltage efficiency μ_v of the EHC as introduced in equation (2.68), the voltage applied to the stack has to be measured. Voltages could directly be measured by the ARDUINO's internal ADC and it should therefore be an easy task to perform this voltage measurement. Nevertheless a few important points had to be considered. Because of the high possible currents, even the copper wire with a cross section of 50 mm^2, used to connect the compressor to its power supply, could cause a measurable voltage drop. The voltage measurement is therefore performed by using a second set of wires directly attached to the Anode and Cathode current collector plates. The expected voltages to be measured are in the range of 0 V–1 V. By using the ARDUINO's on board ADC with a range of 0 V–3,3 V, we would waste two thirds of our dynamic range. Therefore, another external 16 bit ADC with a programmable gain amplifier (ADS1115) is used to measure this voltage. Under normal operation, the voltage applied to a single layer EHC stack should not be much higher than 1 V. However, the power supply used to apply this voltage to the compressor (ELV "PS900W") can theoretically deliver up to 60 V. This voltage would most certainly destroy the ARDUINO and possibly other components. Therefore some way to limit the voltage seen by the ADC had to be found that does not change the measured voltage. This goal was achieved by adding two diodes (wired in series) parallel to the compressor and the ADC and one very fast acting (FF) fuse to the positive lead of the voltage measurement line (see bottom right of the circuit diagram in Figure 3.8). Should an over voltage event occur, the diodes start conducting large amounts of current in an avalanche breakdown event, therefore limiting the voltage seen by the ADC. This large current through the voltage sensing wire would break the fuse and cut the connection from the compressor to the ADC. By using two diodes with a breakdown voltage of 0,7 V wired in series, the voltage limit was set to about 1,4 V. At the low voltages in the range expected, these diodes barely conduct any current and therefore don't influence the measured voltage significantly. Results of the experiments with this over voltage protection circuit can be found in the results chapter under section 4.1.3. Importantly, this setup does not protect against over voltage events if the polarity is reversed. Therefore extra care has to be taken to assure the voltage sensing wires are connected to the compressor with the correct polarity.

3.5.5 Electrical Distribution Cabinet and Custom PCB

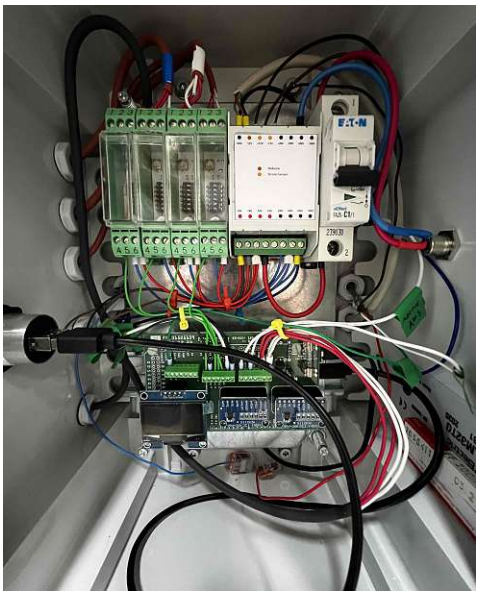

Fig. 3.6: View inside the electrical distribution cabinet

The electrical distribution cabinet contains the power supply and wiring of most of the low voltage devices. This includes the sensors, the CPU fans of the gas cooler, and the ARDUINO DUE reading the sensor values and producing the PI(D) signal for the remote control of the gas cooler power supply. It is located above the gas cooler and below the power supply for the compressor (see Figure 3.1). The cabinet (close up picture in Figure 3.6) is supplied with 24 V DC through a MEANWELL "GST60A". This power supply is protected against short circuit, overload, over voltage and over temperature. The voltage is passed into the cabinet by a coaxial power connector and then distributed as shown in the circuit diagram in Figure 3.8. The DIN rail mounted circuit board next to the switch in the top right of Figure 3.6 contains all the components to produce 12 V DC for the ARDUINO DUE and the NOCTUA CPU fans, ±12 V DC for the current sensor and to distribute the 24 V from the input to all other devices as shown in the circuit diagram. The evaluation of 9 different sensors using the ARDUINO DUE, as shown in the circuit diagram in Figure 3.8, requires a number of passive and active electronic components. These components are all attached to a "shield", a circuit board attached to the ARDUINO using its header pins. A first prototype of this shield relying entirely on through hole components was fabricated and tested successfully. To maximise the space available in the electrical distribution cabinet, incorporate a small display and minimise the possibility of connections becoming loose over time due to faulty solder joints, the final design relied on using a PCB and a mixture of surface mount and through hole components instead of just through hole components.

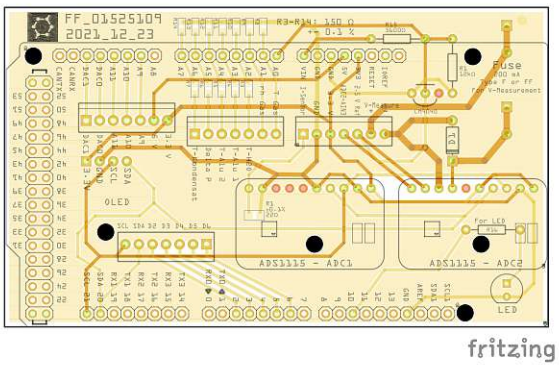

(a) The PCB as designed by using the open source CAD software FRITZING.

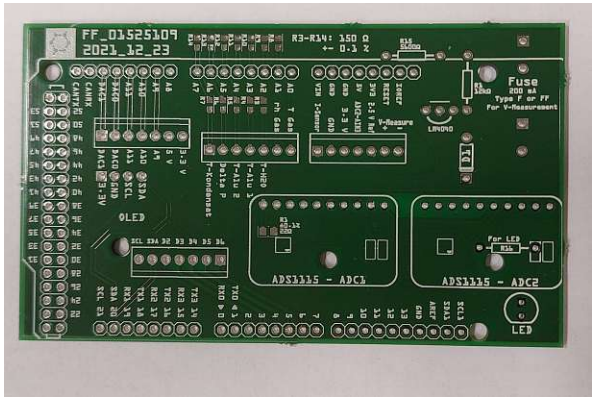

(b) The real PCB as fabricated by the company AISLER (Aachen, Germany)

Fig. 3.7: The PCB incorporates mounts for two external ADCs, one OLED display, a 2,5 V reference voltage source, a fuse to protect the circuit against over voltage from the compressor power supply, screw terminals to connect the ARDUINO to all the other components and header pins to connect this shield to the ARDUINO itself.

3.5.6 Syntax for Communication with the Arduino Due

The ARDUINO DUE sends the measurement results to a host computer via USB (baud rate = 38400) and can be remote controlled by issuing serial commands to it. Possible commands are listed in Table 3.1.

Tab. 3.1: Possible Commands the ARDUINO will except with the code as shown in Appendix section 6.2

Command	Explanation
T XX.X	Changes the set-point of the gas cooler temperature to XX.X °C. XX.X has to be a float in the range from "-5.0" to "25". The standard value after restarting the ARDUINO is 10 °C. Both T XX.X and TXX.X (with and without white space) are allowed syntax.
f XXXX	Changes the frequency of serial communication with the host computer. After issuing this command the ARDUINO will try to report values once every XXXX ms (milliseconds). XXXX has to be an integer larger than zero. Arbitrarily high frequencies can be set this way but the ARDUINO will internally confirm that values are only reported at most with the measurement frequency (I.e. the same value saved in the ARDUINO's buffer will not be reported twice if the reporting frequency is set higher than the measurement frequency). Both f XXXX and fXXXX (with and without white space) are allowed syntax.
m	Toggle between machine and human readable output format. The machine readable output format is of the shape ";value;value;...;value;" (semicolon separated) and does not show headers. The human readable output format uses tabulator symbols to separate the values and repeats the header row every 10 cycles (can be changed in code by changing the constant byte "repeat_channelNames_every"). The order of the values is the same in both modes.
h	Displays the help message.
Any other	Displays the message "unknown command, press h to Display help"

Fig. 3.8 Circuit Diagram of the Laboratory Setup

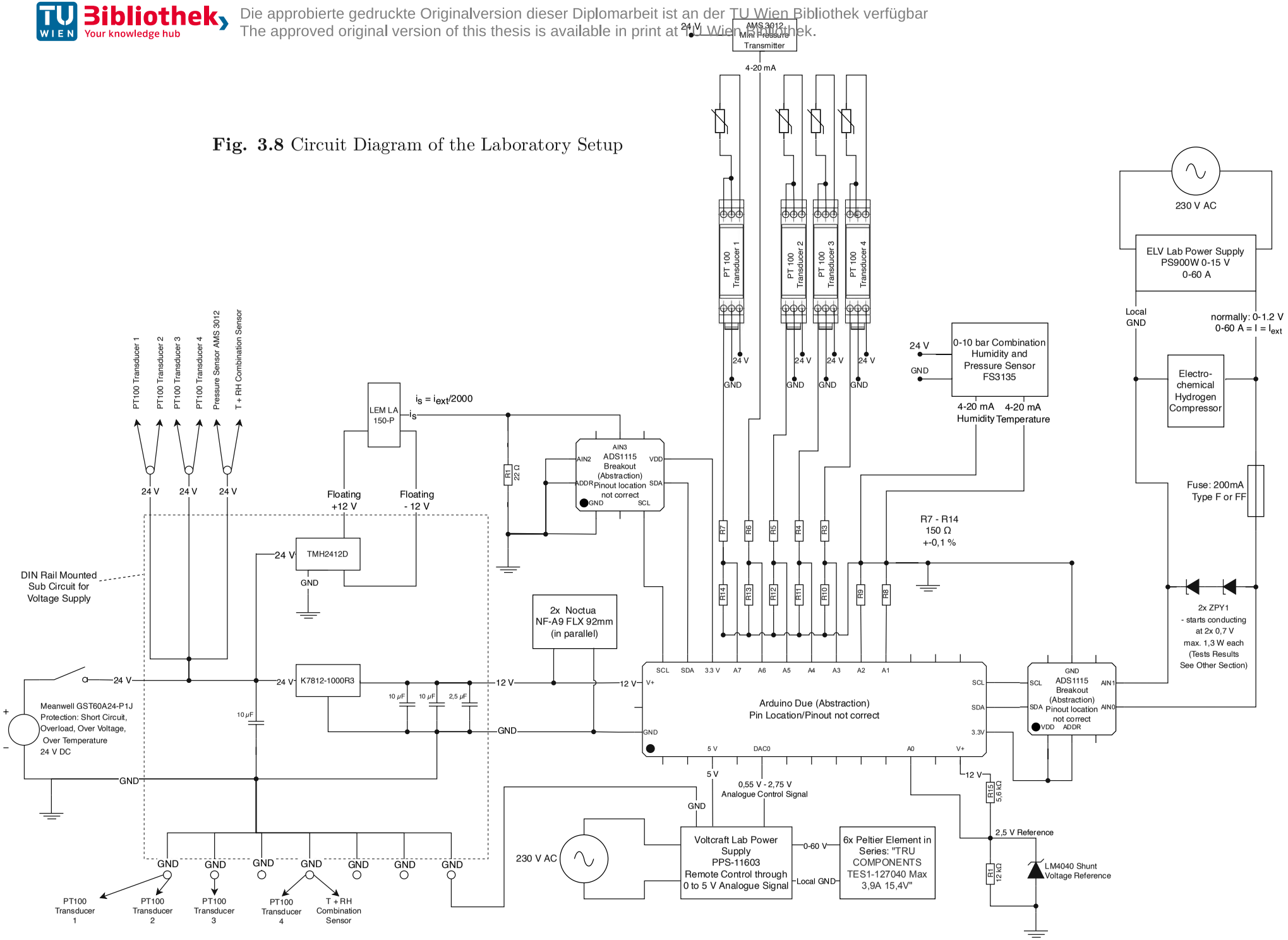

Chapter 4

First Experiments and Results

4.1 Preliminary Experiments

4.1.1 Determining the PI Gas Cooler Constants

Since, as mentioned in section 3.4.2, the PI controlled gas cooler had to be retrofitted to accommodate a second cooling chamber for the retentate, two sets of experiments were conducted to determine the constants for the control of the gas cooler, one prior to the retrofit and one thereafter. A method similar to the Ziegler–Nichols tuning method was used to determine the constants. A selection of results from these experiments is shown in Figures 4.1a and 4.1b.

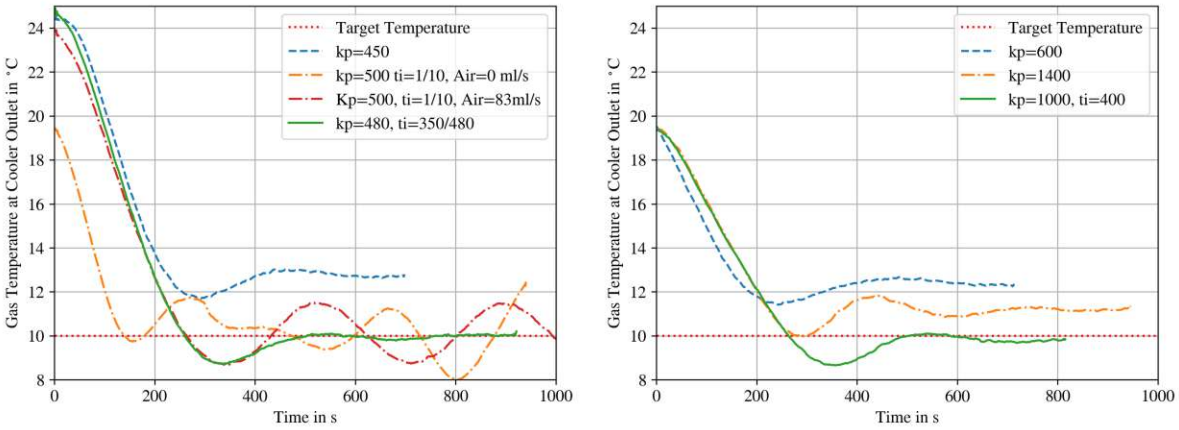

(a) Selected temperature/time curves for the gas cooler with one chamber.

(b) Selected temperature/time curves for the gas cooler after retrofitting it with a second cooling chamber.

Fig. 4.1: A selection of the experiments performed to find the constants kp and ti.

The blue dashed curves in Figure 4.1 show results of experiments using only proportional gain kp. This gain was then increased and eventually complemented by an integral gain $1/ti$. The green solid curves are produced using the final values determined for the system in its respective configuration. As shown here, the proportional gain had to be doubled after changing the setup to reach similar behaviour.

4.1.2 Gas Cooler Step Response and Response to Disturbance

To test the gas cooler's response to sudden changes in operational parameters like gas flow rate or sudden jumps in the target temperature during operation, another experiment was conducted. Results are shown in Figure 4.2.

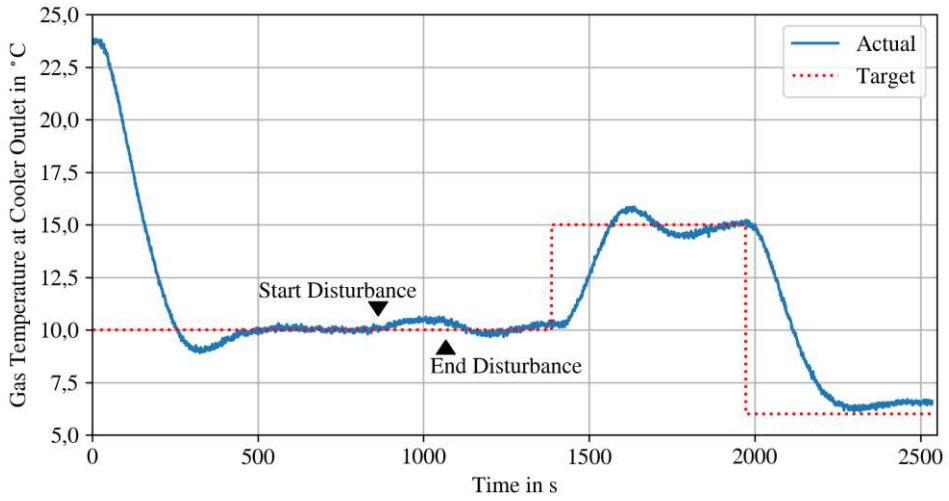

Fig. 4.2: Temperature of the gas leaving the cooler over time. The markers show where a disturbance (sudden change of gas flow rate from 27 mL/min to 133 mL/min) was introduced and where this disturbance was stopped again (lowering flow rate to 20 mL/min). Two changes in target temperature (from 10 °C to 15 °C and from 15 °C to 6 °C) were sent to the controller. The step response to these changes is also shown here.

4.1.3 Over-Voltage Protection for Voltage Measurements

A number of different diodes were investigated as possible candidates for the over-voltage protection circuit that was introduced in section 3.5.4. The circuits using them (A,B,C,D and E) are displayed in Figure 4.3c. Original plans to use (A) or (B) to limit the output voltage to 3,3 V were unsuccessful as seen in 4.3b. However, since the ADC "ADS1115" measuring the voltage across the diodes can be set to a gain of 2x, capping the output voltage at around 1,6 V was a good option. This was fulfilled by two "ZPY1" in series (C). The main factor distinguishing the diodes "ZPD3.3", "TC-ZPD2.7" and "ZPY1" is the Zener breakdown voltage of 3,3 V, 2,7 V and 0,7 V, respectively. The first two diodes are Zener diodes, and the "ZPY1" is a Si diode which has to be operated forward biased to mimic the behaviour of a Zener diode. The reverse breakdown voltage for this diode is higher than any voltage tested in the tests performed (see Series C in Figure 4.3 or data sheet of "ZPY1"). This demonstrates again that the fuse would not trip if a high reverse voltage would be applied. As mentioned before, this has to be avoided.

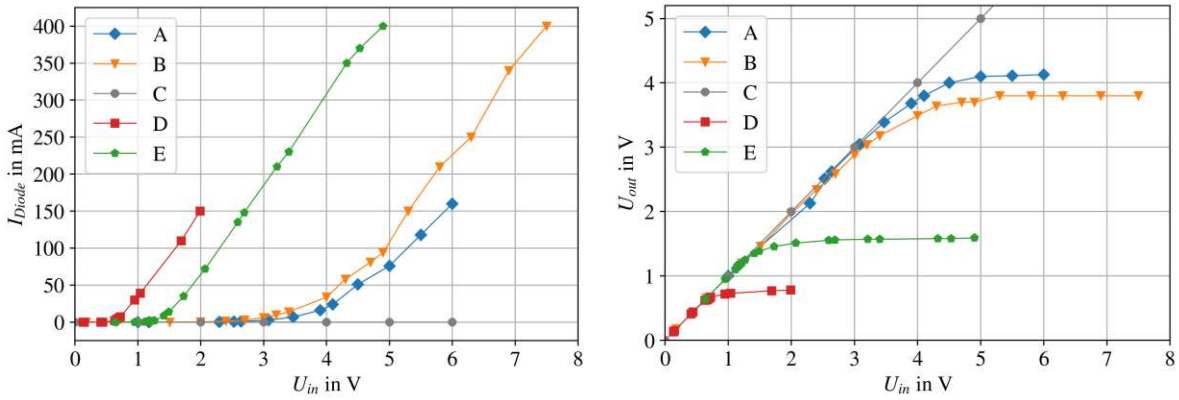

(a) The current flow through the diodes I_{diode} against the voltage applied to the over-voltage protection circuit U_{in}.

(b) Voltage applied to the over-voltage protection circuit U_{in} against voltage measured at the output of the protection circuit U_{out}.

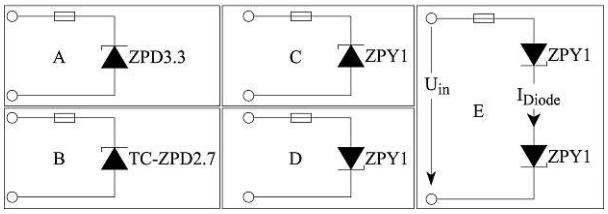

(c) Schematics of the 5 different over-voltage protection circuits that were investigated as possible candidates. The fuse used is the same in all 5 versions and therefore not labelled.

Fig. 4.3: Results of the experiments carried out to find the best diode for the over-voltage protection circuit.

Figure 4.3a shows that the current flow through the diodes I_{diode} rises fast as soon as a voltage value above the breakdown voltage is reached. It would then continue to rise even faster with increasing U_{in} if there was no serial resistance by the 200 mA FF fuse. Figure 4.3b shows that at low voltage values, the voltage across the diodes (seen by the ADC) equals U_{in} because I_{diode} is negligibly small. However, due to the rapid increase in I_{diode} after the breakdown voltage, the voltage across the diodes is capped slightly above this respective breakdown voltage. They can therefore protect the circuit attached to them from over-voltage.

4.2 Operation of the EHC

For the following experiments using pure H_2 or mixtures of H_2 with N_2/CH_4, the EHC setup as shown in Figure 3.1 had to be connected to an external gas mixing and measurement unit. This unit uses multiple mass flow controllers (MFCs) by Bronkhorst (Kamen, Germany) to create gas mixtures over a wide concentration range. All % gas concentrations shown in this chapter are % (v/v) (unless directly stated otherwise). The MFCs used were all of the type "mini CORI-FLOW" and were remote-controlled by a PC running a process control software. H_2 or CH_4 concentrations of the permeate and retentate were measured using a gas analyser by Sick (Waldkirch, Germany).

4.2.1 Separation

The first experiment was the attempt to separate H_2 from a gas mixture of 60 g/h N_2 and 3 g/h H_2. Because of the extremely low density of H_2 gas, this mixture is about 41 % H_2 by volume. This gas mixture was sent to the unit through the "Main Inlet" port seen on the very left in the flowchart in Figure 3.2. To ensure adequate humidity, valve V3 was opened all the way and valve V2 was closed. The entire inlet gas stream therefore passed through the humidifier before reaching the compressor. The needle valve V7 was kept open during the experiment because pure separation without compression was to be tested. The two gas streams exiting through the "Permeate Measurement Out" port and the "Retentate Measurement Out" port were alternately sent to the gas analyser to determine their hydrogen concentration. (See discussion in section 5.2.4 for accuracy of gas analyser measurements)

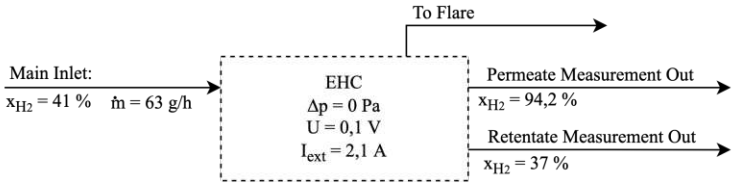

Fig. 4.4: Results of the first experiment with the entire setup as described. H_2 concentration and mass flow at the main inlet were determined using the MFCs. The H_2 concentration at the two outlets was determined using the gas analyser (see section 4.2 for information on gas analyser and MFCs). The gas streams which are not currently measured are sent directly to the flare.

The increase in H_2 mass fraction achieved during this experiment equates to an enrichment factor of $\beta_{H2} \approx 10,8$ (using mass fractions) with equation (2.3).

4.2.2 Compression

To test the second possible operational mode described in section 2.6.5, a number of experiments was carried out using a pure stream of H_2 (5 g/h) as the feed. This time the needle valve V7 was closed all the way to allow the EHC to build up pressure on its cathode side. The incoming gas stream was again humidified as much as the humidifier allowed by opening valve V3 all the way and keeping valve V2 closed. The voltage applied to the cell was kept constant for each series, and the resulting pressure/time curves were recorded. The results are shown in Figure 4.5. Each of the resulting curves has an almost linear increase in pressure over time. The way the curves deviate from increasing linearly by sloping downwards is also a shared feature amongst the data-sets. To make this trend away from a linear increase easier to see, a second graph was

produced. It only contains the data set at 0,75 V and 2,9 A together with an extrapolation of the linear approximation to the first 40 seconds of this data set (Figure 4.6). This data set was chosen specifically because the deviation from linear behaviour for sets with a low ΔP or sets at a low voltage is so small that it is almost invisible even with the linear approximation as a visual aid.

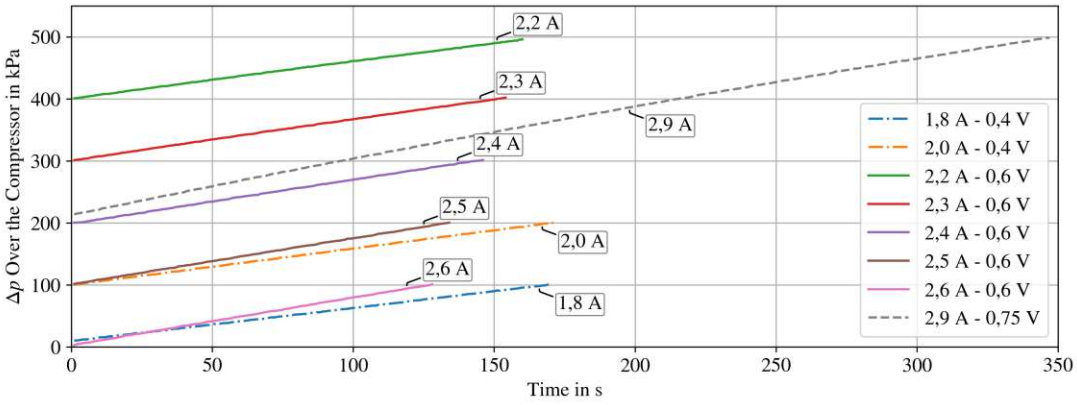

Fig. 4.5: Pressure difference building up over the compressor with time. All curves in this graph were recorded with the thermostatic bath at 30 °C and the feed H_2 flux (pure) kept constant at 5 g/h.

The reason why each of the curves is bending downwards is that all of the curves are recorded with a constant voltage applied to the EHC. At the same voltage, the current being drawn by the EHC gets lower as the pressure difference over the compressor increases (will be discussed in section 5.1.3). Following the Faraday equation (2.11), this drop of current leads to a lower flux of hydrogen being transported through the membrane and therefore to a decrease in the slope of pressure over time. This trend (higher pressure difference leads to lower currents) can also be seen when comparing all the curves recorded at 0,6 V shown in Figure 4.5 to each other. Every 1 bar increase in starting pressure decreases the average current over the respective compression by 0,1 A (see all series with solid line in Figure 4.5).

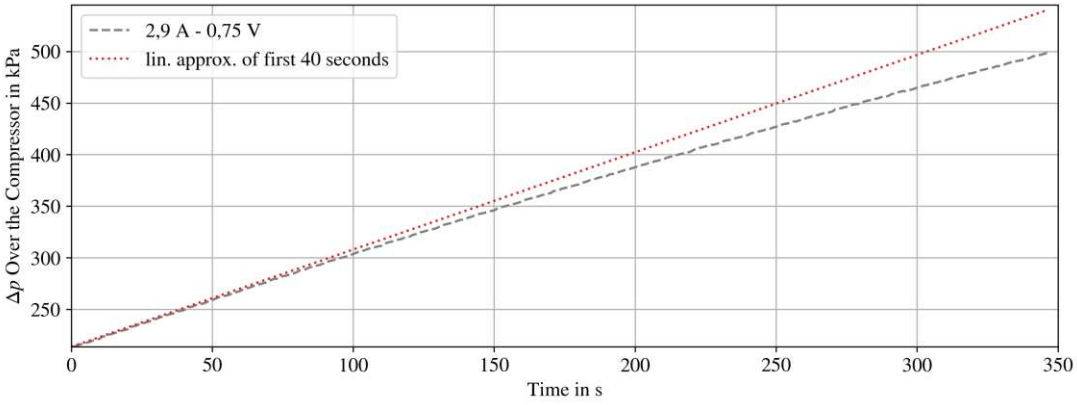

Fig. 4.6: To help visualise the non-linearity of the compression curves in the previous Figure (4.5), a linear approximation for the first 40 seconds of a data set is plotted together with the data set itself. The linear approximation was found using the equation: $\Delta p_L = kt + d = [(\Delta p(t = 40) - \Delta p(t = 0))/40]t + \Delta p(t = 0)]$

The decrease of current with increased pressure is not equally pronounced under all operational conditions. The currents shown as data labels in Figure 4.5 are the average currents ($\bar{I}$) for the respective series. Table 4.1 in the following section shows these average currents ($\bar{I}$) together with a percentage value describing how pronounced the drop of current with pressure (and therefore the slope downwards from increasing linear) for this series is. It is calculated by $(I(t_0) - I(t_{end}))/(\bar{I} \times \Delta p) \times 100$. Higher percentage values (and therefore a stronger deviation from linear increase) are found for higher voltages and for higher pressure differences. This finding is in agreement with the polarisation curves found in the upcoming section 4.2.5, as they also fork out more with increasing voltage.

4.2.3 Determining Dead Volume on the Permeate Side

Experiments using a gas flow meter (Definer), as shown later in section 4.2.6, confirmed that the current efficiency of the EHC is very close to 100 % for the operational conditions achievable with this setup. This means that the current I can, to some extent, be used as a proxy for the flux through the compressor by using an equation derived from the Faraday equation (2.11) and the equation of state for an ideal gas (pv=nRT). This equation (4.1) together with the compression data shown in the last section 4.2.2, allowed to calculate the dead volume. This dead volume calculation includes: The volume of the cathode chamber of the EHC stack, the tubing on the outlet side of the EHC stack cathode up to the valve V7 (including the tubing to the pressure sensor) and the tubing on the inlet of the EHC stack cathode from the stack to the valve V1 (see flowchart in Figure 3.2 for labels).

$$V_{Dead} = \frac{\bar{I}RT}{zF}\frac{\Delta t}{\Delta p} \tag{4.1}$$

Tab. 4.1: Calculation of the dead volume from a number of experiments. All data sets are recorded at a temperature of 30 °C for the thermostatic bath and a feed stream of 100 % H_2 with 5 g/h

Series	Current Drop per bar in %	$\Delta p/\Delta t$ in Pa/s	$\bar{I}$ in A	V_{Dead} in cm^3
2 bar–5 bar 0,75 V	7,0	741,59	2,9	50,6
0 bar–1 bar 0,36 V	-3,3	483,14	1,8	48,2
1 bar–2 bar 0,40 V	0,0	529,42	2,0	48,9
2 bar–3 bar 0,57 V	5,4	627,02	2,4	49,5
0 bar–1 bar 0,57 V	2,7	690,56	2,6	48,7
1 bar–2 bar 0,57 V	2,8	668,11	2,5	48,4
3 bar–4 bar 0,57 V	6,1	594,41	2,3	50,0
4 bar–5 bar 0,57 V	5,0	537,12	2,2	53,0

The average dead volume from all values found in Table 4.1 computes to 49,6 mL. Assuming accuracy of the flow rate measurement with the definer and the current measurement with the hall effect current sensor, we can calculate the standard deviation to be 1,6 mL.

4.2.4 Separation and Compression - Unsteady State

The EHCs two operational modes “compression” and “separation” have now been successfully demonstrated. The next step, as mentioned in section 2.6.5, was to combine the two modes and simultaneously separate and compress. This time valve V7 was closed completely to create back pressure on the cathode side. Figure 4.7 depicting a pressure over time curve for a stream of 5 % H_2 in CH_4, looks very similar to figure 4.5, depicting compression of H_2 from a pure gas stream. As long as no mass transfer limitations occur or substances in the feed interact with the catalyst or membrane, compression out of a gas mixture behaves the same as compression of pure H_2.

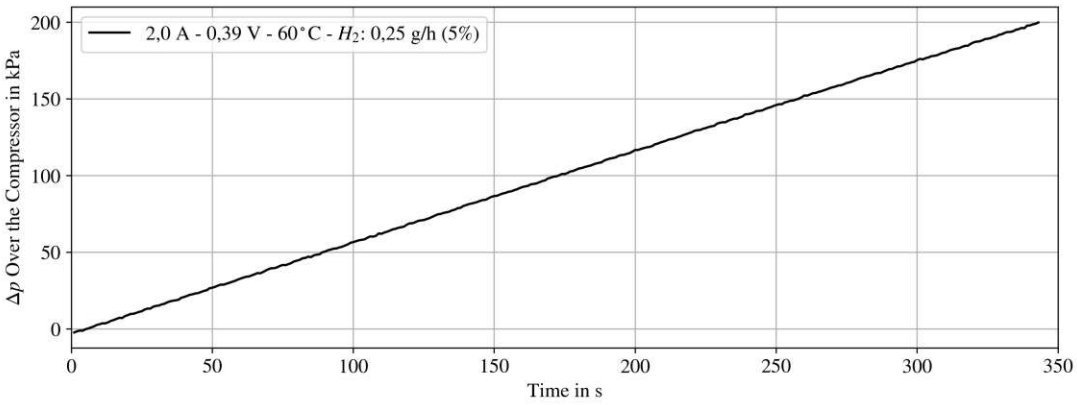

Fig. 4.7: Pressure difference building up over the compressor with time. The curve shows compression of H_2 out of a dilute feed (bath temperature and H_2 concentration are given in the data label). The diluent used was CH_4.

4.2.5 Polarisation Curves - Influence of Feed, Pressure and Temperature

The Δp over time plots shown in Figures 4.5, 4.6 and 4.7 were all produced with the back pressure valve V7 completely closed or open all the way to create either no back pressure at all for pure separation, or block flow out of the cathode chamber to increase the pressure in it over time.

For the following sets of data, we are leaving this unsteady state and will turn to steady state operation of the EHC. To do this, the position of the needle valve V7 needs to be very carefully adjusted to maintain a constant Δp over time. Then, a constant voltage is applied to the stack for some period of time. The voltage and current are measured, recorded and averaged over this steady time period to get a single data point. The voltage is then changed to another value and kept constant for some period of time again to record the next data point. These sets of data at constant voltage and current can then be combined to create a polarisation curve for a specific operational mode. The influence of the parameters $\Delta p, T$, H_2 concentration and flow rate are shown in the following Figures (4.8b, 4.8a, 4.8c)

Generally for EHCs, flatter polarisation curves are better since this means that less overpotential is required for operation. Less overpotential means fewer losses occur, less energy is required and a higher efficiency is achieved. The influence of temperature shown in Figure 4.8b is similar to what could be expected from theory and literature. Higher temperatures are favourable for EHC operation (see section about electrochemical energy conversion 2.2 or the sections about influence of temperature on different sources of overpotential 2.4.6).

The influence of the feed shown in Figure 4.8c also roughly follows the pattern expected from theory about concentration polarisation (section 2.4.6.4). Lower feed concentrations of H_2 lead to higher overpotentials and therefore to worse polarisation curves. More experiments with different

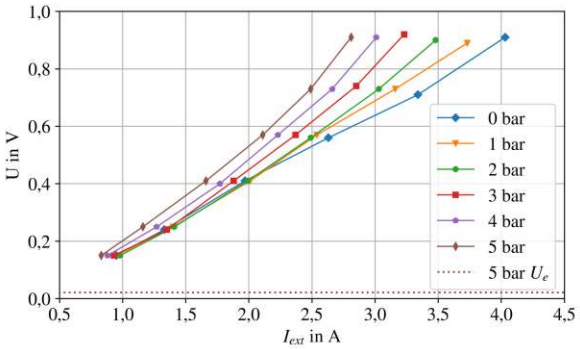

(a) Influence of back pressure on polarisation curves of the EHC. All curves in this Figure were recorded at 30 °C and with a pure H_2 feed of 5 g/h.

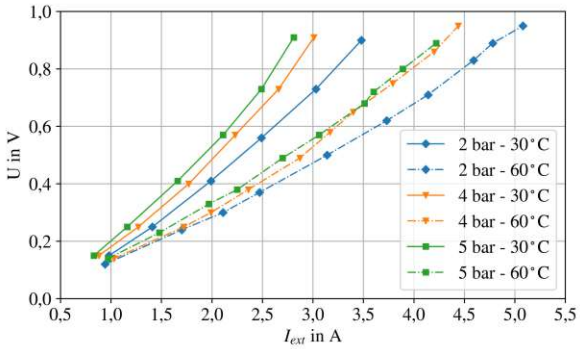

(b) Influence of temperature on polarisation curves of the EHC stack. All curves in this Figure were recorded with a pure H_2 feed of 5 g/h.

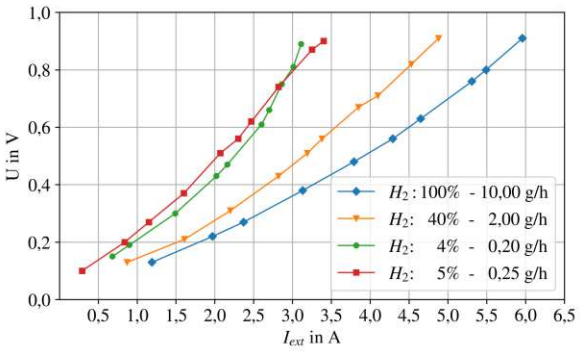

(c) Influence of feed flow rate and concentration on polarisation curves of the EHC stack. The blue, orange and green lines were recorded during one experiment using N_2 to dilute the H_2. The red line was recorded in a different experiment on a different day using CH_4 to dilute the H_2. All data in this Figure was acquired at 60 °C and with a constant pressure difference of 2 bar over the compressor.

Fig. 4.8: A collection of polarisation curves at different operating conditions

feed compositions should be conducted after the issues with the compressor stack (discussed later in section 5.1.3) and hysteresis (discussed later in section 5.2.1) are resolved, to validate these findings.

The Influence of differential pressure over the compressor shown in figure 4.8a will be discussed in much detail in section 5.1.3.

4.2.6 Separation and Compression - Steady State

A number of experiments were carried out in which the gas stream exiting the EHC during steady state operation was characterised. The volumetric flow rate of the permeate was measured using a "Definer 220-L Rev. C1" by Bios international Corp (NJ, USA), the composition of this gas was measured using the previously mentioned (section 4.2) gas analyser, and the feed was preset using the previously mentioned mass flow controllers. The results of these experiments are displayed in a series of seven Figures (4.9 to 4.15). The values directly determined during the experiments are printed in black in these Figures while values that were calculated from the experimentally determined ones are shown in orange. Since the following seven Figures contain a lot of information, some noteworthy observations will be pointed out to the reader here. As mentioned before, all gas concentrations given in % are % (v/v) unless directly stated otherwise.

The first five Figures (4.9 to 4.13) all have similar operational conditions at 60 °C, about 0,4 V and a pressure difference of 2 bar. However, they do differ in their feed composition. Mixtures in the range of 80 %–4 % H_2 with N_2 as the diluent were used in these experiments. Every drop in H_2 feed concentration leads to a slightly higher overall efficiency μ_{ehc} caused by increases in voltage efficiency μ_v. The permeate flow rate does slightly drop with every decrease in H_2 feed concentration. However, looking at the percentage of H_2 that the EHC was able to remove from the feed in a single pass, we can see a drastic increase. The EHC removed 3 % of the total hydrogen in the feed from a feed containing 80 % H_2. With the lowest hydrogen feed concentration tested (4 %) the EHC was able to remove 33,6 % of the total feed H_2.

The experiment in Figure 4.14 with a H_2 feed concentration of 5 % is very similar to the five previous experiments already discussed. However, this time the diluent was not N_2 but CH_4.

The experiment shown in Figure 4.15 differs from all others in a number of factors and is therefore hardly comparable. The operational conditions were different at 30 °C, 0,19 V and a higher pressure difference of 5 bar. The feed in this case was not a mixture with another gas but pure H_2. Even though direct comparison with the other experiments is difficult, one peculiarity is worth pointing out: Although current and voltage efficiencies μ_i and μ_v respectively, are similar to the ones in the previous experiments, the power consumption in kWh/Nm^3 was only about half of all that observed in all previous experiments.

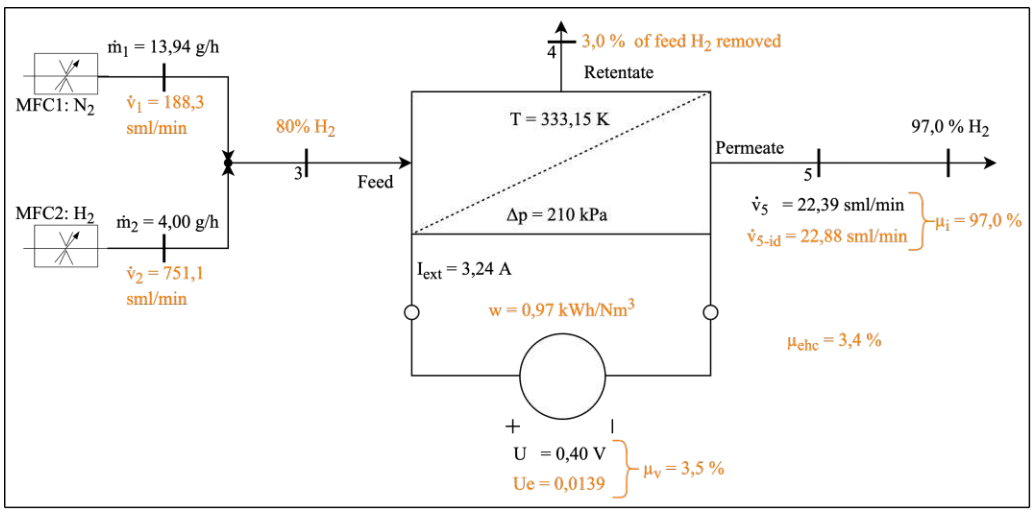

Fig. 4.9: Compilation of experimental results in steady state with a feed of 80 % H_2

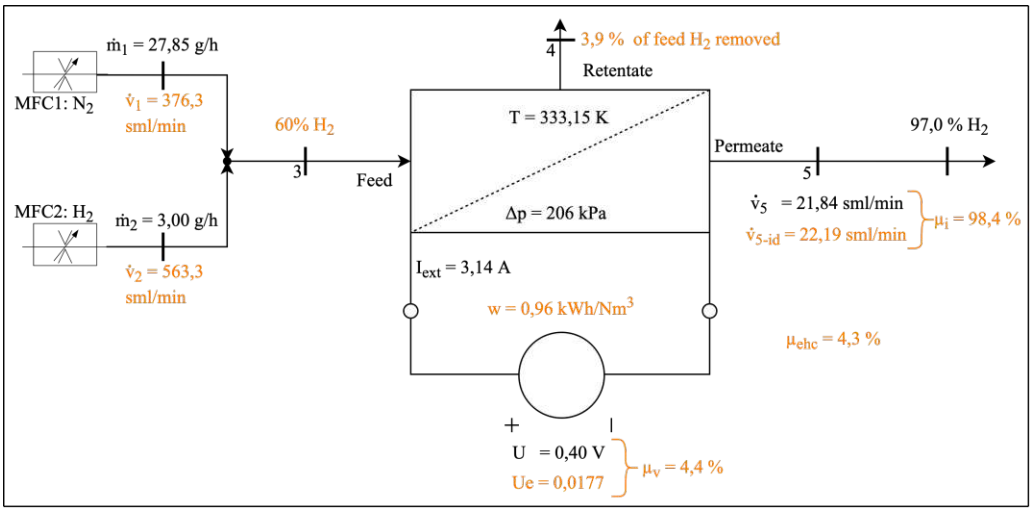

Fig. 4.10: Compilation of experimental results in steady state with a feed of 60 % H_2

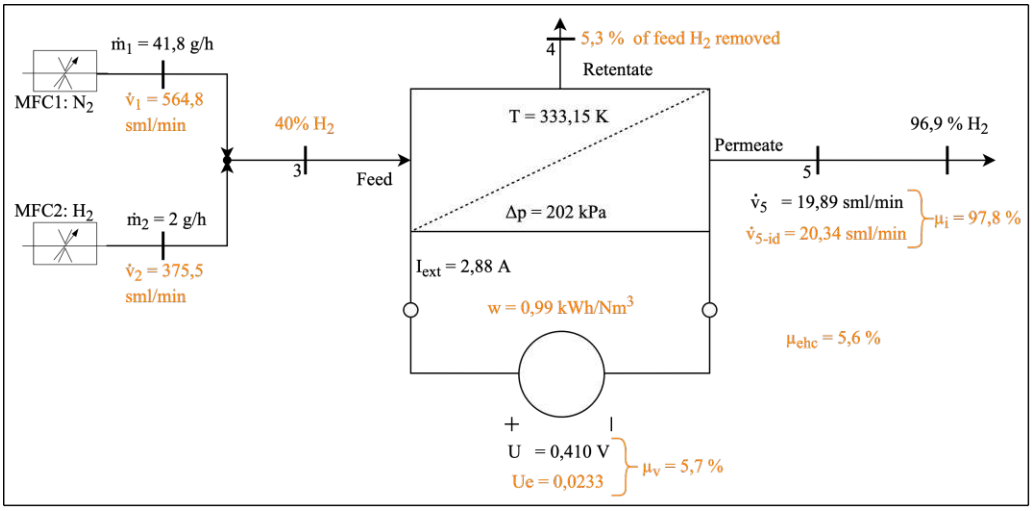

Fig. 4.11: Compilation of experimental results in steady state with a feed of 40 % H_2

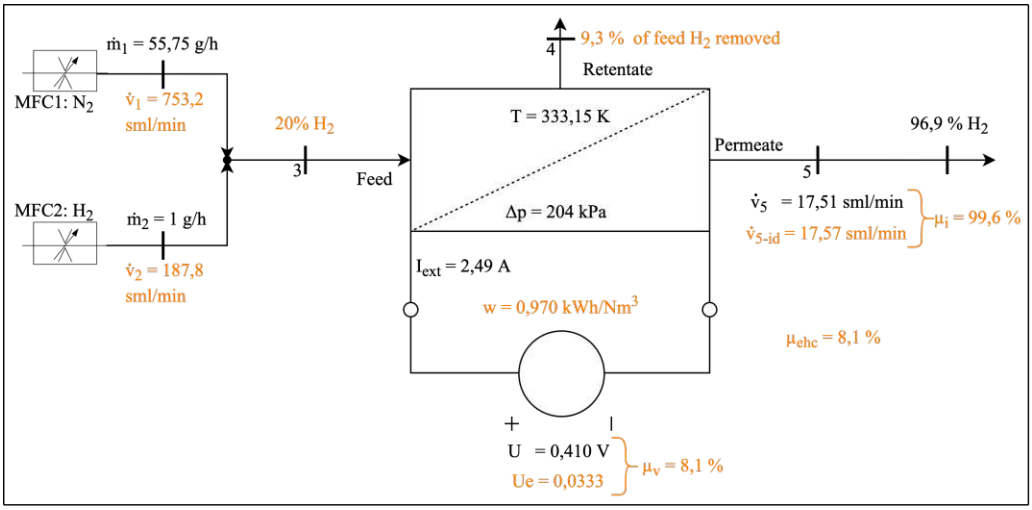

Fig. 4.12: Compilation of experimental results in steady state with a feed of 20 % H_2

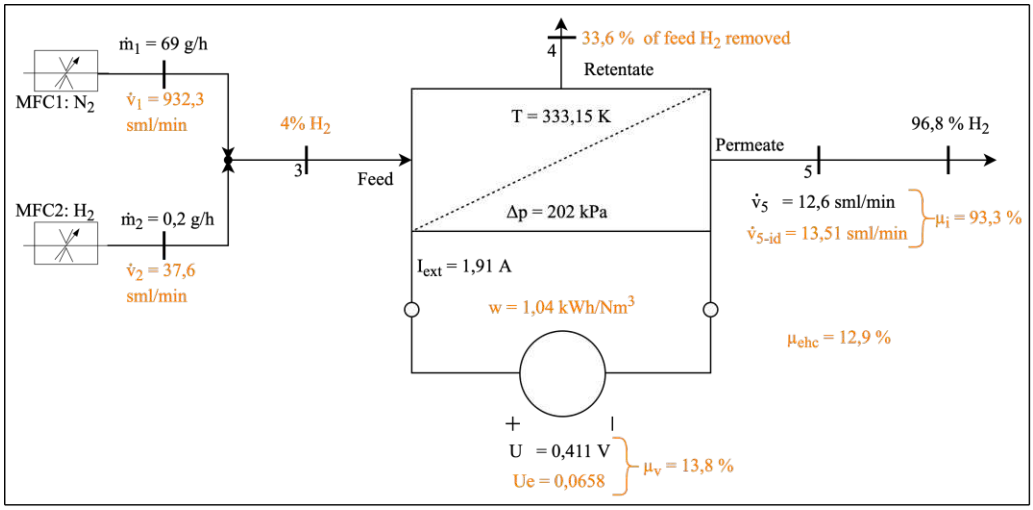

Fig. 4.13: Compilation of experimental results in steady state with a feed of 4 % H_2

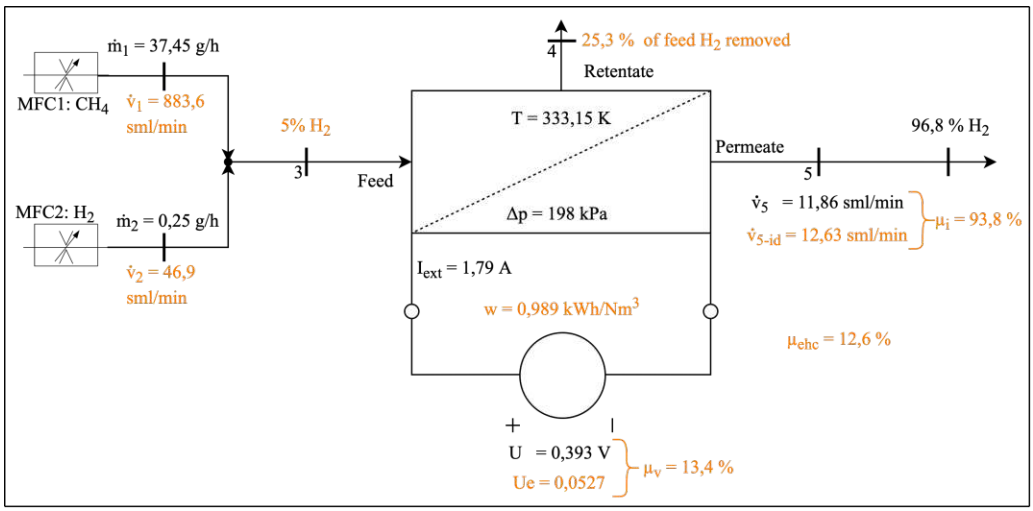

Fig. 4.14: Compilation of experimental results in steady state with a feed of 5 % H_2 in CH_4

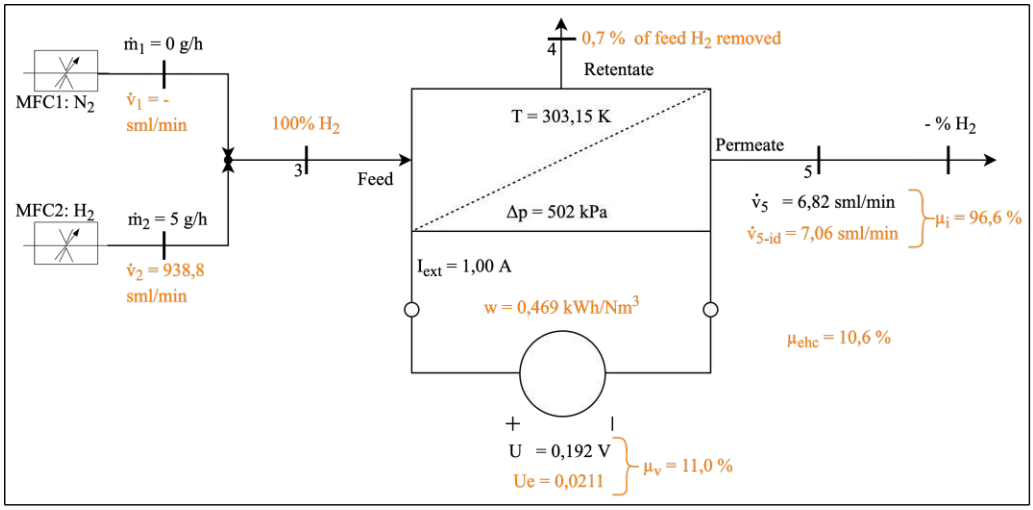

Fig. 4.15: Compilation of experimental results in steady state using pure H_2

Chapter 5

Discussion and Conclusions

Engineering a functional prototype of an EHC based on a patent and a previous Bachelor's thesis [4, 3] was the task I set out to fulfil when beginning to work on this Master's thesis. Although the tests described in the previous section confirmed that this task was undoubtedly accomplished, many challenges still have to be overcome to achieve the greater goals described in the motivation section of this work. With more research, electrochemical hydrogen compression might prove to be an important puzzle piece in the transition towards a future of exclusively using renewable energy. The first experiments performed on this laboratory scale EHC unit also revealed that there is plenty of room for improvement, and many more experiments could be carried out using this unit to fully characterise it. In this chapter we want to briefly look at some of the "lessons learned" during construction, we want to scrutinise the results obtained during the first days of operation for potential sources of error, and we want to give an outlook on possible future experiments one could perform using this setup.

5.1 Lessons Learned and Potential Improvements

5.1.1 The Compressor Power Supply

DC power supplies for high currents are expensive. According to an IRENA report from 2020 [14, p. 52], they make up about 27,5 % of the total costs of a commercial PEM electrolyser plant. The power supply used to supply DC to the EHC in this setup was comparatively cheap at 249 €. Therefore we should not be surprised that the quality of the provided DC voltage is not entirely perfect in every regard.

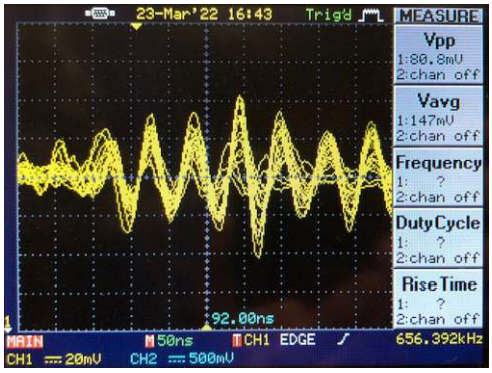

Fig. 5.1: The "PS900W" power supply set to 0,1 V DC is connected to an oscilloscope in parallel to the compressor as a load. The oscilloscope, set to 20 mV/division vertically, shows AC noise of about 80 mV peak to peak.

- Even though the data sheet of the "PS900W" states a voltage range of 0 V–15 V for the current range of 0 A–60 A, the lowest voltage achievable when the power supply is powered

on, is not actually zero. The display on the power supply might show 0,0 V but currents of up to 1,2 A were still observed flowing through the compressor. Using a multimeter, a DC voltage of 0,03 V was observed in this instance.

- There is a lot of AC noise superimposed on the DC voltage. Figure 5.1 shows the voltage signal when measured with an oscilloscope. The average DC voltage, displayed by the power supply, is 0,1 V (0,15 V according to the oscilloscope). The peak to peak value of the superimposed noise with this setting is around 0,08 V. For these low voltage values, the noise is about 50 % of the applied voltage. The influence of this AC noise on the compressor is not known and should either be determined experimentally/through a literature review, or the DC voltage should be be improved for future experiments by using filters or a higher quality DC power supply.

5.1.2 Corrosion

As determined in section 3.3, the thermostatic bath requires addition of Na_2CO_3 to prevent corrosion of the stainless steel parts submerged in the bath. However, two important facts were not sufficiently borne in mind at the time of designing the gas humidifier:

- Na_2CO_3 in water will create a slightly alkaline pH. This is good for preventing corrosion of stainless steel but not good for the passivation layer of aluminium. The original design (Figure 5.2a) for the gas humidifier consisted of a frame made from 20 mm x 20 mm extruded aluminium profiles holding the stainless steel humidifier tank.
- The L-brackets used to connect said extruded aluminium profiles to each other are readily available from a number of suppliers. They are typically manufactured from zinc or aluminium [74, 75] and come with galvanised steel screws for attaching them to the aluminium profiles. This meant a number of metals with very different positions in the electrochemical voltage series were now submerged in a slightly alkaline water bath. Therefore, intense galvanic corrosion occurred over the course of only two days.

Because of this, a new design for the frame holding the humidifier had to be built after the first tests using the thermostatic bath. Figure 5.2 shows the original design (Figure 5.2a), an example for the corrosion that occurred after two days in the bath (Figure 5.2b), and the new design consisting only of heat resistant polymers and stainless steel (5.2c).

(a) The original humidifier design using extruded aluminium profiles as a frame that was held together by zinc brackets with steel screws

(b) Corrosion over the course of two days

(c) New design for the humidifier. Two plates made from polycarbonate are connected by threaded rods made from Polyamid

Fig. 5.2: The original gas humidifier design had to be replaced by a new and corrosion-resistant one. In the new design, only polymers and stainless steel are in contact with the water in the thermostatic bath.

5.1.3 Design of the Compressor Stack and the Current Collector Plates

Even though the EHC successfully passed every test performed (section 4.2), there is a lot of room for improvement to its operation. The voltage efficiencies observed were under 10 % in many experiments and never surpassed 20 %. Possibly due to the same root cause, the currents observed with the setup were way lower than expected from literature about EHCs. Many publications report current densities covering the full range from 0 A/cm^2–1 A/cm^2 or even slightly above it. [43, 45, 46, 68, 76]. Companies that work on this technology make even bolder claims presenting current densities of up to 2,5 A/cm^2 [64], 2,2 A/cm^2 [77], or 1,2 A/cm^2 [63]. These numbers do seem feasible, however, since 2 A/cm^2 is considered a conservative value for PEM electrolysis and current densities of 6 A/cm^2 or more are expected to be achievable in the next few decades [14].

The current shown in the Figures of the results section is not displayed in A/cm^2 because this would yield very low and impractical values. Therefore, the current was just displayed in A. The highest current *density* observed with the realised setup was 0,119 A/cm^2 at 0,91 V. This is much lower than results achieved in literature. Only one publication reported even lower current densities, albeit slightly obscured by reporting the values in A/m^2. Casati et al. [42] report that:

> *By using lower values of current density (i =*20 A/m^2*) [...] it is possible to obtain a stationary value of the voltage[...]. After many runs we hypothesized that this behaviour is due to the dehydration of the membrane and decided to partially flood with water the gas flow channels in the cathode compartment, with the aim of getting a constant degree of humidity inside the membrane. Actually no improvement has been obtained, but a schizophrenic behaviour was observed [...]. Summarising these results it is possible to say that stable operating conditions can be obtained with low values of current density and high values of the feed flow rate (FFR). At the temperature of* 343 K *stable operating conditions can be obtained at higher current densities (i =*40 A/m^2*) but always with high FFR[...]*

Changing the values reported by Casati et al. [42] to the more commonly reported dimension of current density, we find that they achieved a range of 0,002 A/cm^2–0,006 A/cm^2. (20 A/m^2–60 A/m^2). At this point, no definite answer can be given as to what causes the low observed current density and the high observed overpotentials with the realised setup. The explanation of membrane dehydration proposed by Casati et al. [42] in the quotation above does seem reasonable and is supported by the observed hysteresis discussed later in this chapter (5.2.1). However, it might not be the only effect at play. The fact that the polarisation curves presented in the results section (4.8) have such a strong dependency on back pressure is indicative of another problem pending. The theoretical external electrolysis voltage U_e required to power the EHC, is expected to increase with increasing back pressure due to the $ln(p_{H_2cat}/p_{H_2an})$ term in the Nernst equation for EHCs (2.67). This increase however, is way smaller than the increase observed experimentally. Using the Nernst equation we can calculate that U_e for a back pressure of 0 bar and pure H_2 on both the anode and cathode side is 0 V. U_e for a back pressure of 5 bar and pure H_2 on the anode and cathode is 0,021 V (brown dotted line in 4.8a). If the difference in open circuit voltage is not causing the difference between the polarisation curves at different pressures, it has to be some form of overpotential. Looking back at section 2.4.6 in the theoretical chapter, we find that back pressure should not have as strong of an influence on overpotential as it appears to have in these experiments.

- Activation overpotentials, caused by slow reactions at the electrodes are not expected to increase with increasing back pressure
- Concentration polarisation should also not be affected by a higher pressure on the cathode side since it rises when the anode side is depleted of reactants
- Losses caused by back diffusion *are* expected to increase with higher back pressure. However, this does not seem to be happening in this case. The current efficiencies presented in section 4.2.6 show a negligible decrease in current efficiency with increasing back pressure. Back diffusion therefore does not seem to be the root cause of this increase in overpotential.

After ruling out the other options, this leaves Ohmic losses as a potential cause for the larger than expected discrepancy between the different polarisation curves at different pressures. Another hint that Ohmic losses are the cause for the discrepancy, is the linear increase of overpotential with increasing current, especially at 0 bar pressure difference (Figure 5.3). When comparing the linear approximations for higher back pressures shown in Figure 5.3 with their respective experimental data, one could argue that there is exponential or higher order growth of overpotential superimposed on the linear increase. Exponential increase would be a sign of concentration polarisation. I would argue that this is not what is happening here. Ohmic losses are described by the equation $\eta_\Omega = r_\Omega * i$. This function leads to a linear increase in overpotential only if we assume that r_Ω stays constant for different pressures and for low to high current densities. If we further recall that $r_\Omega = r_{\Omega_i} + r_{\Omega_e} + r_{\Omega_c}$ (from 2.4.6.3), it seems reasonable to describe the non linear growth even with this simple model.

Let us recall the two questions we are trying to answer:

1. Why is there a large discrepancy between the polarisation curves at different back pressures when U_e does not increase by much?

   If the membrane is not properly clamped down in its membrane holder, the contact resistance Ω_c may become a function of pressure. With pressure applied to the membrane, it might flex and be in contact with the conductive backplates only in some areas. This means that the effective current density in those small spots of contact is way higher than

the current density that would be calculated by just dividing the total current by the total membrane area.

2. Why does the increase in overpotential seem to have a component of faster than linear growth even at the very low current densities achieved with this setup (compared to literature) and with high H_2 feed flow rates?

   If, as speculated, parts of the membrane are not in good contact with the back plate, this could cause a high local current density. This could explain the faster-than-linear growth in more than one way. Either the membrane gets locally depleted of reactants because the reaction at these few spots is occurring so fast that diffusion becomes limiting (as explained in the theoretical chapter about concentration polarisation 2.4.6.4), or the local high current densities heat up these spots of the membrane and thereby dry it out locally. As mentioned in the theoretical section about ohmic losses 2.4.6.3, the ionic conductivity of the membrane is strongly dependant on membrane humidity. If local overheating occurs, this would increase r_{Ω_i} as currents get higher, and consequently lead to a non linear increase in overpotential. This theory of local membrane overheating is supported by the hysteresis effect that was observed when returning to lower current after operating at high current (see section 5.2.1).

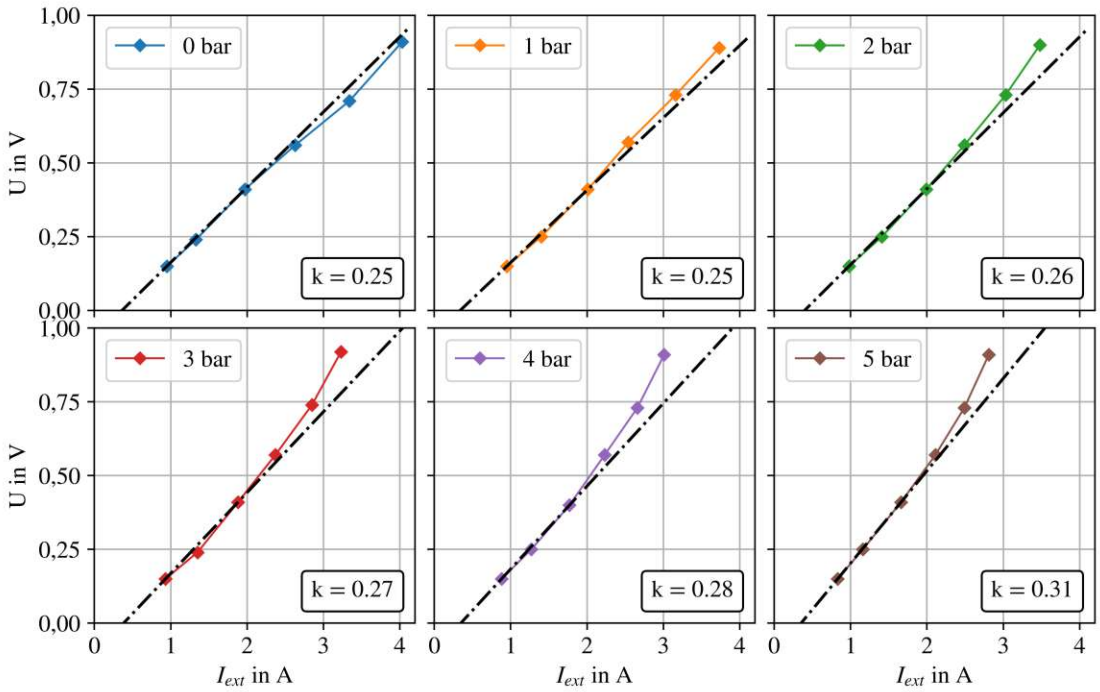

Fig. 5.3: Polarisation curves for pure H_2 (5 g/h at 30 °C) with pressure differences from 0 bar–5 bar. The black dash-dotted lines are linear approximations created by connecting the data-point at the lowest current with the data-point at the third lowest current. The k value in the lower right of each plot is the slope of the respective linear approximation ($\Delta U/\Delta I_{ext}$).

The two key messages of Figure 5.3 are:

- The slope k ($\propto r_\Omega$) of the polarisation curves increases with increasing pressure difference.

- With 0 bar pressure difference, there seems to be a linear increase in overpotential only while every curve at higher Δp does seem to show non-linearity.

Both effects could be explained by the equation $\eta_\Omega = (r_{\Omega_i}(I) + r_{\Omega_e} + r_{\Omega_c}(\Delta p)) \times i$. Further experiments are undoubtedly necessary to determine whether or not this speculative explanation is founded in reality. It is, however, at least plausible that the observed behaviour is caused by this.

5.1.4 Further Setup Improvement Proposals

- An improvement to the setup that would most likely be worth wile, is redesigning the membrane holder to make the stack assembly less tedious and ensure a better and more even clamping force on the membrane while maintaining its good characteristics like the very low susceptibility to concentration polarisation. The back plate design with thin meandering flow channels leads to high gas velocities and therefore low influence of lower hydrogen feed concentrations. Unlike Grigoriev et al. [45], who found very strong mass transfer limitations even with 62 % H_2 in the feed and concluded that "[the EHC] cannot be used to extract hydrogen efficiently from diluted sources", we were able to remove more than 33 % of the H_2 from a feed that only contained 4 % H_2 to begin with. In addition this operation was not accompanied by a large drop in efficiency (see section 4.2.6).

- For redesigning the membrane holder a material should be chosen that is less susceptible to corrosion than the aluminium currently used. Aluminium was mostly used for its good machinability but already showed slight signs of corrosion after the first three days of performing experiments on the system. For material choices refer to section 2.6.4 or literature about the subject.

- There is currently no possibility to create any back pressure on the collective outlet leading to the flare. This was an intended design choice made in the planning phase because it should not be possible to close the flare outlet and therefore create high pressures in any part of the setup not protected by the pressure relief safety valve. However, if we want to measure not just the composition but also the absolute amount of gas leaving the setup through the retentate or permeate measurement out-port (valve V6 or V9), we currently have no way of telling whether or not all the gas is exiting the setup through this measurement port, or if a fraction is still flowing through the respective non-return valves 1 or 2 and leaving through the collective outlet. Replacing the non-return valves to change their opening pressure from the current 0,1 bar to some higher pressure would be an option. This would, however, make it impossible to operate the EHC without back pressure because the gas has to go through these valves to exit via the flare outlet. Another option would be to replace said non-return valves with adjustable pressure difference valves. When planning future experiments on the setup, this should be considered.

- As mentioned multiple times in the section about sensors and electronics (3.5), the over-voltage protection would not function if the stack voltage measurement was connected to the stack the wrong way around. Applying a high reverse voltage would most likely damage the ADC or the Arduino. This could possibly be solved by adding another diode of the same type in parallel to the two diodes that are already included in the setup (see wiring diagram in Figure 3.8 or diode selection in the results section 4.1.3). The diode's direction would have to be reversed so it starts conducting at about 0,7 V reverse voltage and therefore protects the circuit from reverse over-voltage by breaking the 200 mA fuse.

- Setting a desired back pressure using the needle valve V7 is currently a tedious process because the adjustability of this valve is poor. Very small changes in the valve's position lead to huge changes in flow rate. Replacing this valve with a multi turn needle valve (with scale) might allow an easier definition of the desired back pressure.
- Set/check the torque for the M16 EHC screws to ensure suitable pressure is applied to the gastkets and the stack as a whole.
- Add a "droplet collector" after the humidifier to prevent the relative humidity sensor from getting splashed with water.

5.2 Discussion of Results and Possible Sources of Error

The influence of back pressure on the polarisation curves has already been discussed in the previous section because it closely ties into the most likely necessary redesign of the membrane holder/ the current collector plates. Some further noteworthy points about the gathered results will now be given.

5.2.1 Hysteresis in Current Measurements

After recording a number of polarisation curves as described in the results section 4.2.5 (holding everything else constant and then cycle through different voltages to record some voltage and current values to average over), a problematic effect was observed. It seemed to make a difference for the resulting polarisation curve, whether the voltages were cycled from low to high or from high to low (e.g. [1 V; 0,9 V; ...; 0,1 V] vs [0,1 V;0,2 V; ...; 1 V]). To further explore this, a number of polarisation curves was recorded in which both directions were recorded together. One of these is shown in Figure 5.4a.

When changing from higher to lower currents, the performance at the same voltage is worse than the performance at this voltage when coming from lower currents. The effect only occurs in the higher current ($>\approx 3$ A) regions and the two curves recombine into one again at low currents. The cause for this effect can be well observed in a graph of current against time after a voltage change as shown in Figure 5.4b. The voltage changes in Figure 5.4b with 0,1 V–1,0 V and 1,0 V–0,2 V are of course very large, but this makes the effect clearly visible. It evidently makes a difference whether the average current is calculated over the first 20 seconds after changing to a new voltage value or whether the first 20 seconds after changing voltage are ignored and the following 20 seconds are used for averaging. This Figure also suggests that recovering from a high current event (orange series) takes more time than the opposite effect when reaching a high current (blue series). After some time at constant voltage a new stable current is reached. This effect is possibly caused by local overheating of the membrane due to uneven contact with the current collector plate, and the membrane has to humidify again at lower currents before a higher current is possible again. Since this effect was only discovered on the third (and last) day of performing experiments on the setup, it is not entirely clear whether or not this effect is included in some of the data presented in this thesis. For future experiments this has to be borne in mind.

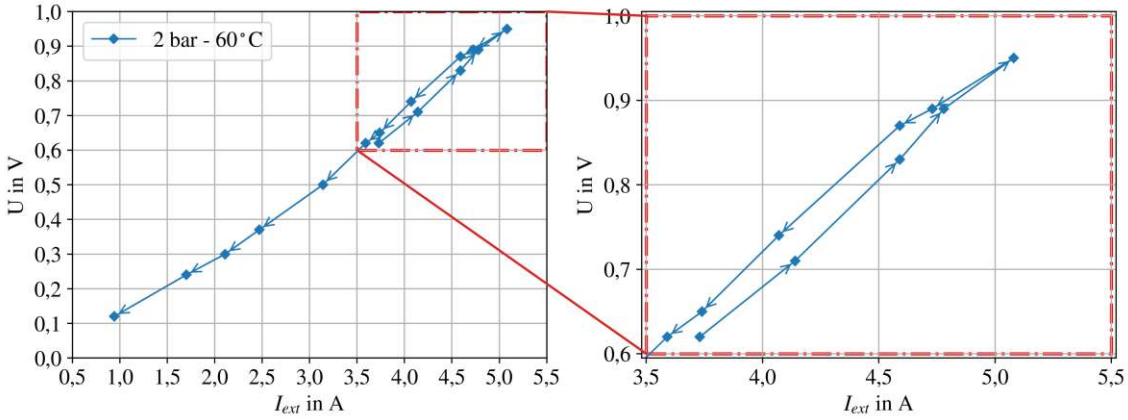

(a) A polarisation curve created by scanning voltage values in both directions. First the voltage was increased, and after reaching the highest voltage, it was decreased until the lowest voltage was reached (depicted by the arrows).

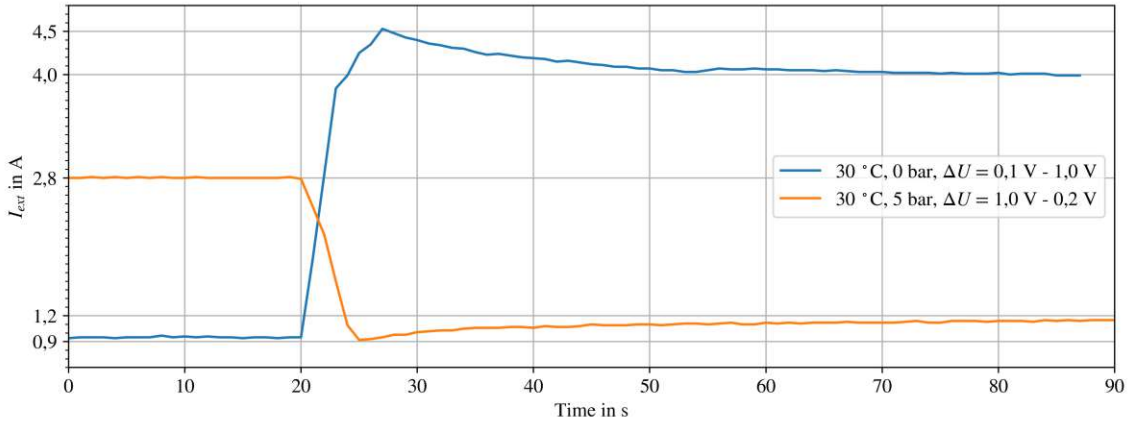

(b) Two time series of current after a voltage change.

Fig. 5.4: A polarisation curve showing the hysteresis effect that was observed multiple times and a time series of current to visualise where this effect is coming from

5.2.2 Voltage

The voltage measurement, as mentioned in the realisation chapter, is performed using a 16 bit ADC. This ADC determines the voltage applied to the reactor at a single point in time. How frequent this measurement is performed, can be set by issuing a command to the Arduino via USB. The voltage readings produced by this ADC were very noisy, and could vary by more than 100 % from one measured value to the next (with a few ms in between the two measurements). When averaging over longer time periods (e.g. over 50 values recorded within 10 seconds) the average voltage value became very stable. Looking at Figure 5.1 depicting the noise superimposed on the DC voltage, makes it easy to see how the voltage measurement could be so noisy. Depending on chance, we might measure the voltage at a peak or a trough of the superimposed noise and therefore get a higher or lower DC voltage reading with every measurement. This also explains why averaging works very well to get rid of the noise. This problem could possibly be solved by adding a capacitor of appropriate size to the ADC to smooth out the noise in the measurement. Other options include upgrading to a better DC power supply or just being aware that the noise is present and always averaging the voltage readings over

a sufficiently large number of samples. This could also be done directly on the Arduino by implementing some averaging code. When choosing this averaging route, however, the sampling frequency should be adjusted after measuring the frequency of the AC noise to make sure all measurement points will not fall in peaks or troughs of the noise and the resulting average will not be skewed.

5.2.3 Temperature

The PT100 RTDs used to monitor the temperature of the thermostatic bath, the compressor anode and cathode, and the gas cooler all delivered very stable values. Although they were all submerged in the same thermostatic bath, they showed differences in temperature of up to 0,3 °C. If a future stack design allows to operate at currents higher than the ~6 A achieved currently, it might be worth while to correct the slight offsets that the RTDs display at the moment. This offset could possibly be corrected by submerging all of them in the thermostatic bath, very close to each other, and then correcting the offset by adjusting the potentiometer on the respective PT100 signal transducer in the electronics distribution cabinet, until all of them show the same, correct temperature. This would allow to detect slight temperature changes of the cathode or anode of the EHC if future operations at higher current are performed.

5.2.4 Gas Composition Using the Gas Analyser

The gas analyser used to determine the composition of the permeate had not been calibrated for some time and therefore showed a strong offset that was not corrected in the data presented in this work. Even when supplying pure H_2 directly to it, the measured value never reached values above 98 %. A similar offset was observed for measurements of CH_4 concentrations. If pure CH_4 was supplied to it, the gas analyser would display about 104 % CH_4. It was determined that, for this work, the exact percentage values are not of critical importance to prove that the separation process using the EHC is working. All the permeate H_2 concentrations given in the results section are in the high 90 percent region. The actual concentration is probably even closer to 100 % than the values presented here. Underestimating the EHC separation performance is better than overestimating it, and therefore it was not tried to correct the offsets. For future experiments it could be worth while to calibrate the gas analyser before trying to get precise results for the permeate and retentate concentration.

5.3 Future Experiments and Outlook

The number of future experiments and improvements that could be done is large. A few of them are presented here as bullet points for quick reference.

- Send gas to the EHC with different humidities by using the two needle valves V2 and V3
- Flood the cathode chamber with water for membrane humidification as was done in some literature about EHCs (see 2.6.3)
- Create new stack design to try and resolve the issues described in section 5.1.3
- Improve over voltage protection circuit as described in section 4.1.3
- Use other gas mixtures than H_2 + N_2, H_2 + CH_4 or even non-binary gas mixtures and measure polarisation curves, separation efficiency, energy consumption, etc.

- Try other membranes. E.g. thinner and thicker membranes of the same type (Nafion^{TM}) or new high-performance proton exchange membranes like Aquivion^{TM} or others
- Create new current collector plate designs out of materials that are more corrosion resistant than the aluminium presently used
- Measure the humidity of the permeate produced by the EHC. Water transport is theoretically expected to mostly move water towards the cathode chamber (see 2.6.3). However during the first experiments, no noticeable amount of water was observed to be condensed in the gas cooler coming from the cathode, while the anode side gas cooler had to be drained from condensate about every hour of operation.
- Calibrate the gas analyser for more precise measurement of separation characteristics (see 5.2.4)
- Investigate amount of non non H_2 gases in the permeate by including permeability of Nafion^{TM} in calculations and/or performing precise measurements of contaminants in the permeate.
- Compare single stage and multi stage EHC operation by building a stack with multiple membranes that can be connected in parallel/in series or a combination of the two by adequately designed bipolar plates.

While some issues still need to be ironed out, the project performed in this Master's thesis was a success overall. With energy requirements in the range of around 0,5 kW h–1,0 kW h for every Nm^3 of H_2 the system needed about 17 %–33 % of hydrogens lower heating value (LHV) in the form of electrical energy to extract H_2 from a variety of feed streams (down to 4 % H_2) and release it with very high purity at a pressure of up to six times the feed pressure. This currently does not compare extremely favourable to the 8 % of the higher heating value [51] (= 9,5 % of the LHV) that classical mechanical compression requires to compress H_2 from 1 bar to 200 bar. After a future version of this test setup manages to remove the efficiency limitations currently faced by this EHC, the energy required for compression can most likely be lowered by a very significant amount. Performing a more extensive study comparing these two technologies will be much more fruitful at this point in time.

However, as mentioned before in section 2.4.7 the pure efficiency of electrochemical hydrogen compression is not its only benefit. Being able to selectively remove H_2 from a very dilute gas stream and compress it in a single step is the true strength. In this thesis we were already able to demonstrate this operational mode successfully. In the future, after removing said efficiency bottlenecks, a very interesting investigation would be comparing the combined energy requirement and cost of performing this EHCs operational mode (compression and purification in a single step) with the combined energy requirement and cost of classical methods to perform the same task.

Bibliography

[1] R. Moradi and K. M. Groth. "Hydrogen storage and delivery: Review of the state of the art technologies and risk and reliability analysis". In: *International Journal of Hydrogen Energy* 44.23 (May 2019), pp. 12254–12269. ISSN: 03603199. DOI: 10.1016/j.ijhydene.2019.03.041. URL: https://linkinghub.elsevier.com/retrieve/pii/S0360319919309656 (visited on 03/28/2022).

[2] K. Müller. "Technologien zur Speicherung von Wasserstoff. Teil 1: Wasserstoffspeicherung im engeren Sinn". In: *Chemie Ingenieur Technik* 91.4 (Apr. 2019), pp. 383–392. ISSN: 0009-286X, 1522-2640. DOI: 10.1002/cite.201800043. URL: https://onlinelibrary.wiley.com/doi/10.1002/cite.201800043 (visited on 03/28/2022).

[3] V. Halmschlager. "Energy Demand for the Separation of Hydrogen from H2/CH4 Mixtures by Proton Exchange Membrane Systems". Bachelor Thesis. TU-Wien, 2015.

[4] W. Liemberger, M. Harasek, and M. Miltner. "Method for Separating Hydrogen from Gas Mixtures". Pat. WO2019180032A1. Univ-Wien-Tech. Sept. 26, 2019.

[5] Linde-Gas. *Datentabelle Wasserstoff*. Linde-Gas-GmbH. URL: https://www.linde-gas.at/de/images/1007_rechnen_sie_mit_wasserstoff_v110_tcm550-169419.pdf (visited on 03/29/2022).

[6] F. Barbir. *PEM fuel cells: theory and practice*. 2nd ed. Amsterdam ; Boston: Elsevier/Academic Press, 2013. 518 pp. ISBN: 978-0-12-387710-9.

[7] RÖMPP-Redaktion, F. Geldsetzer, and U. Jahn. *Methan*. In: ed. by F. Böckler, B. Dill, G. Eisenbrand, F. Faupel, B. Fugmann, T. Gamse, R. Matissek, G. Pohnert, A. Rühling, S. Schmidt, and G. Sprenger. Thieme Gruppe, June 25, 2020. URL: https://roempp.thieme.de/lexicon/RD-13-01634 (visited on 03/30/2022).

[8] J. Hartmann-Schreier. *Wasserstoff*. In: ed. by F. Böckler, B. Dill, G. Eisenbrand, F. Faupel, B. Fugmann, T. Gamse, R. Matissek, G. Pohnert, A. Rühling, S. Schmidt, and G. Sprenger. Thieme Gruppe, May 26, 2004. URL: https://roempp.thieme.de/lexicon/RD-23-00368 (visited on 03/30/2022).

[9] RÖMPP-Redaktion. *Propan*. In: ed. by F. Böckler, B. Dill, G. Eisenbrand, F. Faupel, B. Fugmann, T. Gamse, R. Matissek, G. Pohnert, A. Rühling, S. Schmidt, and G. Sprenger. Thieme Gruppe, Mar. 1, 2002. URL: https://roempp.thieme.de/lexicon/RD-16-04306 (visited on 03/30/2022).

[10] M. Habermeyer and F. Geldsetzer. *Dieselkraftstoff*. In: ed. by F. Böckler, B. Dill, G. Eisenbrand, F. Faupel, B. Fugmann, T. Gamse, R. Matissek, G. Pohnert, A. Rühling, S. Schmidt, and G. Sprenger. Thieme Gruppe, June 27, 2012. URL: https://roempp.thieme.de/lexicon/RD-04-01383 (visited on 04/01/2022).

[11] C. Achten. *Benzin*. In: ed. by F. Böckler, B. Dill, G. Eisenbrand, F. Faupel, B. Fugmann, T. Gamse, R. Matissek, G. Pohnert, A. Rühling, S. Schmidt, and G. Sprenger. Thieme Gruppe, Dec. 13, 2009. URL: https://roempp.thieme.de/lexicon/RD-02-00799 (visited on 04/01/2022).

[12] IEA. *Hydrogen – Analysis and key findings*. Paris: International Energy Agency, Nov. 2021. URL: https://www.iea.org/reports/hydrogen (visited on 03/29/2022).

[13] IEA. *The Future of Hydrogen*. Paris: International Energy Agency, 2019, p. 203. URL: https://www.iea.org/reports/the-future-of-hydrogen.

[14] IRENA. *Green hydrogen cost reduction: Scaling up electrolysers to meet the 1.5C climate goal*. Abu Dhabi: International Renewable Energy Agency, 2020, p. 106.

[15] IRENA. *Hydrogen: A renewable energy perspective*. Abu Dhabi: International Renewable Energy Agency, 2019, p. 52.

[16] WOE. *Innovation Insights Brief - New Hydrogen Economy Hype or Hope?* World Energy Council, 2019. URL: https://www.worldenergy.org/publications/entry/innovation-insights-brief-new-hydrogen-economy-hype-or-hope (visited on 03/29/2022).

[17] H. Hofbauer. *Skriptum zur Vorlesung Brennstoff und Energietechnologie 159.830*. 2019.

[18] S. Kuczyński, M. Łaciak, A. Olijnyk, A. Szurlej, and T. Włodek. "Thermodynamic and Technical Issues of Hydrogen and Methane-Hydrogen Mixtures Pipeline Transmission". In: *Energies* 12.3 (Feb. 12, 2019), p. 569. ISSN: 1996-1073. DOI: 10.3390/en12030569. URL: http://www.mdpi.com/1996-1073/12/3/569 (visited on 09/17/2022).

[19] P. Kurzweil. *Angewandte Elektrochemie: Grundlagen, Messtechnik, Elektroanalytik, Energiewandlung, technische Verfahren*. Wiesbaden: Springer Fachmedien Wiesbaden, 2020. ISBN: 978-3-658-32420-9. DOI: 10.1007/978-3-658-32421-6. URL: http://link.springer.com/10.1007/978-3-658-32421-6 (visited on 04/04/2022).

[20] "CHAPTER 7 - Production of Electricity". In: *Sustainable Nuclear Power*. Ed. by G. J. Suppes and T. S. Storvick. Burlington: Academic Press, Jan. 1, 2007, pp. 185–200. ISBN: 978-0-12-370602-7. DOI: 10.1016/B978-012370602-7/50024-7. URL: https://www.sciencedirect.com/science/article/pii/B9780123706027500247.

[21] J. M. Kurtz, S. Sprik, G. Saur, and S. Onorato. *Fuel Cell Electric Vehicle Durability and Fuel Cell Performance*. NREL/TP–5400-73011, 1501675. Mar. 13, 2019, NREL/TP–5400–73011, 1501675. DOI: 10.2172/1501675. URL: http://www.osti.gov/servlets/purl/1501675/ (visited on 04/22/2022).

[22] VDI e. V., ed. *VDI-Wärmeatlas*. Berlin, Heidelberg: Springer Berlin Heidelberg, 2013. ISBN: 978-3-642-19980-6. DOI: 10.1007/978-3-642-19981-3.

[23] P. Linstrom and W. Mallard. *NIST Chemistry WebBook, NIST Standard Reference Database 69*. Type: dataset. National Institute of Standards and Technology, 1997. DOI: 10.18434/T4D303. URL: http://webbook.nist.gov/chemistry/ (visited on 04/15/2022).

[24] *Mitsubishi Heavy Industries, Ltd. Global Website | MHI Completes Development of the J-series Gas Turbine*. Mitsubishi Heavy Industries, Ltd. URL: https://www.mhi.com/news/0903121287.html (visited on 05/06/2022).

[25] *Siemens erreicht Weltrekorde in Düsseldorfer Kraftwerk "Fortuna"*. SIEMENS AG Press Release. URL: https://press.siemens.com/global/de/feature/siemens-erreicht-weltrekorde-duesseldorfer-kraftwerk-fortuna (visited on 05/06/2022).

[26] *Kraft-Wärme-Kopplung » Infos & Erklärung*. Wien Energie. URL: https://www.wienenergie.at/ueber-uns/unternehmen/energie-klimaschutz/energieerzeugung/kraft-waerme-kopplung/ (visited on 09/15/2022).

[27] R. W. Baker. *Membrane technology and applications*. 3rd ed. Medium: electronic resource. Chichester, West Sussex ; Hoboken: John Wiley & Sons, 2012. 1 p. ISBN: 978-1-118-35971-6.

[28] M. Mulder. *Basic Principles of Membrane Technology*. Dordrecht: Springer Netherlands, 1996. ISBN: 978-94-009-1766-8. DOI: 10.1007/978-94-009-1766-8. URL: http://link.springer.com/10.1007/978-94-009-1766-8 (visited on 06/24/2022).

[29] K. Scott. *Handbook of Industrial Membranes*. OCLC: 476113539. Burlington: Elsevier, 1995. ISBN: 978-0-08-053289-9. URL: http://public.ebookcentral.proquest.com/choice/publicfullrecord.aspx?p=318417 (visited on 06/24/2022).

[30] M. Harasek. *Skriptum zu 166.654 VO Membrantechnik*. 2019. URL: https://tiss.tuwien.ac.at/course/educationDetails.xhtml?courseNr=166654&semester=2019W&dswid=4894&dsrid=298.

[31] A. Dicks and D. A. J. Rand. *Fuel cell systems explained*. Third edition. Hoboken, NJ, USA: Wiley, 2018. 1 p. ISBN: 978-1-118-70696-1.

[32] M. Ciobanu, J. P. Wilburn, M. L. Krim, and D. E. Cliffel. "1 - Fundamentals". In: *Handbook of Electrochemistry*. Ed. by C. G. Zoski. Amsterdam: Elsevier, Jan. 1, 2007, pp. 3–29. ISBN: 978-0-444-51958-0. DOI: 10.1016/B978-044451958-0.50002-1. URL: https://www.sciencedirect.com/science/article/pii/B9780444519580500021.

[33] H.-J. Foth. *chemisches Potential*. In: ed. by F. Böckler, B. Dill, G. Eisenbrand, F. Faupel, B. Fugmann, T. Gamse, R. Matissek, G. Pohnert, A. Rühling, S. Schmidt, and G. Sprenger. Thieme Gruppe, Aug. 7, 2006. URL: https://roempp.thieme.de/lexicon/RD-03-01203 (visited on 04/28/2022).

[34] J. Fleig. *Technische Elektrochemie*. 2022. URL: https://tiss.tuwien.ac.at/course/courseDetails.xhtml?dswid=9177&dsrid=712&courseNr=164216&semester=2020W (visited on 05/04/2022).

[35] J. Fleig. *Skriptum - Elektrochemische Energieumwandlung und Energiespeicherung*. 2022. URL: https://tiss.tuwien.ac.at/course/courseDetails.xhtml?dswid=2801&dsrid=506&courseNr=164288&semester=2022S (visited on 05/04/2022).

[36] I. Riess. "What does a voltmeter measure?" In: *Solid State Ionics* 95.3 (Mar. 1, 1997), pp. 327–328. ISSN: 01672738. DOI: 10.1016/S0167-2738(96)00542-5. URL: https://linkinghub.elsevier.com/retrieve/pii/S0167273896005425 (visited on 05/05/2022).

[37] A. McNaught and A. Wilkinson. *standard hydrogen electrode*. In: *IUPAC Compendium of Chemical Terminology, 2nd ed. (the "Gold Book")*. Blackwell Scientific Publications, Oxford, 1997. DOI: 10.1351/goldbook.S05917. URL: https://doi.org/10.1351/goldbook.S05917 (visited on 09/15/2022).

[38] E. Amores, J. Rodríguez, J. Oviedo, and A. de Lucas-Consuegra. "Development of an operation strategy for hydrogen production using solar PV energy based on fluid dynamic aspects". In: *Open Engineering* 7.1 (June 14, 2017), pp. 141–152. ISSN: 2391-5439. DOI: 10.1515/eng-2017-0020. URL: https://www.degruyter.com/document/doi/10.1515/eng-2017-0020/html (visited on 05/16/2022).

[39] V. Liso, G. Savoia, S. S. Araya, G. Cinti, and S. K. Kær. "Modelling and Experimental Analysis of a Polymer Electrolyte Membrane Water Electrolysis Cell at Different Operating Temperatures". In: *Energies* 11.12 (Nov. 23, 2018), p. 3273. ISSN: 1996-1073. DOI: 10.3390/en11123273. URL: http://www.mdpi.com/1996-1073/11/12/3273 (visited on 05/16/2022).

[40] C. Song, Y. Tang, J. L. Zhang, J. Zhang, H. Wang, J. Shen, S. McDermid, J. Li, and P. Kozak. "PEM fuel cell reaction kinetics in the temperature range of 23–120°C". In: *Electrochimica Acta* 52.7 (Feb. 2007), pp. 2552–2561. ISSN: 00134686. DOI: 10.1016/j.electacta.2006.09.008. URL: https://linkinghub.elsevier.com/retrieve/pii/S0013468606009583 (visited on 05/17/2022).

[41] D. G. Bessarabov and P. Millet. *PEM water electrolysis*. Hydrogen energy and fuel cells primers volume 1-2. London [England] ; San Diego, CA: Academic Press, 2018. 2 pp. ISBN: 978-0-12-811145-1.

[42] C. Casati, P. Longhi, L. Zanderighi, and F. Bianchi. "Some fundamental aspects in electrochemical hydrogen purification/compression". In: *Journal of Power Sources* 180.1 (May 2008), pp. 103–113. ISSN: 03787753. DOI: 10.1016/j.jpowsour.2008.01.096. URL: https://linkinghub.elsevier.com/retrieve/pii/S037877530800222X (visited on 04/04/2022).

[43] G. Sdanghi, J. Dillet, S. Didierjean, V. Fierro, and G. Maranzana. "Feasibility of Hydrogen Compression in an Electrochemical System: Focus on Water Transport Mechanisms". In: *Fuel Cells* 20.3 (June 2020), pp. 370–380. ISSN: 1615-6846, 1615-6854. DOI: 10.1002/fuce.201900068. URL: https://onlinelibrary.wiley.com/doi/10.1002/fuce.201900068 (visited on 04/04/2022).

[44] C. Vayenas, M. Tsampas, and A. Katsaounis. "First principles analytical prediction of the conductivity of Nafion membranes". In: *Electrochimica Acta* 52.6 (Jan. 2007), pp. 2244–2256. ISSN: 00134686. DOI: 10.1016/j.electacta.2006.03.109. URL: https://linkinghub.elsevier.com/retrieve/pii/S0013468606008280 (visited on 05/20/2022).

[45] S. Grigoriev, I. Shtatniy, P. Millet, V. Porembsky, and V. Fateev. "Description and characterization of an electrochemical hydrogen compressor/concentrator based on solid polymer electrolyte technology". In: *International Journal of Hydrogen Energy* 36.6 (Mar. 2011), pp. 4148–4155. ISSN: 03603199. DOI: 10.1016/j.ijhydene.2010.07.012. URL: https://linkinghub.elsevier.com/retrieve/pii/S036031991001308X (visited on 04/04/2022).

[46] R. Ströbel, M. Oszcipok, M. Fasil, B. Rohland, L. Jörissen, and J. Garche. "The compression of hydrogen in an electrochemical cell based on a PE fuel cell design". In: *Journal of Power Sources* 105.2 (Mar. 2002), pp. 208–215. ISSN: 03787753. DOI: 10.1016/S0378-7753(01)00941-7. URL: https://linkinghub.elsevier.com/retrieve/pii/S0378775301009417 (visited on 04/04/2022).

[47] A. Chouhan, B. Bahar, and A. K. Prasad. "Effect of back-diffusion on the performance of an electrochemical hydrogen compressor". In: *International Journal of Hydrogen Energy* 45.19 (Apr. 2020), pp. 10991–10999. ISSN: 03603199. DOI: 10.1016/j.ijhydene.2020.02.048. URL: https://linkinghub.elsevier.com/retrieve/pii/S0360319920305784 (visited on 06/22/2022).

[48] F.-M. Barth. *Thermodynamik für Maschinenbauer*. 2. Auflage. De Gruyter Studium. Berlin Boston: De Gruyter Oldenbourg, 2016. 225 pp. ISBN: 978-3-11-041336-6.

[49] M. Haider. *Skriptum zur Vorlesung Angewandte Thermodynamik 302.073*. Oct. 2013.

[50] H. D. Baehr and S. Kabelac. *Thermodynamik: Grundlagen und technische Anwendungen*. Springer-Lehrbuch. Berlin, Heidelberg: Springer Berlin Heidelberg, 2009. ISBN: 978-3-642-00556-5. DOI: 10.1007/978-3-642-00556-5. URL: https://link.springer.com/10.1007/978-3-642-00556-5 (visited on 03/29/2022).

[51] M. Rhandi, M. Trégaro, F. Druart, J. Deseure, and M. Chatenet. "Electrochemical hydrogen compression and purification versus competing technologies: Part I. Pros and cons". In: *Chinese Journal of Catalysis* 41.5 (May 2020), pp. 756–769. ISSN: 18722067. DOI: 10.1016/S1872-2067(19)63404-2. URL: https://linkinghub.elsevier.com/retrieve/pii/S1872206719634042 (visited on 04/04/2022).

[52] *Universal and Individual Gas Constants*. Engineering ToolBox. 2004. URL: https://www.engineeringtoolbox.com/individual-universal-gas-constant-d_588.html (visited on 07/21/2022).

[53] *Air - Specific Heat vs. Temperature at Constant Pressure*. Engineering ToolBox. 2004. URL: https://www.engineeringtoolbox.com/air-specific-heat-capacity-d_705.html (visited on 07/21/2022).

[54] G. Sdanghi, G. Maranzana, A. Celzard, and V. Fierro. "Review of the current technologies and performances of hydrogen compression for stationary and automotive applications". In: *Renewable and Sustainable Energy Reviews* 102 (Mar. 2019), pp. 150–170. ISSN: 13640321. DOI: 10.1016/j.rser.2018.11.028. URL: https://linkinghub.elsevier.com/retrieve/pii/S1364032118307822 (visited on 07/20/2022).

[55] K. Onda, K. Ichihara, M. Nagahama, Y. Minamoto, and T. Araki. "Separation and compression characteristics of hydrogen by use of proton exchange membrane". In: *Journal of Power Sources* 164.1 (Jan. 2007), pp. 1–8. ISSN: 03787753. DOI: 10.1016/j.jpowsour.2006.10.018. URL: https://linkinghub.elsevier.com/retrieve/pii/S0378775306020635 (visited on 04/04/2022).

[56] B. L. Kee, D. Curran, H. Zhu, R. J. Braun, S. C. DeCaluwe, R. J. Kee, and S. Ricote. "Thermodynamic Insights for Electrochemical Hydrogen Compression with Proton-Conducting Membranes". In: *Membranes* 9.7 (July 1, 2019), p. 77. ISSN: 2077-0375. DOI: 10.3390/membranes9070077. URL: https://www.mdpi.com/2077-0375/9/7/77 (visited on 04/04/2022).

[57] L. Lipp. *Development of Highly Efficient Solid State Electrochemical Hydrogen Compressor (EHC)*. FuelCell Energy, Inc., June 2008, p. 15.

[58] J. Cornish. *Survey Results and Analysis of the Cost and Efficiency of Various Operating Hydrogen Fueling Stations*. Engineering Procurement and Construction, Lakewood, CO (United States), 2011.

[59] D. Henkensmeier, M. Najibah, C. Harms, J. Žitka, J. Hnát, and K. Bouzek. "Overview: State-of-the Art Commercial Membranes for Anion Exchange Membrane Water Electrolysis". In: *Journal of Electrochemical Energy Conversion and Storage* 18.2 (May 1, 2021), p. 024001. ISSN: 2381-6872, 2381-6910. DOI: 10.1115/1.4047963. URL: https://asmedigitalcollection.asme.org/electrochemical/article/18/2/024001/1085903/Overview-State-of-the-Art-Commercial-Membranes-for (visited on 04/09/2022).

[60] *Iridiumpreis | Umicore Precious Metals Management*. UMICORE AG. URL: https://pmm.umicore.com/de/preise/iridium/ (visited on 05/06/2022).

[61] M. Müller, M. Carmo, A. Glüsen, M. Hehemann, S. Saba, W. Zwaygardt, and D. Stolten. "Water management in membrane electrolysis and options for advanced plants". In: *International Journal of Hydrogen Energy* 44.21 (Apr. 2019), pp. 10147–10155. ISSN: 03603199. DOI: 10.1016/j.ijhydene.2019.02.139. URL: https://linkinghub.elsevier.com/retrieve/pii/S036031991930758X (visited on 04/12/2022).

[62] B. S. MacKenzie and D. P. Bloomfield. *Electrochemical Hydrogen Compressor*. Santa Fe: Analytic Power Corp, May 2006.

[63] M. Nordio, F. Rizzi, G. Manzolini, M. Mulder, L. Raymakers, M. Van Sint Annaland, and F. Gallucci. "Experimental and modelling study of an electrochemical hydrogen compressor". In: *Chemical Engineering Journal* 369 (Aug. 2019), pp. 432–442. ISSN: 13858947. DOI: 10.1016/j.cej.2019.03.106. URL: https://linkinghub.elsevier.com/retrieve/pii/S1385894719305716 (visited on 04/04/2022).

[64] M. Hamdan. *Electrochemical Compression*. GinerELX, 2018, p. 19.

[65] L. Vermaak, H. W. J. P. Neomagus, and D. G. Bessarabov. "Recent Advances in Membrane-Based Electrochemical Hydrogen Separation: A Review". In: *Membranes* 11.2 (Feb. 13, 2021), p. 127. ISSN: 2077-0375. DOI: 10.3390/membranes11020127. URL: https://www.mdpi.com/2077-0375/11/2/127 (visited on 04/19/2022).

[66] L. Schorer, S. Schmitz, and A. Weber. "Membrane based purification of hydrogen system (MEMPHYS)". In: *International Journal of Hydrogen Energy* 44.25 (May 2019), pp. 12708–12714. ISSN: 03603199. DOI: 10.1016/j.ijhydene.2019.01.108. URL: https://linkinghub.elsevier.com/retrieve/pii/S036031991930240X (visited on 05/16/2022).

[67] K. Onda, T. Araki, K. Ichihara, and M. Nagahama. "Treatment of low concentration hydrogen by electrochemical pump or proton exchange membrane fuel cell". In: *Journal of Power Sources* 188.1 (Mar. 2009), pp. 1–7. ISSN: 03787753. DOI: 10.1016/j.jpowsour.2008.11.135. URL: https://linkinghub.elsevier.com/retrieve/pii/S0378775308022866 (visited on 04/19/2022).

[68] J. Pineda-Delgado, A. Chávez-Ramirez, C. K. Gutierrez B, S. Rivas, C.-R. Marisela, R. de Jesús Hernández-Cortes, J. Menchaca-Rivera, and J. Pérez-Robles. "Effect of relative humidity and temperature on the performance of an electrochemical hydrogen compressor". In: *Applied Energy* 311 (Apr. 2022), p. 118617. ISSN: 03062619. DOI: 10.1016/j.apenergy.2022.118617. URL: https://linkinghub.elsevier.com/retrieve/pii/S0306261922000915 (visited on 04/19/2022).

[69] B. Rohland and K. Eberle. "Electrochemical hydrogen compressor". In: 43.24 (Aug. 21, 1998), p. 6. DOI: https://doi.org/10.1016/S0013-4686(98)00144-3.

[70] J. Sedlak, J. Austin, and A. Laconti. "Hydrogen recovery and purification using the solid polymer electrolyte electrolysis cell". In: *International Journal of Hydrogen Energy* 6.1 (1981), pp. 45–51. ISSN: 03603199. DOI: 10.1016/0360-3199(81)90096-3. URL: https://linkinghub.elsevier.com/retrieve/pii/0360319981900963 (visited on 10/01/2022).

[71] Mark Debe. *Final Report - Advanced Cathode Catalysts and Supports for PEM Fuel Cells*. DOE/GO/17007-1, 1052138. Sept. 28, 2012, DOE/GO/17007–1, 1052138. DOI: 10.2172/1052138. URL: http://www.osti.gov/servlets/purl/1052138/ (visited on 09/21/2022).

[72] IKA. *Betriebsanleitung für den IKA ICC basic Umwälzthermostat*. 2022. URL: https://www.ika.com/de/Produkte-Lab-Eq/Thermostate-Umwaelzthermostate-Einhaengethermostate-csp-272/ICC-basic-Downloads-cpdl-4134400/ (visited on 09/21/2022).

[73] *AllAboutCircuits: Hall Effect Current Sensing: Open-Loop and Closed-Loop Configurations - Technical Articles*. Aug. 20, 2022. URL: https://www.allaboutcircuits.com/technical-articles/hall-effect-current-sensing-open-loop-and-closed-loop-configurations/ (visited on 08/20/2022).

[74] Motedis. *Winkel für Aluminiumprofile von Motedis*. URL: https://www.motedis.com/shop/Winkel-fuer-Aluprofil__1203.html.

[75] B. Rexroth. *Winkel für Aluminiumprofile von Bosch Rexroth*. URL: https://www.boschrexroth.com/en/xc/products/product-groups/assembly-technology/basic-mechanic-elements/connection-elements/bracket.

[76] M.-T. Nguyen, S. A. Grigoriev, A. A. Kalinnikov, A. A. Filippov, P. Millet, and V. N. Fateev. "Characterisation of a electrochemical hydrogen pump using electrochemical impedance spectroscopy". In: *Journal of Applied Electrochemistry* 41.9 (Sept. 2011), pp. 1033–1042. ISSN: 0021-891X, 1572-8838. DOI: 10.1007/s10800-011-0341-9. URL: http://link.springer.com/10.1007/s10800-011-0341-9 (visited on 04/04/2022).

[77] L. Lipp. *Electrochemical Hydrogen Compressor*. Date for this source is unknown - possibly 2015. FuelCell Energy, Inc.

List of Figures

List of Tables

Chapter 6

Appendix

6.1 Information about Sensors Used and Component Suppliers

Tab. 6.1: Technical Information about the Sensors 1 to 3 in the flowchart in Figure 3.2

No. in 3.2	1	2	3
Measures	RH	T	ΔP
Location	Humidifier	Humidifier	Compressor
Product ID	FS3135	FS3135	AMS 3012-10000-D
Vendor	FuehlerSysteme eNET (Nürnberg, Germany)	FuehlerSysteme eNET (Nürnberg, Germany)	Analog Microelectronics (Mainz, Germany)
Powered by	24 V Power Supply	24 V Power Supply	24 V Power Supply
I_{total}	4 mA–20 mA	4 mA–20 mA	4 mA–20 mA
Signal	4 mA–20 mA	4 mA–20 mA	4 mA–20 mA
Range	0 %–100 % r.H	−20 °C–80 °C	0 bar–10 bar
V_{in}^{min}-V_{in}^{max}	15 V–36 V DC	15 V–36 V DC	10 V–36 V DC
R_m^{min}-R_m^{max}	0 Ω–500 Ω @24 V	0 Ω–500 Ω @24 V	0 Ω–600 Ω

Tab. 6.2: Technical Information about the Sensors 4 to 6 in the flowchart in Figure 3.2

No. in 3.2	4	5	6
Measures	T	T	T
Location	Gas Cooler	Anode Current Collector	Cathode Current Collector
Product ID	001-KSS-PT100-3L-1.0-W[1]	MU-PT1000-I420-EF6S-2.0-W	MU-PT1000-I420-EF6S-2.0-W
Vendor	Otom Group (Bräunlingen, Germany)	Otom Group (Bräunlingen, Germany)	Otom Group (Bräunlingen, Germany)
Powered by	24 V Power Supply	24 V Power Supply	24 V Power Supply
I_{total}	24 mA–44 mA	24 mA–44 mA	24 mA–44 mA
Signal	4 mA–20 mA	4 mA–20 mA	4 mA–20 mA
Range	−20 °C–50 °C[2]	0 °C–100 °C[2]	0 °C–100 °C[2]
V_{in}^{min}-V_{in}^{max}	12 V–34 V AC/DC	12 V–34 V AC/DC	12 V–34 V AC/DC
R_m^{min}-R_m^{max}	250 Ω–600 Ω	250 Ω–600 Ω	250 Ω–600 Ω

[1] This product ID only includes the fast responding PT100 RTD since it can not be bought as a set with a measurement transducer. The transducer was bought separately from the same vendor under the product ID “MU-PT1000-I420” [2] Selected with DIP switches

Tab. 6.3: Technical Information about the Sensors 7 to 9 in the flowchart in Figure 3.2

No. in 3.2	7	8	9
Measures	T	I	U
Location	Thermostatic Bath	Compressor	Compressor
Product ID	MU-PT1000-I420-KS-2.0-550-W	LEM LA 150-P	ADS1115
Vendor	Otom Group (Bräunlingen, Germany)	RS Components (Corby, UK)	AZ-Delivery (Deggendorf, Germany)
Powered by	24 V Power Supply	±12 V	Arduino 3,3 V
I_{total}	24 mA–44 mA	10 mA–45 mA	x
Signal	4 mA–20 mA	$I_{ext}/2000$	U
Range	0 °C–100 °C[1]	−212 A–212 A	0 V–1,4 V
V_{in}^{min}-V_{in}^{max}	12 V–34 V AC/DC	±12 V - ±15 V	3,3 V–5 V DC
R_m^{min}-R_m^{max}	250 Ω–600 Ω	0 Ω–40 Ω	x

[1] Selected with DIP switches

Tab. 6.4: Component suppliers for the setup. URLs confirmed to be working on September 12, 2022

Name	Homepage
Acrylstudio GmbH (Wiener Neudorf, Austria)	www.acrylstudio.eu
AISLER B.V. (Aachen, Germany)	www.aisler.net
Analog Microelectronics GmbH (Mainz, Germany)	www.analog-micro.com
AZ-Delivery Vertriebs GmbH (Deggendorf, Germany)	www.az-delivery.de
Conrad Electronic GmbH (Wels, Austria)	www.conrad.at
Edelstahl24 GmbH (Pichl bei Wels, Austria)	www.edelstahl24.com
ELV Elektronik AG (Salzburg, Austria)	de.elv.com
Fetter Baumarkt GmbH (Wien, Austria)	www.fetter.at
Fixmetall GmbH (Wels, Austria)	www.fixmetall-shop.com
Fluidify FT GmbH (Wolfurt, Austria)	www.fluidify.com
Zur Goldenen Kugel (Wien, Austria)	www.goldenekugel.at
Haym.Infotec GmbH (Salzburg, Austria)	www.haym.info
Ion Power GmbH (München, Germany)	www.ion-power.com
Otom Group GmbH (Bräunlingen, Germany)	www.sensorshop24.de
Persicaner und Co GmbH (Wien, Austria)	www.persicaner.at
QuinTech e.K. (Göppingen, Germany)	www.quintech.de
RS Components GmbH (Gmünd, Austria)	at.rs-online.com
Schraubenking GmbH (Altheim, Austria)	www.schraubenking.at
AA-Solutions GmbH (Wiener Neudorf, Austria)	www.swagelok.com
VWR International GmbH (Wien, Austria)	at.vwr.com/store/
Weh Austria (Naarn, Austria)	www.wehaustria.at
Witt Gastechnik GmbH (Witten, Germany)	www.wittgas.com

Tab. 6.5: What was procured by the respective component suppliers

Name	Components bought from this supplier
Acrylstudio GmbH (Wiener Neudorf, Austria)	Custom thermostatic bath made from PC
AISLER B.V. (Aachen, Germany)	PCB production from gerber files
Analog Microelectronics GmbH (Mainz, Germany)	Miniature pressure sensor
AZ-Delivery Vertriebs GmbH (Deggendorf, Germany)	ADS1115 ADC, breadboard, jumper cables, OLED display
Conrad Electronic GmbH (Wels, Austria)	various materials, small parts and electronic components
Edelstahl24 GmbH (Pichl bei Wels, Austria)	Cutting ring fittings, stainless steel fittings and more stainless steel material
ELV Elektronik AG (Salzburg, Austria)	Laboratory power supply for high currents
Fetter Baumarkt GmbH (Wien, Austria)	Winch
Fixmetall GmbH (Wels, Austria)	Aluminium for current collector back plates
Fluidify FT GmbH (Wolfurt, Austria)	Serto polymer screw fittings, stainless steel support sleeves for PTFE tubing
Zur Goldenen Kugel (Wien, Austria)	Small parts like screws, nuts and washers
Haym.Infotec GmbH (Salzburg, Austria)	CPU fans and copper CPU coolers
Ion Power GmbH (München, Germany)	Nafion CCMs and Sigracet GDLs
Otom Group GmbH (Bräunlingen, Germany)	PT 100 RTDs with signal transducer, humidity sensor for atmospheric pressure
Persicaner und Co GmbH (Wien, Austria)	Klingersil sealing Material, PTFE Tubing, Copper sealing rings
QuinTech e.K. (Göppingen, Germany)	Nafion CCMs, Freudenberg GDLs and ice cube fuel cell sealing material
RS Components GmbH (Gmünd, Austria)	various materials, small parts and electronic components
Schraubenking GmbH (Altheim, Austria)	Stainless steel ring screw, stainless steel wire and mounting material
AA-Solutions GmbH (Wiener Neudorf, Austria)	Swagelok adapters
VWR International GmbH (Wien, Austria)	Julabo thermostatic bath heater
Weh Austria (Naarn, Austria)	Low backpressure non return valves for use with H_2
Witt Gastechnik GmbH (Witten, Germany)	Safety pressure relief valve for use with H_2

6.2 Arduino Code

Written and compiled with the ARDUINO integrated development environment version 1.8.19 for ARDUINO DUE. The included libraries are the most recent versions (in April 2022) of the following libraries and their respective dependencies:

- Adafruit_ADS1X15.h
- Arduino.h
- U8x8lib.h

6.2.1 Including Libraries and Variable Initialisation

```
//Debug
//set DEBUG to 1 to activate Serial Output
//set it to 0 to deactivate all Serial debugging Output
#define DEBUG 0
#if DEBUG == 1
#define debug(x) Serial.print(x)
#define debugln(x) Serial.println(x)
#else
#define debug(x)
#define debugln(x)
#endif

#include <Adafruit_ADS1X15.h>

//General:
//how many lines of values in human readable output before the Channel names are repeated
const byte  repeat_channelNames_every = 10;
// So Arduino can count how often it has sent the Information without Channel Names
byte repeat_counter = 10;
// set baud rate for host serial monitor(pc/mac/other)
const unsigned int baud_host  = 38400;
// set at what intervals the readings are sent to the computer (this is not the frequency of taking the readings!)
unsigned int send_readings_every = 1000;
bool human_readable = true;
unsigned long next_serial_time;
// wether or not we're waiting for a reading
boolean request_pending = false;
// holds the time when the next reading should be ready from the circuit
unsigned long next_reading_time;
// INT pointer to hold the current position in the channel_ids/channel_names array
```

```
31 int channel = 0;
32 // A 50 byte character array to hold incoming data from the
      sensors
33 char sensordata[50];
34 // An Integer to check how often The Sensors were read between
      two Serial Communications
35 // This is also used to make sure we dont do Serial
      Communication more often then we question the Sensors
36 unsigned int SpeedTest = 0;
37
38 //Display:
39 byte Display_counter = 0;
40 unsigned long next_display_time;
41 // set at what intervals the Display should be updated (in ms)
42 const unsigned int update_display_every = 4000;
43 #include <Arduino.h>
44 #include <U8x8lib.h>
45 // U8x8 Contructor List
46 // The complete list is available here:
47 // https://github.com/olikraus/u8g2/wiki/u8x8setupcpp
48 U8X8_SH1106_128X64_NONAME_HW_I2C u8x8(/* reset=*/ U8X8_PIN_NONE)
      ;
49
50 //ADS1115 (using the Adafruit Library):
51 //----ADC01
52 //set how many circuits are attached
53 #define TOTAL_CIRCUITS 10
54 #define ads1_addr 72   //ADDR to GND
55 const char ads1_name[] = "I-Sensor";
56 const char ads1_dim[] = "A";
57 bool ads1_bool = true;
58 Adafruit_ADS1115 ads1;
59  /* ADS1115  @ +/- 2.048 gain (16-bit results) to turn from bit
       to mV */
60 const float ads1_multiplier = 0.0625F;
61 //----ADC02
62 #define ads2_addr 73 //ADDR to VDD
63 const char ads2_name[] = "Spannung";
64 const char ads2_dim[] = "mV";
65 bool ads2_bool = true;
66 Adafruit_ADS1115 ads2;
67  /* ADS1115  @ +/- 4.096V gain (16-bit results) to turn from bit
       to mV */
68 const float ads2_multiplier = 0.125F;
69
70 //Arduino Analog Read Pins:
71 #define AnIn_Reference A0
72 #define AnIn_T_Gas A1
73 #define AnIn_rH_Gas A2
```

```
74 #define AnIn_T_Water A3
75 #define AnIn_T_Cathode A4
76 #define AnIn_T_Anode A5
77 #define AnIn_p_Gas A6
78 #define AnIn_T_Cond A7
79
80 //places to store the Analog Read Values
81 //and constants to turn these values to actual values we are
      interested in
82 float reference_float = 0.0;
83 //implementiert die Geradengleichung: y GradC = 100/2.4 GradC/V
      * x V - 60/2.4 GradC
84 //mit 150 Ohm Messwiderstand
85 const float temp_multiplier = 41.667;
86 const float temp_addend = 25.0;
87 //Dip Schalter auf den Messbereich -20 bis + 50 Grad Celsius
      eingestellt
88 const float cond_multiplier = 29.167;
89 //mit 150 Ohm Messwiderstand Implementiert y GradC = 175/6 GradC
      /V * x V - 75/2 GradC
90 const float cond_addend = 37.5;
91 //kPa/V   für die Geradengleichung y kPa = 416.667 kPa/V*x V-250
       kPa
92 const float pres_multiplier = 416.667;
93 //kPa
94 const float pres_addend = 250;
95  //% r.h./V für die Geradengleichung y % r.h.  = 41.667 % r.h. /
       V * x V -25 % r.h.
96 const float rh_multiplier = 41.667;
97 //% r.h.
98 const float rh_addend = 25;
99 //A/V    für die Geradengleichung y A = 90.909 A/V * x V
100 const float current_multiplier = 90.909;
101
102
103 //Arrays to store the Channel Names, Addresses, Pins and Values:
104 //A list of I2C ids or Pin Numbers -> Where to find the Sensor
105 int channel_ids[] = {ads1_addr,
106                      ads2_addr,
107                      AnIn_Reference,
108                      AnIn_rH_Gas,
109                      AnIn_T_Gas,
110                      AnIn_p_Gas,
111                      AnIn_T_Anode,
112                      AnIn_T_Cathode,
113                      AnIn_T_Water,
114                      AnIn_T_Cond};
115 //A list of channel names
116 //(must be the same order as in channel_ids[])
```

```
117 //only used to designate the readings in serial communications
118 const char *channel_names[] = {ads1_name,
119                                ads2_name,
120                                "VRef uncorr",
121                                "rel. hum. in",
122                                "T-Gas in",
123                                "DeltaP Comp.",
124                                "T-Anode  ",
125                                "T-Cathode",
126                                "T-H2O    ",
127                                "T-Condens"};
128 //A list of channel names
129 //(must be the same order as in channel_ids[])
130 //only used to designate the readings in serial communications
131 const char *channel_dim[] = {ads1_dim,
132                              ads2_dim,
133                               "V",
134                               "% r.H.",
135                               "C",
136                               "kPa",
137                               "C",
138                               "C",
139                               "C",
140                               "C"};
141 // an array of floats to hold the readings of each channel
142 float readings[TOTAL_CIRCUITS];
143 
144 //Constants for the Gas cooler PID Temperature controller:
145 //Pin for Analog Output Signal
146 #define AnalogOut_pin DAC1
147 //only perform the PID Calculations every 2000 ms
148 //because remote controlled power supply didnt like geting
149 //new voltage setpoint every few milliseconds
150 const unsigned int calculate_PID_every = 2000;
151 float condenser_temp = 0.0;
152 float PID_error = 0;
153 float previous_error = 0;
154 float elapsedTime, Time_PID, timePrev;
155 float PID_value = 0;
156 unsigned long next_PID_time;
157 float PID_value_unclipped = 0.0;
158 int PID_p = 0;    int PID_i = 0;    int PID_d = 0;
159 //PID constants and T setpoint - Change these Values as needed
160 //(kp/ti = ki)
161 ////////////////////////////////////////////////////
162 unsigned int kp = 1000;
163 unsigned int ti = 400;
164 unsigned int kd = 0;
165 //Default temperature setpoint in degree Celsius
```

```
166 float set_temperature = 10;
167 ////////////////////////////////////////////////////////
```

6.2.2 The “void setup()” Code

```
1  void setup() {
2    // Set the hardware serial port.
3    Serial.begin(baud_host);
4
5    //ADS1115 (using the Adafruit Library)
6    //1x gain   +/- 4.096V   1 bit =  0.125mV
7    ads2.setGain(GAIN_ONE);
8    //2x gain   +/- 2.048V   1 bit =  0.0625mV
9    ads1.setGain(GAIN_TWO);
10
11   if (!ads1.begin(ads1_addr)) {
12     Serial.println("Failed to initialize ADS1");
13     ads1_bool = false;
14   }
15   else{
16     Serial.println("ADS1 initialized");
17   }
18   if (!ads2.begin(ads2_addr)) {
19     Serial.println("Failed to initialize ADS2");
20     ads2_bool = false;
21   }
22   else{
23     Serial.println("ADS2 initialized");
24   }
25
26   //PID Temperature Controller
27   pinMode(AnalogOut_pin,OUTPUT);
28   Time_PID = millis();
29
30   //Serial Communication Time
31   //calculate the next point in time we should do serial
       communications
32   next_serial_time = millis() + send_readings_every;
33
34   //Start the Display Library
35   u8x8.begin();
36   //calculate the next point in time we should update the
       Display
37   next_display_time = millis() + update_display_every;
38 }
```

6.2.3 The “void loop()” and Helper Functions

```
1  void loop() {
2    channel_select();
3    do_serial();
4    PID_controller();
5    do_display();
6    receive_serial();
7  }
8
9  //take sensor readings in a "asynchronous" way
10 void channel_select() {
11   int raw = 0;
12   // a place to store the Value after Mapping it from raw
13   float value = 0.0;
14   // is a request pending?
15   if (request_pending) {
16     // if yes then: is it time for the reading to be taken?
17     if (millis() >= next_reading_time) {
18       //if yes then: where is the reading comming from? -->
             Switch
19       switch (channel_ids[channel]){
20         case ads1_addr:
21           SpeedTest ++;
22           if (ads1_bool == true){
23             //use the Adafruit Library to go and grab the Result
                   from the ADS
24             value = receive_Value_ads1115()*ads1_multiplier
                 /1000;
25             //turns the Voltage from the ADS to the proportional
                   current to the Compressor
26             value = value*current_multiplier;
27             readings[channel] = value;
28             request_pending = false;
29           }
30           //if no ADS is connected under this Address: dont try
                to grab the Results
31           else {
32             request_pending = false;
33             //replace actual value with -111.11 to indicate
                 error
34             readings[channel] = -111.11;
35           }
36           break;
37
38         case ads2_addr:
39           if (ads2_bool == true){
```

```
40            //use the Adafruit Library to go and grab the Result
                  from the ADS and turn it into a voltage
41            value = receive_Value_ads1115()*ads2_multiplier;
42            readings[channel] = value;
43            request_pending = false;
44          }
45          //if no ADS is connected under this Address: dont try
              to grab the Results
46          else {
47            request_pending = false;
48            //replace actual value with -111.11 to indicate
                error
49            readings[channel] = -111.11;
50          }
51          break;
52        case AnIn_Reference:
53          reference_float = analog_stabilizer();
54          //put the float in the readings Array
55          readings[channel] = reference_float;
56          // we are done on this channel, we can read the next
              input
57          request_pending = false;
58          break;
59        //TODO ADD Function to Map it to relative Humidity
60        case AnIn_rH_Gas:
61          value = analog_stabilizer();
62          value = 2.500/reference_float*value;
63          //if The Voltage is under 0.5 Volt --> Overwrite the
              value to -111.11 to indicate error
64          if (value < 0.5){
65            value = -111.11;
66          }
67          else{
68            //change from volts to relative humidity (*k)
69            value = value*rh_multiplier;
70            // (-d)
71            value = value - rh_addend;
72          }
73          //averrage this reading with the last reading to get a
                floating average
74          value = (value + readings[channel])/2.0;
75          //put the float in the readings Array
76          readings[channel] = value;
77          request_pending = false;
78          break;
79        case AnIn_T_Gas:
80          //go and grab the Temperature Value for this channel
              using this helper function
81          readings[channel] = get_Temperature_reading(false);
```

```
82            break;
83          case AnIn_p_Gas:
84            value = analog_stabilizer();
85            value = 2.500/reference_float*value;
86            //if The Voltage is under 0.5 Volt --> Overwrite the
                 value to -111.11 to indicate error
87            if (value < 0.5){
88              value = -111.11;
89            }
90            else{
91              //change from volts to pressure (*k)
92              value = value*pres_multiplier;
93              // (-d)
94              value = value - pres_addend;
95            }
96            //averrage this reading with the last reading to get a
                  floating average
97            value = (value + readings[channel])/2.0;
98            //put the String in the readings Array
99            readings[channel] = value;
100           // we are done on this channel, we can read the next
                 input
101           request_pending = false;
102           break;
103         case AnIn_T_Anode:
104           //go and grab the Temperature Value for this channel
                 using this helper function
105           readings[channel] = get_Temperature_reading(false);
106           break;
107         case AnIn_T_Cathode:
108           //go and grab the Temperature Value for this channel
                 using this helper function
109           readings[channel] = get_Temperature_reading(false);
110           break;
111         case AnIn_T_Water:
112           //go and grab the Temperature Value for this channel
                 using this helper function
113           readings[channel] = get_Temperature_reading(false);
114           break;
115         case AnIn_T_Cond:
116           //go and grab the Temperature Value for this channel
                 using this function
117           //use the "true" to also save the Temperature as the
                 Temperature for the PID controller
118           readings[channel] = get_Temperature_reading(true);
119           break;
120       }
121     }
122     else {
```

```
123       ;
124     }
125   }
126   // no request is pending on the current channel so we...
127   else {
128     // switch to the next channel (increase current channel by
          1, and roll over if we're at the last channel using the %
           modulo operator)
129     channel = (channel + 1) % TOTAL_CIRCUITS;
130     //what is the next circuit that i want to request a reading
          from?
131     switch (channel_ids[channel]){
132       case ads1_addr:
133         //is set to Continuous Mode --> Request is always
              Pending
134         request_pending = true;
135         break;
136       case ads2_addr:
137         //is set to Continuous Mode --> Request is always
              Pending
138         request_pending = true;
139         break;
140       case AnIn_Reference:
141           request_pending = true;
142           break;
143       case AnIn_rH_Gas:
144           request_pending = true;
145           break;
146       case AnIn_T_Gas:
147           request_pending = true;
148           break;
149       case AnIn_p_Gas:
150           request_pending = true;
151           break;
152       case AnIn_T_Anode:
153           request_pending = true;
154           break;
155       case AnIn_T_Cathode:
156           request_pending = true;
157           break;
158       case AnIn_T_Water:
159           request_pending = true;
160           break;
161       case AnIn_T_Cond:
162           request_pending = true;
163           break;
164       }
165   }
166 }
```

```
167
168 //Receive a reading from the current channel if the current
      channel is one of the ADCs Channels
169 int16_t receive_Value_ads1115(){
170   int16_t adcInt;
171   if(channel_ids[channel]==ads1_addr) {
172       adcInt = ads1.readADC_Differential_2_3();
173   }
174   else if(channel_ids[channel]==ads2_addr) {
175       adcInt = ads2.readADC_Differential_0_1();
176   }
177   return adcInt;
178 }
179
180 float get_Temperature_reading(bool use_for_PID){
181   //To Handle the Voltage from this Analog Channel in this
        function
182   float voltage = 0.0;
183   //To Handle the Value for the Temperature calculated from the
        Voltage inside this Function
184   float Temp = 0.0;
185   voltage = analog_stabilizer();
186   voltage = 2.500/reference_float*voltage;
187   if (use_for_PID==false){
188    //Turn Voltage into Temperature with normal constants
189     Temp = voltage * temp_multiplier;
190     Temp = Temp - temp_addend;
191     //average Temperature with the Reading that it had the last
          time we checked to get a floating average
192     Temp = (Temp + readings[channel])/2.0;
193   }
194   //if this flag was passed to the function --> Use this Temp
        for the PID and use different constants
195   else if (use_for_PID==true){
196     //Turn Voltage into Temperature with other constants
197     Temp = voltage * cond_multiplier;
198     Temp = Temp - cond_addend;
199     //average Temperature with the Reading that it had the last
          time we checked to get a floating average
200     Temp = (Temp + readings[channel])/2.0;
201     condenser_temp=Temp;
202     use_for_PID=false;
203   }
204   //if The Voltage is under 0.5 Volt --> Overwrite the value
        with -111.11 to indicate something is wrong
205   if (voltage < 0.5){
206     Temp = -111.11;
207   }
208   request_pending = false;
```

```
209   return Temp;
210 }
211
212 // do serial communication in a "asynchronous" way
213 void do_serial() {
214   // is it time for the next serial communication?
215   if (millis() >= next_serial_time && SpeedTest > 1) {
216     if (human_readable == true){
217       // we want to repeat the channel Names every time the
            counter reaches max
218       if (repeat_counter < repeat_channelNames_every) {
219         for (int i = 0; i < TOTAL_CIRCUITS; i++) {
220           Serial.print(readings[i]);
221           Serial.print("\t\t");
222         }
223         Serial.println(" ");
224         repeat_counter++;
225       }
226       //When the Counter reaches the maximum: reset it to 0 and
            print the channel names and Dimensions once
227       else {
228         for (int i = 0; i < TOTAL_CIRCUITS; i++) {
229           Serial.print(channel_names[i]);
230           Serial.print("\t");
231         }
232         Serial.println(" ");
233         for (int i = 0; i < TOTAL_CIRCUITS; i++) {
234           Serial.print(" ");
235           Serial.print(channel_dim[i]);
236           Serial.print("\t\t");
237         }
238         Serial.println(" ");
239         repeat_counter = 0;
240       }
241 //      // loop through all the sensors
242 //      for (int i = 0; i < TOTAL_CIRCUITS; i++) {
243 //        // print channel name
244 //        Serial.print(channel_names[i]);
245 //        Serial.print(":\t");
246 //        // print the actual reading
247 //        Serial.print(readings[i]);
248 //        Serial.print(" ");
249 //        //print the Current Channels Dimension
250 //        Serial.println(channel_dim[i]);
251 //      }
252     debug("PID unclipped");
253     debugln(PID_value_unclipped);
254     debug("PID_i Wert");
255     debugln(PID_i);
```

```
256     debug("So oft wurde der Channel 1 zwischen zwei Serial
           Communications gemessen: ");
257     debugln(SpeedTest);
258     }
259     //Readings should be sent in a machine readable form
260     else{
261       for (int i = 0; i < TOTAL_CIRCUITS; i++) {
262         Serial.print(";");
263         Serial.print(readings[i]);
264       }
265       Serial.println(";");
266     }
267
268     SpeedTest = 0;
269     next_serial_time = millis() + send_readings_every;
270   }
271 }
272 //Displaybreite 16 Zeichen Displayhöhe 8 Zeilen
273 void do_display(){
274   if (millis() >= next_display_time) {                  // is it
         time for the next serial communication?
275     u8x8.clear();                                       //clear
         the screen
276     u8x8.setFont(u8x8_font_amstrad_cpc_extended_f);     //set the
         font
277     u8x8.setCursor(0,0);                                //put the
         cursor in the top left corner
278     byte i = 9;                                         //set the
         indentation to put the values
279     if (Display_counter == 0){
280       u8x8.print("1/2 PID Control");
281       u8x8.setCursor(0,2);                              //put the
           cursor in the second line
282       u8x8.print("T-Cond:");
283       u8x8.setCursor(i,2);                              //put the
           cursor in the second line to the right to write the
           value
284       u8x8.print(condenser_temp);
285       u8x8.setCursor(0,3);                              //put the
           cursor in the third line
286       u8x8.print("T-Set:");
287       u8x8.setCursor(i,3);                              //put the
           cursor in the third line to the right to write the
           value
288       u8x8.print(set_temperature);
289       u8x8.setCursor(0,4);                              //put the
           cursor in the fifth line
290       u8x8.print("PID_p:");
```

```
291       u8x8.setCursor(i,4);                              //put the
              cursor in the fifth line to the right to write the
              value
292       u8x8.print(PID_p);
293       u8x8.setCursor(0,5);                              //put the
              cursor in the sixth line
294       u8x8.print("PID_i:");
295       u8x8.setCursor(i,5);                              //put the
              cursor in the sixth line to the right to write the
              value
296       u8x8.print(PID_i);
297       u8x8.setCursor(0,6);                              //put the
              cursor in the seventh line
298       u8x8.print("PID_d:");
299       u8x8.setCursor(i,6);                              //put the
              cursor in the seventh line to the right to write the
              value
300       u8x8.print(PID_d);
301       u8x8.setCursor(0,7);                              //put the
              cursor in the eigth line
302       u8x8.print("PID:");
303       u8x8.setCursor(i,7);                              //put the
              cursor in the eigth line to the right to write the
              value
304       u8x8.print(PID_value);
305       Display_counter++;
306       next_display_time = millis() + update_display_every; //
              Calculate the next time we should update the Display
307     }
308     else if (Display_counter == 1){
309       u8x8.print("2/2 Readings");
310       u8x8.setCursor(0,2);                              //put the
              cursor in the second line
311       u8x8.print("Delta-P:");
312       u8x8.setCursor(i,2);                              //put the
              cursor in the second line to the right to write the
              value
313       u8x8.print(readings[5]);                          //you have
               to manually set where the pressure value is stored in
              the Array
314       u8x8.setCursor(0,3);                              //put the
              cursor in the third line
315       u8x8.print("Voltage:");
316       u8x8.setCursor(i,3);                              //put the
              cursor in the third line to the right to write the
              value
317       u8x8.print(readings[1]);                          //The
              Voltage Value is stored here
```

```
318       u8x8.setCursor(0,4);                                  //put the
              cursor in the fourth line
319       u8x8.print("Current:");
320       u8x8.setCursor(i,4);
321       u8x8.print(readings[0]);
322       Display_counter++;
323       //Calculate the next time we should update the Display
324       next_display_time = millis() + update_display_every;
325
326     }
327     else { //if the Displaycounter is not 0 or 1 then we reset
            it to 0
328       Display_counter = 0;
329     }
330
331   }
332 }
333 //If anyone send anything via the Serial Command: we can go and
     grab it here
334 void receive_serial(){
335   if (Serial.available() > 0) {
336     //for first incomming byte
337     byte incomingByte = 0;
338     //if you dont receive anything further for 100 ms: just
          continue with normal business
339     Serial.setTimeout(100);
340     // read the first incoming byte to determine what to do next
          :
341     incomingByte = Serial.read();
342
343     //T = 0x54 was the first byte we received? Someone wants to
          Transmit a Temperature
344     if (incomingByte == 0x54){
345       float Temp = -10.0;
346       Temp = Serial.parseFloat(SKIP_WHITESPACE);
347       if (Temp+5 > 0 && Temp < 25){
348         set_temperature = Temp;
349         Serial.print("New Temperature Setpoint is: ");
350         Serial.print(set_temperature);
351         Serial.println(" Celsius");
352       }
353       else{
354         Serial.println("Error! Temperature out of Bounds (-5 to
              +25 Celsius)");
355       }
356     }
357
358     //h = 0x68 is the first byte we received? Someone wants to
          Display the Help message
```

```
359     else if (incomingByte == 0x68){
360     Serial.println("Help Message: ");
361     Serial.println("Send 'h' to view this Help Message");
362     Serial.println("Send 'm' to switch from human readable to
           machine readable output Format and back");
363     Serial.println("Send 'T 10.0' to change the Condenser set
           Temperature (e.g. to 10.0 Degrees Celsius)");
364     Serial.println("Send 'f 1000' to change the Frequency of
           Serial communication (1000 = send once every 1000 ms)");
365    }
366
367     //m = 0x6D is the first byte we received? Someone wants to
           togle machine and human readable output Format
368     else if (incomingByte == 0x6D){
369       if (human_readable == true){
370         human_readable = false;
371         Serial.println("Switching to machine readable output
              Format.");
372         Serial.println("Output from here on will be: ");
373         for (int i = 0; i < TOTAL_CIRCUITS; i++) {
374           Serial.print(";[");
375           Serial.print(channel_names[i]);
376           Serial.print("]=");
377           Serial.print(channel_dim[i]);
378         }
379         Serial.println(";");
380       }
381       else{
382         human_readable = true;
383         Serial.println("Switching to human readable output
              Format.");
384       }
385     }
386
387     //f = 0x66 is the first byte we received? Someone wants to
           change the Frequency of Serial Communication
388     else if (incomingByte == 0x66){
389       int Temp = 0;
390       Temp = Serial.parseInt(SKIP_WHITESPACE);
391       if (Temp > 0){
392         send_readings_every = Temp;
393         Serial.print("Trying to report values once every ");
394         Serial.print(Temp);
395         Serial.println(" ms from now on");
396       }
397       else {
398         Serial.println("Error! Time has to be an Integer bigger
              then 0");
399       }
```

```
400     }
401
402     else {
403     Serial.println(incomingByte);
404     Serial.println("unknown command, press h to Display help");
405    }
406   //Whatever the Communication just was: Leave the user some
        time to read before continuing with normal reporting
407   next_serial_time = millis() + 4000;
408   }
409 }
410
411 void PID_controller(){
412   if (millis() >= next_PID_time) {
413     //First we calculate the error between the setpoint and the
          real value
414     PID_error = condenser_temp - set_temperature;
415     //Calculate the P value
416     PID_p = kp * PID_error;
417     //For derivative and Integral we need real time to calculate
           speed change rate and Integral
418     timePrev = Time_PID;                                  // the
          previous time is stored before the actual time read
419     Time_PID = millis();                                  // actual
          time read
420     elapsedTime = (Time_PID - timePrev) / 1000;
421     //Now we can calculate the D calue
422     PID_d = kd*((PID_error - previous_error)/elapsedTime);
423     //Calculate the I value (gets bigger overtime)
424     if (PID_i>4000){            //it should get bigger over time
          ... but we dont want it to go completely overboard
425       PID_i=3999;
426     }
427     else if (PID_i<-4000){      //it should get bigger over time
          .... but we dont want it to go completely overboard
428       PID_i=-3999;
429     }
430     else {
431       PID_i = PID_i + (kp/ti * PID_error * elapsedTime);
432     }
433     //Final total PID value is the sum of P + I + D
434     PID_value = PID_p + PID_i + PID_d;
435     PID_value_unclipped = PID_value;
436     //We define Analog Signals range between 0 and 4095 (0-3.3
          Volt... actually only 0.55 V to 2.75V)
437     if(PID_value < 0)
438     {    PID_value = 0;    }
439     if(PID_value > 4095)
440     {    PID_value = 4095;  }
```

```
441     //Now we can write the Analog signal to the Analog Output
           pin (input for the Lab Power Suply)
442     analogWriteResolution(12);
443     analogWrite(AnalogOut_pin,int(PID_value));
444     next_PID_time = millis() + calculate_PID_every; // calculate
            the next time to request a reading
445     previous_error = PID_error;                     // Store the
            previous error for next loop.
446   }
447 }
448
449 //take averages over many Analog Reads to stabilize the output
450 float analog_stabilizer(){
451   int raw = 0;
452   unsigned long sumierer = 0;
453   float voltage = 0.0;
454   for (int i = 0; i < 300; i++) {
455     //Change the resolution of the Arduinos Internal ADC from
          Standard 10 bit to 12 bit. (0-4095)
456     analogReadResolution(12);
457     raw = analogRead(channel_ids[channel]);
458     sumierer = sumierer+raw;
459   }
460    //divide by the Number of Cycles you looped in the for loop
         and map it to 3.3 Volt
461   voltage = fmap(sumierer/300, 0, 4095, 0.0, 3.3);
462   return voltage;
463 }
464
465 //A Function to Map the Analog input to a Voltage (float)
466 float fmap(float x, float in_min, float in_max, float out_min,
       float out_max){
467   return (x - in_min) * (out_max - out_min) / (in_max - in_min)
        + out_min;
468   }
```